INFRARED SPECTROSCOPY OF CLUSTER IONS: HIGH ENERGY CONFORMER TRAPPING AND MULTIPLE PHOTON ABSORPTION

BY

JORDAN PATRICK BECK

DISSERTATION

Submitted in partial fulfillment of the requirements
for the degree of Doctor of Philosophy in Chemistry
in the Graduate College of the
University of Illinois at Urbana-Champaign, 2011

Urbana, Illinois

Doctoral Committee:

Professor James M. Lisy, Chair
Professor Martin Gruebele
Assistant Professor Benjamin McCall
Assistant Professor Benjamin Lev

Abstract

Infrared predissociation (IRPD) spectra of several cluster ions are presented, resulting in the emergence of two major themes. Trapped, high energy conformers are observed in argon tagged clusters. In non-argon tagged hydrated alkali metal ion clusters, multiple photon absorption processes can occur.

The cluster ions discussed in this dissertation are generated by impacting neutral clusters with ions. If there is an energetic barrier between the neutral cluster configuration and the global minimum cluster ion configuration that is larger than the binding energy of the most labile ligand, then high energy conformers can be trapped. Thus, the trapped conformers retain some of the bonds of their neutral precursors. For example, neutral methanol dimer contains a hydrogen bond and a trapped, high energy $Cl^-(CH_3OH)_2Ar$ conformer was observed which also contains a methanol•••methanol hydrogen bond. Similar results are reported for $M^+(C_6H_6)_{2\text{-}4}(H_2O)_2Ar$ and M^+(benzyl alcohol)$_1(H_2O)_{1\text{-}2}Ar$ where IRPD spectra reveal hydrogen bonds resulting from the configurations of the neutral precursors.

For most of the clusters studied, spectral features from high energy conformers and global minimum energy conformers were observed in the same spectra. However, a special case is reported in chapter 5 in which spectral features from high energy conformers and global minimum energy conformers of $Li^+(C_6H_6)_{2\text{-}4}(H_2O)_2Ar$ were observed in different spectra corresponding to the fragmentation channel monitored. This conformer-specific fragmentation greatly simplified the interpretation of the spectra and provided useful information on the cluster energetics.

Conformer specific fragmentation was also observed for $M^+(H_2O)_{5-7}$, but for a different reason. In the hydrogen bonded O-H stretching region, IRPD spectra obtained by monitoring the loss of two waters only contained features from linear hydrogen bonds. This mode dependent fragmentation is believed to be the result of multiple photon absorption. This conclusion is supported by laser-fluence dependence studies and by evaporative ensemble calculations.

Acknowledgements

First and foremost, I would like to thank my beautiful, loving, and dedicated wife, Beth. She has been a constant source of support, encouragement, and understanding for me through my years as a graduate student.

Thank you also to my family scattered about northern Illinois and Iowa. The times that we gather together always bolster my spirit and bring me great joy. I would like to give a special acknowledgement to my parents, Loren and Cynthia, who have given me unconditional love and support.

I am grateful for all the wonderful friends and fellow believers from Good Shepherd Lutheran Church. I have appreciated the opportunity to grow in faith with you all and thank you for your encouragement.

Professor Lisy has been a great mentor in both the scientific and educational realms. Scientifically, his deep understanding of cluster ions and his chemical intuition has proven to be an invaluable resource. I also appreciate all the opportunities Professor Lisy gave me to work on educational projects. The experience I gained working with him in teaching physical chemistry will serve me well in my future career.

I would like to thank my fellow lab mates: Jason Rodriguez, Oscar Rodriguez Jr., Amy Nicely, and Dotti Miller. Jason has been a great friend, confidant, and mentor to me. I would like to thank him for his encouragement and advice. Thank you, Oscar, for reading my dissertation several times and for providing me with detailed suggestions. Also, thanks for always being available to “talk science”.

The work of this dissertation was greatly supported by the SCS staff. I would like to specifically acknowledge Jim Wentz and Mike Hallock. Jim was extremely knowledgeable, helpful, and prompt. Mike has been great at helping me with any calculation related issues. They are both great at what they do.

Finally, I thank Professor Paul Kelter, Dr. Donald DeCoste, and An Phong-Le. It has been a privilege learning about chemical education with you.

To Beth

Table of Contents

Chapter 1: Introduction

1.1 Motivation

Infrared (IR) spectroscopy of gas phase cluster ions is a very powerful tool used to probe non-covalent interactions[1-3].

Infrared spectroscopy is used to study vibrational modes of molecules and complexes. Several commonly studied stretching modes, including the O-H and N-H stretching modes, are very sensitive to their local environment[4,5]. For example, hydrogen bond formation can cause O-H stretching frequencies to shift hundreds of wavenumbers. Additionally, these frequency shifts are also accompanied by an increase in IR intensity[4,5].

Gas phase cluster ions are systems containing an ion and a small (for our purposes, less than ~50), but well-defined number of atoms and/or molecules. Since the number of constituents in gas phase cluster ions is so small, they can be used to study very specific interactions between molecules without the perturbations caused by bulk phase solvents[6,7]. Additionally, with the presence of only one ion, counterion effects are completely eliminated.

Compared to studies on neutral gas phase clusters[8-10], the presence of an ion in a gas phase cluster ion has several benefits. First, the presence of the charge allows for facile mass selection using standard mass spectrometric techniques prior to probing the cluster. Second, ion•••neutral interactions are important in many chemical processes[11-13]. Not only can cluster ions be used to probe such ion•••neutral interactions, but the influence of the ion on neutral•••neutral interactions can be determined as well. This

combination allows for a more complete description of the relative importance of various competing and cooperative non-covalent interactions[14].

One final major advantage to studying gas phase cluster ions is that the systems are small enough to permit high level electronic structure calculations, creating a synergy between experiment and theory. The calculations provide support for the assignments of experimental spectral features. The experiments, in turn, provide benchmarks for theorists.

1.2 IRPD and Argon Tagging

Infrared predissociation spectroscopy (IRPD) is the primary technique used in the Lisy lab to investigate cluster ions. In this action spectral technique, which is described in detail in chapter 2, IR spectra are obtained by monitoring cluster fragmentation following photon absorption. One design consideration for this method is the pressure in the experimental apparatus. If the pressure is too high, collision induced dissociation can become a major source of noise in the IRPD spectra. A significant improvement was made to the experimental apparatus in the Lisy lab in 2005 when a differentially pumped chamber was installed between the ion source and detector[15]. This lowered the experimental pressure (detector chamber pressure) by around an order of magnitude (to ~ $1x10^{-7}$ Torr), effectively eliminating collision induced dissociation.

This design improvement opened the door for the investigation of systems that were previously difficult or impossible to study in the Lisy lab. One class of clusters that became much more viable for examination was argon tagged cluster ions. Argon tagging is a well established experimental technique which has two major implications on the IRPD spectra. First, argon tagging reduces the internal energies and effective

temperatures of the clusters leading to better resolved spectral features. Second, argon tagging allows high energy structural conformers to be trapped in the cluster ion beam and subsequently probed, as reported in chapters 3,5, and 6. Thus, by studying argon tagged clusters, a more detailed description of the potential energy surface can be obtained.

1.3 Chapter Overview

Chapter 2 is a highly detailed description of the experimental apparatus used for the acquisition of the IRPD spectra reported in this dissertation.

In chapters 3 – 4, the influence of the chloride anion on two systems is discussed. The major focus of these chapters is the ionic hydrogen bond. For both $Cl^-(CH_3OH)_{1\text{-}3}Ar$ and Cl^-(*N*-methylacetamide)$_1(H_2O)_{0\text{-}2}Ar_2$, the ionic hydrogen bond is strengthened by cooperative effects as the number of solvent ligands is increased.

Interactions between aromatic ligands, alkali metal ions, and water are investigated in chapters 5 – 6. Unique and compact global minimum energy structures are inferred from experimental spectra and calculations for $Li^+(C_6H_6)_{2\text{-}4}(H_2O)_2Ar_{0\text{-}1}$. High energy isomers are also observed for $Li^+(C_6H_6)_{2\text{-}4}(H_2O)_2Ar_1$ and are selectively probed in the loss of ($Ar + C_6H_6$) fragmentation channel. The influence of a ligand which contains both aromatic and polar sites is studied by using benzyl alcohol. In both chapters, the effect of ion size is studied by using both Li^+ and Na^+.

The only chapter describing experimental results of non-argonated clusters is chapter 7. Spectra of $M^+(H_2O)_{5\text{-}7}$, M = alkali metal, in two fragmentation channels are reported. Multiple photon absorption is proposed to explain the spectral patterns

observed in the fragmentation channels in light of fluence dependence data, and energy calculations.

Chapter 8 describes two new computer programs that can be used to calculate internal energy distributions of cluster ions produced via evaporation. The results of these calculations are applied to modeling mass spectra are used as evidence of multiple photon absorption.

1.4 References

(1) Duncan, M. A. *International Reviews in Physical Chemistry* **2003**, *22*, 407.
(2) Lisy, J. M. *Journal of Chemical Physics* **2006**, *125*, 132302.
(3) Robertson, W. H.; Johnson, M. A. *Annual Review of Physical Chemistry* **2003**, *54*, 173.
(4) *Hydrogen Bonding - New Insights*; Grabowski, S. J., Ed.; Springer: Dordrecht, The Netherlands, 2006; Vol. 3.
(5) *Recent Theoretical and Experimental Advances in Hydrogen Bonded Clusters*; Xantheas, S. S., Ed.; Kluwer Academic Publishers: Dordrecht, The Netherlands, 2000.
(6) Lisy, J. M. Vibrational Spectroscopy of Cluster Ions. In *Cluster Ions*; Ng, C. Y., Baer, T., Powis, I., Eds.; John Wiley and Sons: New Yord City, 1993; pp 217.
(7) Lisy, J. M. *International Reviews in Physical Chemistry* **1997**, *16*, 267.
(8) de Vries, M. S.; Hobza, P. *Annual Review of Physical Chemistry* **2007**, *58*, 585.
(9) Robertson, E. G.; Simons, J. P. *Physical Chemistry Chemical Physics* **2001**, *3*, 1.
(10) Zwier, T. S. *The Journal of Physical Chemistry A* **2001**, *105*, 8827.
(11) Davis, J. T. *Nature Chemistry* **2010**, *2*, 516.
(12) Jungwirth, P.; Tobias, D. J. *Journal of Physical Chemistry B* **2002**, *106*, 6361.
(13) Knipping, E. M.; Lakin, M. J.; Foster, K. L.; Jungwirth, P.; Tobias, D. J.; Gerber, R. B.; Dabdub, D.; Finlayson-Pitts, B. J. *Science* **2000**, *288*, 301.
(14) Muller-Dethlefs, K.; Hobza, P. *Chemical Reviews* **1999**, *100*, 143.
(15) Miller, D. J. Elucidating the hydration of biomolecules: An experimental and computational approach, University of Illinois at Urbana-Champaign, 2007.

Chapter 2: Experimental Details

2.1 Introduction

In the Lisy lab, a triple quadrupole apparatus combined with an IR laser is used to obtain IR spectra of cluster ions. As shown in Figure 2.1 and Table 2.1, this device contains a variety of components which will be discussed in detail in this chapter. Briefly, neutral clusters are formed by the supersonic expansion of a mixture of gasses through a 180 μm diameter conical nozzle to generate neutral clusters. Approximately 100 nozzle diameters downstream, ions, generated from a home-built ion gun, perpendicularly impact the fully expanded neutral beam. The ions are thermionically emitted from a filament coated with a paste prepared by rinsing a commercially available molecular sieve with a saturated solution of an alkali-halide salt. The nascent cluster ions have a significant amount of internal energy (~1000 kJ/mol) from the ion impact and subsequent solvation. The excess energy is then dissipated via evaporative cooling until the clusters reach a quasi-stable state (i.e. until the unimolecular dissociation lifetime exceeds the ~200 μs flight time through the apparatus). The cluster ions are guided by electrostatic lenses from the source chamber, through an octupole ion guide in a second differentially-pumped chamber, and into the detection chamber. The latter chamber houses the triple quadrupole mass spectrometer and the detector (a channeltron electron multiplier equipped with a conversion dynode). The parent ion of interest is mass selected in the first quadrupole. The second quadrupole, a radio frequency only device, 60 cm in length, serves as an ion guide, where the ions interact with a single ~ 10 ns pulse from a gently-focused, tunable IR laser (LaserVision OPO/OPA pumped by a 10 Hz Surelite II Nd:YAG laser). The absorption of a mid-IR photon induces dissociation

and the third quadruple, a mass-filter, is tuned to the mass of a fragment ion. Fluence-corrected photodissociation cross-sections are reported as a function of IR frequency.

2.2 Triple Quadrupole

Gas Handling

A schematic representation of the gas handling and mixture setup for the production of clusters containing water and argon is shown in Figure 2.2. A line of neat argon exits the gas tank at a pressure of 8±2 psig. With a typical atmospheric pressure of 760 Torr, this corresponds to an absolute pressure of 1170±100 Torr. This line may be split into two or more lines. One of the argon lines is connected directly to a mass flow controller. The others pass through bubblers containing water before reaching a separate flow controller. Assuming the argon passing through the bubblers becomes saturated with the solvent, the composition of the flow streams can be approximated. Water, for example, has a vapor pressure of 20 Torr at typical lab temperature of 22^{o}C. Therefore, the gas mixture exiting a water bubbler has an approximate water mole fraction of:

$$\chi_{H_2O} \approx \frac{20}{1170+20} = 0.017 \pm 0.002$$

In general, the flows exiting the bubblers are further diluted by recombining them with the pure argon stream after the flow controllers.

The flow controllers (MKS 1159) are devices that regulate gas flow by measuring the amount of heat required to maintain a constant temperature of the gas flowing through. A small portion of the gas stream is sent through a sensor tube which contains a resistance heater. The voltage required to maintain a constant temperature is a linear function of the flow. The output is given in equivalent flow rate of nitrogen (sccm N_2).

In order to determine the actual flow rate of the gas stream, the output must be multiplied by a gas correction factor (GCF):

$$GCF = \frac{0.316*(S)}{d*C_P}$$

where S=molecular structure correction factor (1.03 for monatomic gases, 1 for diatomics, 0.941 for triatomics, and 0.88 for polyatomics), d=standard density in g/L, C_P=Specific heat in cal/g^{o}C. For argon, the gas correction factor is 1.39. Although the argon/water flow has a slightly smaller GCF due to the presence of the water, the error introduced by using 1.39 for this stream is smaller than the accuracy of the instrument itself and is ignored. The accuracy of the flow controllers is reported to be 1% of the full scale value, which for the pure argon stream is 1000 sccm N_2, leading to an uncertainty of ±10 sccm.

Depending on the types of clusters desired, the ratio of pure argon to argon/solvent can be varied. Typical values for the production of hydrated alkali metal ion clusters are ~70-150 sccm Ar and ~80-170 sccm Ar/H_2O (with 100 sccm from each stream, the overall water mole fraction is ~0.009). To make argonated clusters, the flow of the argon/water is significantly reduced to ~1-30 sccm (with conditions of 150 sccm Ar and 15 sccm argon/water, the final water mole fraction is ~0.002). The total flow rate to the nozzle is generally kept at around 140-240 sccm.

Before the gas mixture reaches the nozzle, a pressure measurement is taken using an Edwards EPS diaphragm pressure gauge. This gauge contains a diaphragm where one side of the diaphragm is connected to the gas line and the other side is at a reference pressure. The pressure differential causes a deflection of the diaphragm. The amount of deflection is measured with a strain gauge mounted on the diaphragm and is proportional

to the pressure and independent of the gas composition. Typical backing pressures used are 300-550 Torr.

When we study substances that, at room temperature, are in the solid state (*N*-methylacetamide, e.g.) or have a low vapor pressure (benzyl alcohol, e.g), the bubbler technique does not work. In these cases, a sample cell is placed after the backing pressure gauge and prior to the nozzle (see Figure 2.1). The cell is heated which produces an increased solvent vapor pressure and, therefore, more efficient entrainment.

Supersonic Expansion

To enter the source chamber, the gas passes through a 180 μm conical nozzle. The gas will reach supersonic speeds if the ratio of the backing pressure to the chamber pressure (P_b/P_c) exceeds a critical value of ~2.1[1]. With a typical backing pressure of P_b=400 Torr and source chamber pressure of $P_c=4\text{x}10^{-4}$ Torr, the ratio (P_b/P_c)=$1\text{x}10^{6}$, well above the critical value. Additionally, supersonic beams have a pressure at the exit of the nozzle equal to approximately half of the backing pressure. Since the beam pressure is higher than the chamber pressure, the beam expands. The center of the expansion is isentropic and is referred to as the zone of silence. The zone of silence extends in the axial direction (direction of flow) until the Mach disc is reached at a distance of $x_m = 0.67d\left(\frac{P_b}{P_c}\right)^{1/2}$, where x_m is the mach disc location and d is the diameter of the nozzle. For the conditions specified above, x_m=12 cm, which is approximately the distance from the nozzle to the skimmer in our apparatus. As the gas expands, the temperature decreases, but the gas also accelerates. This corresponds to a narrowing of the velocity distribution around a velocity higher than the average stagnation velocity as shown in Figure 2.3. The two important factors in determining the velocity and

temperature are the molar mass of the gas and the heat capacity ratio, $\gamma = C_P / C_V$, as shown in the following equations:

$$\frac{P}{P_b} = \left(\frac{T}{T_b} \right)^{\frac{\gamma}{\gamma - 1}}$$

$$Velocity = V = \sqrt{\frac{2R}{W} \left(\frac{\gamma}{\gamma - 1} \right) \left(T_b - T \right)}$$

where the subscript b refers to the backing conditions and W is the molecular weight. Thus it can be seen that heavier molecules will produce slower beams. Also, using polyatomic molecules will result in warmer beams due to smaller values for γ.

Due to the large temperature drop during the expansion, the gas atoms and molecules can coalesce, leading to the production of neutral clusters. The size of clusters produced is determined by three factors[2]. Larger clusters are produced with higher backing pressures and larger nozzle apertures, whereas higher initial gas temperatures tend to produce smaller clusters. Due to the release of the binding energy, cluster formation limits the terminal temperature of the beam. Pure argon cluster beams have temperatures on the order of 10 K.

The formation of mixed clusters in our experiments can be explained more quantitatively with the aid of the energy diagram shown in Figure 2.4. The seed for any larger cluster is the production of an argon dimer, which would require the release of ~1 kJ/mol of energy by collisions with other argon atoms. A possible path for the formation of a mixed cluster is then $Ar_2 + H_2O \rightarrow Ar_2(H_2O)^* \rightarrow Ar(H_2O) + Ar$. As can be seen from Figure 2.4, this process would require the release of an additional ~0.7 kJ/mol of energy. This simple example emphasizes the role of the carrier gas in the production of

clusters. The carrier gas serves to remove the cohesive energy via collisions and evaporation.

The expanded beam of neutral clusters is impacted perpendicularly with a stream of metal ions approximately 3 cm downstream of the nozzle aperture. The metal ions are produced from an ion gun setup which consists of a filament and a series of electrostatic lenses to guide the ions toward the neutral beam. The filament is coated with an enriched paste created by combining an aqueous solution saturated with M^+ with a molecular sieve, $K_nNa_{12-n}\left[\left(AlO_2\right)_{12}\left(SiO_2\right)_{12}\right]\cdot xH_2O$. The ion M^+ will undergo ion exchange reactions with the potassium and sodium ions in the sieve, enriching the paste in M^+. This paste is applied to a coil made from 0.008 inch diameter tungsten filament wire. When a current is passed through the coated filament, the filament heats up resulting in thermionic emission of the metal ion M^+. The ratio of ions to atoms emitted is related to the ionization potential Φ, work function ϕ, and temperature T as shown below[3].

$$\frac{\text{Ions Emitted}}{\text{Atoms Emitted}} \propto \exp\left[\frac{-(\Phi-\phi)}{kT}\right]$$

The ionization potential and work function for the alkali metals are shown in Table 2.2. Traditionally, the cesium ion has been the easiest to obtain in the lab as indicated by its relatively low value of Φ-ϕ. To enhance the production of ions and supply them with an initial potential energy, the filament is biased with respect to chamber ground. Typical values used for the ion gun are a current of 2.6-3.2 Amps and a bias of 25-30 V.

Upon impact, the clusters can solvate the metal ion. Due to the solvation energy (which is approximately 40 kJ/mol per water molecule) and the energy of the metal ion, the nascent cluster ions have a large amount of energy (order of thousand kJ/mol) and are

therefore unstable. The clusters dissipate this excess energy through evaporative cooling. In any given cluster, each evaporative step removes energy and mass. Each water evaporation increases the lifetime of the cluster by roughly an order of magnitude. Evaporation continues until the cluster has a lifetime sufficient to reach the detector. Average internal energy and temperature distributions of the cluster ions that reach the detector can be modeled using the evaporative ensemble formalism.

Vacuum System

Clearly, an efficient vacuum system is required to maintain the pressure differential necessary to create a supersonic expansion. Also, differential pumping is necessary to maintain a low pressure (~10^{-7} Torr) in the detector chamber in order to eliminate collisions. For these purposes, a three-stage system containing diffusion, turbomolecular, roots, and rotary vane pumps is utilized. The source chamber is pumped by a Varian 10 in., 3650 L/s diffusion pump. Diffusion pumps consist of a pump vessel with water cooled walls and a series of nozzles. Inside the vessel is a pump fluid (NeoVac SY) which is heated and vaporized by a boiler plate and supersonically expanded through the nozzles in a downward direction toward the walls. As the gas to be pumped diffuses into the fluid jet, it is imparted with a net downward momentum, thereby compressing the gas at the pump outlet. When the pumping fluid reaches the cooled wall, it condenses and flows back to the boiler. It is important that the pressure in a diffusion pump does not become too high. If it does, the pump will no longer operate properly because the pump fluid jet is significantly altered by the gas in the pump. As shown in Figure 2.5, the maximum chamber and foreline pressures are 1.7×10^{-3} Torr and 0.6 Torr, respectively. Because the source pump is responsible for pumping the majority

of the gas load input into the system, it is backed by a 60 L/s roots pump in series with a 10 L/s, two-stage rotary vane pump. Roots pumps consist of two peanut-shaped impellers which spin in a synchronous manner inside a casing in order to compress the gas. Since oil is not used to seal these pumps they are able to rotate at around 3000 rpm. Rotary vane pumps, however, are oil sealed and operate by using a vane and rotor to continually force the gas into a smaller volume, thereby compressing it. The combination of roots and rotary vane pumps in series produces a system with a higher pumping speed than either pump individually. In general, such systems are used because they are cheaper than a single, larger mechanical pump of the same capacity.

The second stage of differential pumping is carried out by a 200 L/s turbo-molecular pump backed by a 3 L/s dual-stage rotary vane pump. Turbo-molecular pumps consist of turbine blades rotating at tens of thousands of rpm that impart a net momentum transfer to the gas molecules in the direction of compression. The turbo-molecular pump in our lab uses magnetic suspension of its ball bearings on its high vacuum side and is therefore very clean.

The final stage of pumping consists of a 6 in., 1200 L/s diffusion pump (SantoVac 5 pumping fluid) backed by a dual-stage, 3 L/s rotary vane pump. As mentioned previously, an important design consideration is that the backing pumps have sufficient capacity to back the high vacuum (HV) pumps. Figure 2.5 demonstrates that even if the HV pumps were operated at their maximum pressures, the backing pumps would be sufficient to avoid gas buildup. In each stage, the achievable throughput through the backing pumps in these conditions is larger than the throughput through the HV pumps. The three stages of differential pumping allow us to operate the detector chamber at a

pressure of ~$1x10^{-7}$ Torr under normal gas loads. The gas in this chamber has a mean free path on the order of hundreds of meters and the probability of collisions with the ion beam is negligibly small. Therefore, laser induced dissociation experiments are carried out in a collisionless environment. It is, however, sometimes useful to promote collision induced dissociation (CID) in order to see the distribution of CID products. This is accomplished by introducing argon directly into the detection chamber through a leak valve located directly above the second quadrupole. This essentially makes Q2 a collision cell.

Due to the importance of creating and maintaining a vacuum, the pressures in the apparatus are closely monitored with two types of pressure gauges. The chamber pressures are monitored with ionization gauges. These devices consist of three electrodes: a cathode to emit electrons which in turn ionize the gas, an anode that collects the stray electrons and guides the ions toward the ion collector, and an ion collector which collects the ions. The current of the ion collector is proportional to the pressure in the gauge. The output of these gauges depends on the gas and is affected by the ionization probability of the gas. Molecules that are more readily ionized (such as acetone) will give higher readings at the same pressure than molecules that have lower ionization probability (i.e. He). Ionization gauges do not operate properly at pressures above ~10^{-3} Torr because gas scattering prohibits the ions from reaching the collector, and at high enough pressures arcing may occur. Foreline gas pressures are measured using thermal conductivity gauges, which operate by measuring the amount of heat the gas will conduct away from a wire. The thermal conductivity is a function of velocity

and pressure. Therefore, the gauge will give higher readings for lighter (faster) gases than for heavier gases (slower) at the same pressure.

Ion Guiding

The ions emitted from the ion gun must be directed towards the neutral beam. Also, once the cluster ions are formed, they must be guided into the detection chamber. Electrostatic lenses and an octapole ion guide are used for these purposes (Figure 2.1). The stability of various cluster ion trajectories through the apparatus is a sensitive function of the lens voltages. The lens conditions are adjusted throughout the day in order to optimize the desired cluster ion signal. Positively biased lenses create potential barriers for cations and therefore retard the beam and act as focusing lenses. Negatively biased lenses, conversely, defocus and accelerate a cationic beam. The octapole has the same general operating principle as the RF-only quadrupole described below. Our octapole operates at 1.2 MHz with a peak to peak voltage around 200-750 V.

Mass Selection: Quadrupoles

Quadrupoles are devices which consist of two pairs of metal rods to which DC and oscillating, radio frequency (RF) voltages are applied. One pair of rods has a positive DC potential and the other has a negative potential. The RF voltage applied to the two pairs is 180^{o} out of phase. Defining the X axis as the axis containing the positive DC rods, the Y axis as containing the negative DC rods and the Z axis as the direction of ion transport, the operation of the quadrupoles can be thought of qualitatively by considering the effect of the potentials on positive ions in the X-Z and Y-Z planes[4]. In the X-Z plane, the positive potential tends to confine the ions toward the center, whereas the RF potential will induce oscillations. Heavier ions will be more affected by the average

(DC) potential, whereas lighter ions will be relatively more affected by the RF potential. Sufficiently light ions will be ejected from quadrupole. Conversely, in the Y-Z plane, the negative DC potential acts to pull the ions toward the rods. Since heavier ions will be relatively more affected by the average (DC) potential, heavier ions will be eliminated in this plane. Thus, the X-Z plane acts as a high-pass mass filter and the Y-Z plane acts as a low-pass mass filter. Together, they create a band-pass mass filter.

More quantitatively, the quadrupoles can be understood by considering the stability diagram associated with Mathieu's equation. For the simplified case of hyperbolic shaped rods, Newton's law (F=ma) in the X and Y directions can be written as[4]:

$$\frac{d^2x}{dt^2} + \frac{ex}{mr_0^2}\left[U + V\cos(\omega t)\right] = 0$$

$$\frac{d^2y}{dt^2} - \frac{ey}{mr_0^2}\left[U + V\cos(\omega t)\right] = 0$$

where U and V are the magnitudes of the DC and AC potentials, respectively, e is the charge on the ion, m is the mass of the ion, r_0 is the shortest distance from the Z-axis to the rods, and ω is the angular frequency of the AC potential. By introducing the parameters *a* and q, these equations can be converted into Mathieu's equation.

$$a = \frac{4eU}{\omega^2 r_0^2 m} \qquad q = \frac{2eV}{\omega^2 r_0^2 m}$$

Solutions of Mathieu's equations are either bounded or unbounded, which correspond to stable or unstable ion trajectories, respectively, as shown qualitatively in Figure 2.6. Quadrupoles generally perform mass scans by adjusting U and V while keeping U/V constant, limiting their operation to a particular mass scan line. For a given magnitude of U and V, only a certain range of masses will fall in the stability region. By increasing U

and V, the mass that falls in the stability region will also increase. Furthermore, the resolution can be adjusted by altering the U/V ratio. Increasing the U/V ratio corresponds to increasing the slope of the mass scan line and results in an increased mass resolution. Finally, the stability diagram also explains how quadrupoles can be operated as ion guides. By removing the DC component, the mass scan line is a horizontal line at $a = 0$ and a large number of masses will fall in the stability region. Thus in RF-only mode, the quadrupole acts as a high-pass mass filter.

Our system consists of three quadrupoles placed coaxially in series. The quadrupoles consist of 9.5 mm diameter cylindrical rods. The first and third quadrupoles are 20 cm each and are mass-selecting quadrupoles. The middle quadrupole is 60 cm (actually three closely spaced 20 cm quadrupoles) and acts in RF-only, or ion guiding mode. The RF component operates at 1.2 MHz and has a maximum peak to peak voltage of 7200 V. An ion with an average velocity of 5000 m/s (corresponding to a time of flight of 200 μs) would experience approximately 50 oscillations in the 20 cm quadrupoles. The DC component ranges from ± 200 to ± 800 V. The mass resolving quadrupoles have a maximum mass of 2000 AMU. The resolution of the quadrupoles can be adjusted and is capable of achieving 1 AMU resolution.

Ion Detection

The cation detection scheme is shown schematically in Figure 2.7. Positive ions strike the conversion dynode, which causes the ejection of approximately four electrons per ion. The electrons are attracted to the positively charged electron multiplier. As its name implies, the electron multiplier outputs approximately 10^7-10^8 electrons per electron input. The output of the electron multiplier is an approximately 10 ns, 1 mV

pulse which is sent through a 1.2 MHz notch filter to filter out any noise caused by the quadrupoles. The signal is then sent through a three stage preamplifier to achieve a 125x amplification. The amplified signal is passed through a discriminator which ignores any pulses smaller than the threshold limit in order to filter out noise caused by thermal electrons or other sources. Any pulses greater than the threshold originate from true ion signal and result in an approximately 50 ns, 2.5 V TTL output from the discriminator. The length of this pulse determines the maximum obtainable signal in pulse counting mode. If the pulses were evenly spaced, they would overlap at $2x10^7$ counts/sec. In practice, we keep the signal below 10^6 counts/sec. At this rate, on average the pulses would be spaced by $\sim 10^{-6} s$, leading to a ratio of spacing to pulse width of:

$$\frac{\text{Spacing between pulses}}{\text{Pulse width}} \approx \frac{10^{-6} s}{50 \times 10^{-9} s} = 20$$

Keeping the signal below this level ensures that the pulses will not overlap so each pulse can be counted. The TTL pulses from the discriminator are sent to a rate meter and a multi-channel scalar (MCS). The MCS sums the signal it receives in time windows, called channels. The maximum resolution of the MCS is 2μs per channel.

2.3 Laser

YAG

In the Lisy lab, we study stretching vibrations in the ~2500-3800 cm^{-1} region. Photons in this frequency region are created by sum frequency and difference frequency generation initiated by the 1064 nm (9400 cm^{-1}) output of a Nd:YAG laser (Continuum Surelite II-10 Hz). The gain medium in this laser is a 115 mm long, 6 mm diameter yttrium aluminum garnate (YAG) rod doped at approximately 1% with Nd^{3+}. The rod is pumped by a xenon flashlamp, which excites the Nd^{3+} into excited pump states.

Population is then transferred into the upper laser level through a nonradiative decay process in order to achieve a population inversion between the $^4F_{3/2}$ and $^4I_{11/2}$ levels[5], Figure 2.8. If the laser begins to lase before the population density in the upper state reaches its maximum potential, then the maximum gain and output energy is not achieved. In order to avoid this, Q-switching is used. The theory of Q-switching is to destroy the laser cavity while the gain medium is being pumped in order to allow the maximum population inversion. Then, the laser cavity is rapidly restored and a pulse of energy at the maximum gain is produced. In the Surelite II, Q-switching is accomplished with a combination of a polarizer, a quarter wave plate, and a Pockels cell[6] as shown in Figure 2.9. The Pockels cell acts as a transparent element when no voltage is applied to it, but as an additional quarter wave plate when ~-4 kV is applied. Therefore, when there is no voltage on the Pockels cell, the beam will pass through the quarter wave plate twice, changing it from horizontal to vertical polarization, and be ejected by the polarizer. When a voltage is applied to the Pockels cell, the beam will pass through a total of four quarter wave plates thereby preserving the horizontal polarization and allowing amplification. So, the flashlamp is fired when the laser cavity is destroyed in order to build maximum population in the upper laser level. Approximately 185-235 μs after the flashlamp discharge is initiated, a Marx bank is used to very quickly (0 to -4 kV in ~20 ns) apply a voltage to the Pockels cell. This results in an approximately 520-750 mJ, 10 ns pulse.

OPO/OPA System

The horizontally polarized output of the YAG laser is directed into a LaserVision OPO/OPA system in order to create a tunable IR output. A schematic of the system is

shown in Figure 2.10. After passing through a telescope inside the LaserVision system, the 1064 nm beam is split into two. One of the 1064 nm beams is directed through a Potassium Titanyl Phosphate (KTP) crystal which acts as a frequency doubler. This is an example of a second order non-linear optical effect which is possible when light is passed through a crystal with a nonzero second order optical susceptibility. As depicted in Figure 2.11, the frequency doubler converts two 1064 nm photons into one 532 nm photon. The 532 nm beam then becomes the pump of the optical parametric oscillation (OPO) setup. The OPO consists of a KTP crystal placed in an optical cavity. Phase matching and frequency selection is accomplished using angle-tuning of the KTP crystal. The angle is controlled by a stepper motor which is remotely controlled by a computer. The OPO process is an example of difference frequency generation. As shown in Figure 2.11, the desired output from this stage is the idler component, which is at the mid-IR frequency desired with a bandwidth of ~3cm^{-1} [7]. This idler component is then sent to the optical parametric amplification (OPA) stage. The mid-IR beam is combined with the non-frequency doubled portion of the 1064 nm beam and sent through a series of four Potassium Titanyl Arsenate (KTA) crystals which are used because of their extended mid-IR transparency. The mid-IR beam is amplified through another difference frequency generation process as shown in Figure 2.11. Finally, the output of the OPA is filtered and the mid-IR component is sent to the TQ. The energy output of the OPA depends on a number of factors including the YAG energy, alignment of KTA crystals, and frequency. Above 3000 cm^{-1}, the output ranges from ~5-15 mJ/pulse. Below 3000 cm^{-1}, the energy gradually drops off from around 5 mJ/pulse at 2800 cm^{-1} to ~2 mJ/pulse at 2400 cm^{-1}.

Infrared Beam

The IR beam exiting the OPO/OPA system first enters a telescope consisting of two CaF_2 lenses as shown in Figure 2.12. The two lenses are separated by approximately 26.3 cm, producing a gradually focused beam which achieves its beam waist in the middle of the second quadrupole. A photoacoustic microphone is placed near the focal point of the first telescope lens. The microphone is sensitive to shock waves produced by atmospheric water absorbing IR radiation in the O-H stretching region[8] (~3400-4000 cm^{-1}). The output of the microphone is proportional to the absorption cross section of water (assuming constant atmospheric water) and serves as a frequency reference. After exiting the telescope, the beam is turned with a protected silver mirror. As shown in Figure 2.13, protected silver coating provides nearly 100% reflection in the relevant mid-IR region. The beam is then split into two components with a CaF_2 beam splitter. Approximately 10% of the beam is directed to another beam splitter which directs the beam toward a pyroelectric detector and the reference cell. The output of the pyroelectric detector directly after the second beam splitter is used for energy calibration by assuming that it is proportional to the laser energy entering the TQ. The detection element in our pyroelectric detectors is a lithium tantalite ($LiTaO_3$) crystal which will heat up when subjected to a laser pulse, causing the lattice spacing of the crystal to change[9]. When electrodes are connected to the crystal, this change can be detected because a current is produced which is proportional to the rate of change of temperature. The output current is sent through a resistor and produces a voltage which is directly proportional to the energy of the laser pulse. The other part of the beam coming from the second beam splitter is sent through a cell containing a reference gas, usually CH_4 or HCl. The

pyroelectric detector located directly after the cell records the energy of the beam coming out. Clearly, the beam will be depleted by the absorption of radiation by the reference gas according to Beer's law. Thus, the output of this detector is used as a frequency calibration in a frequency region which depends on the type of gas. For CH_4 and HCl, this corresponds to the C-H stretch region of ~2900-3200 cm^{-1} and the H-Cl stretch region of ~2600-3100 cm^{-1}, respectively.

Ninety percent of the beam passes through the first beam splitter and is then elevated to the height of the TQ entrance. The elevator mirrors are also used to align the beam through the apparatus' aperture, which is sealed using a sapphire window, and down the quadrupole axis. Proper alignment is achieved by aligning to two points: the aperture entrance to the TQ and a pyroelectric detector located on axis in the turbo chamber. As mentioned previously, the telescope is used to produce a gradually focusing beam which has a beam waist in the middle of the second quadrupole. The beam waist varies with the frequency but is in the neighborhood of 0.2 cm, leading to a Rayleigh length of over a meter. Periodically during data acquisition, the laser energy is measured at the entrance to the TQ in order to calibrate pyroelectric detector readings.

2.4 Data Collection and Analysis

Time of Flight

The time of flight (TOF) is the time it takes a cluster to travel from the entrance of the first quadrupole to the detector. This is a function of the source conditions (especially the ion gun bias) and the mass of the clusters. Experimentally, the TOF is determined by pulsing lens $Q_{1,in}$ while Q1 and Q3 mass select the cluster ion of interest. The MCS card records the signal at the detector as a function of time after the pulse. The 5 V, ~20 μs

pulse on $Q_{1,in}$ causes a perturbation to the ion beam. It takes a time equivalent to the TOF for this perturbed signal to reach the detector.

Mass Spectra

By setting Q3 to ion guiding mode and mass scanning with Q1, mass spectra can be obtained. Mass spectra give the abundance of ions in the molecular beam (in counts per second) vs. mass-to-charge ratio. The mass is usually scanned in 0.5 or 1 AMU steps with an acquisition time of 0.2 sec at each mass. This data is typically collected before IR spectra in order to determine the clusters present in the beam.

Mass Spectra/Mass Spectra

By setting Q1 to mass select a specific mass and mass scanning with Q3, MS/MS data can be obtained. This data provides information on the dissociation products of the cluster selected by Q1. If no argon is leaked into the detection chamber through a leak valve, then the only dissociation pathway is unimolecular dissociation. When argon is introduced into the detection chamber, collision induced dissociation will cause additional fragmentation. Currently, mass spectra/mass spectra are used primarily to verify the identity of the parent cluster and to identify the prominent loss channels.

Infrared Predissociation Spectra

Predissociation spectra are obtained by setting Q1 to mass select a parent cluster and Q3 to mass select a fragment ion. After the parent ion passes through Q1, it enters the ion guiding region of Q2 where it interacts with the IR laser. Photon absorption can cause fragmentation. The only fragment ions which will reach the detector are determined by the mass selection of the third quadrupole. Figure 2.14 shows a schematic representation of the data collection for an idealized IRPD experiment of a cluster with a

TOF equal to 200 μs. The laser pulses at time t=0 causing 50% fragmentation of the parent clusters in Q2. It takes 40 μs for the first bit of signal to reach the detector. For the next 120 μs the rest of the signal will arrive at the detector. At any time after this, any ions reaching the detector did not come from laser interaction in Q2 and can be considered noise. Thus, for IRPD experiments the signal vs. time recorded by the MCS card is divided into four windows. The first window represents the time it takes the first fragment ions to reach the detector. The second window represents the clusters coming from Q2 and gives signal for the experiment. The third window is a delay that is set to be twice as long as the first window. Finally, the fourth window is set to be the same length as the signal window and represents the background. This whole process is repeated for each laser shot. Anywhere from 600-3000 laser shots are executed at each frequency in the scan. The laser frequency is generally scanned in 3 cm^{-1} steps.

As described above, the data is separated into signal and background windows. The signal to noise ratio is defined as[10]:

$$\frac{S}{N} = \frac{Signal - Background}{\sqrt{Signal} + \sqrt{Background}}$$

The percent depletion of the parent ion is given by:

$$\%\text{Depletion} = \frac{\text{Signal(counts)} - \text{Background(counts)}}{\left[\text{I}_{\text{Parent Ion}} \left(\frac{\text{counts}}{\text{sec}} \right) \right] * \left[\text{width of signal window } (\text{s}) \right] * \left[\text{\# of laser shots} \right]} \times 100$$

where $I_{Parent\ Ion}$ is the intensity of the parent ion reaching the detector in the absence of the laser when Q3 is set to pass the parent. The parent ion intensity is measured twice for each laser frequency, once before the initiation of the laser pulses and once after. The

value used in the percent depletion calculation is an average of the two measurements. Finally, the dissociation cross section is calculated with the formula:

$$\sigma\left(cm^2\right) = -\frac{\log\left(1 - \%Dep/100\right)}{\text{Laser Fluence}\left(\text{cm}^{-2}\right)}$$

$$\text{where:} \qquad \text{Laser Fluence}\left(\text{cm}^{-2}\right) = \frac{\#\ photons}{\pi r^2}$$

$$\#\ photons = \frac{\text{Laser power at TQ entrance } \left(\text{mJ/pulse}\right)/1000}{\text{Photon energy (J/photon)}}$$

IRPD spectra are then displayed as cross section vs. frequency plots.

2.5 Conclusions

This experimental setup, and minor variations thereof, has proven to be very useful in the production and detection of a wide variety of cluster ions. The laser setup provides a reliable source of energy in the O-H and C-H stretching regions. Through IRPD experiments, information on cluster formation and geometries and the interplay between various non-covalent interactions has been obtained with several examples given in this dissertation.

2.6 Figures

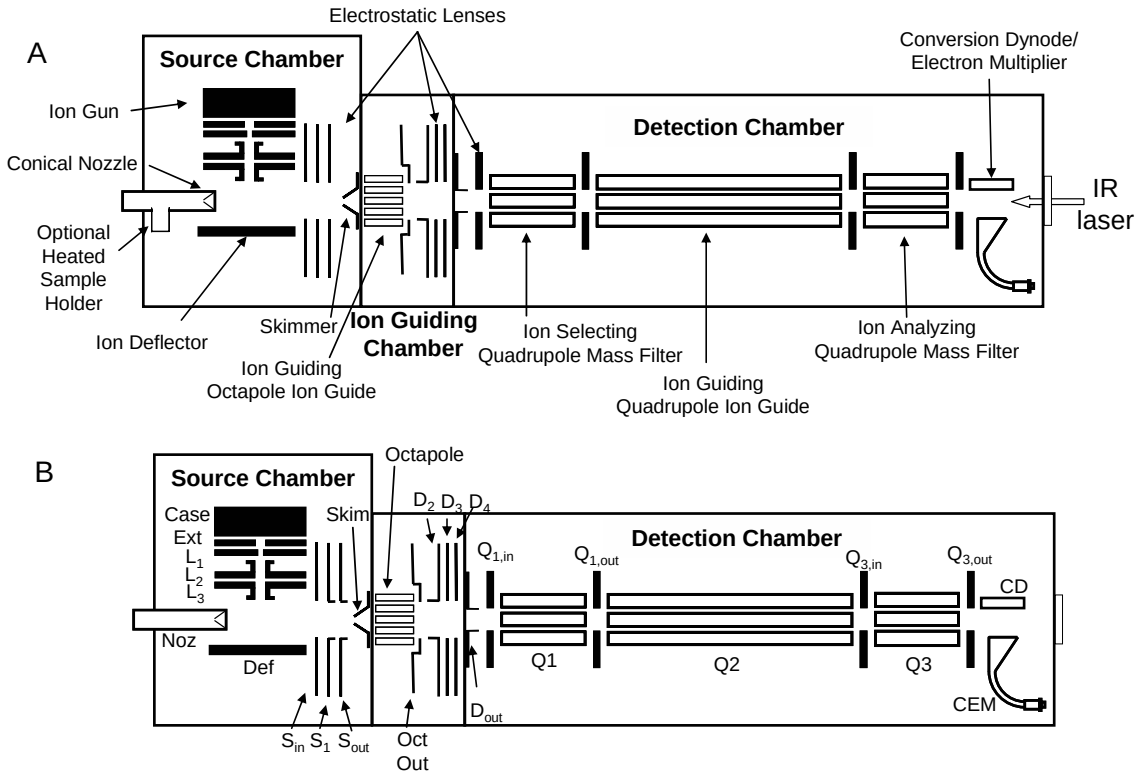

Figure 2.1. Schematic representations of the triple quadrupole apparatus showing A) the various components and B) the labels for each component.

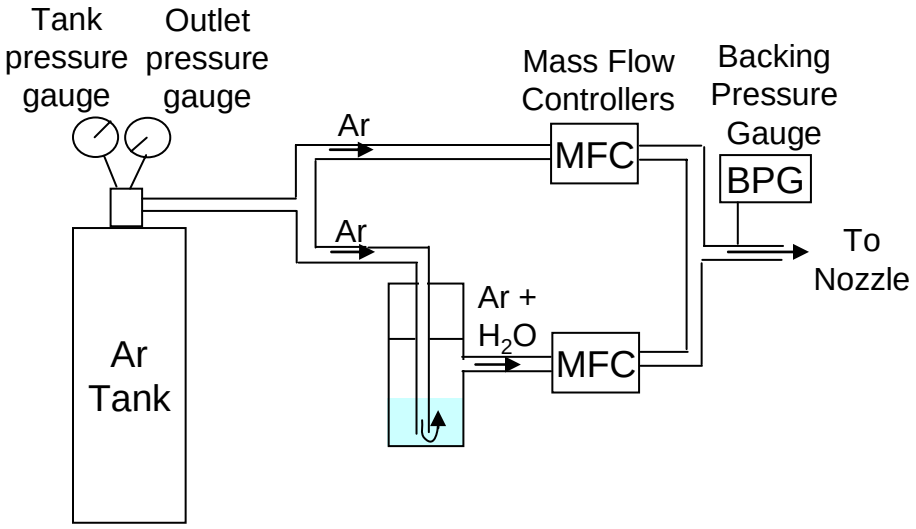

Figure 2.2. Schematic representation (not to scale) of gas flow prior to the nozzle. The two mass flow controllers can be set independently of one another in order to control the gas mixture composition.

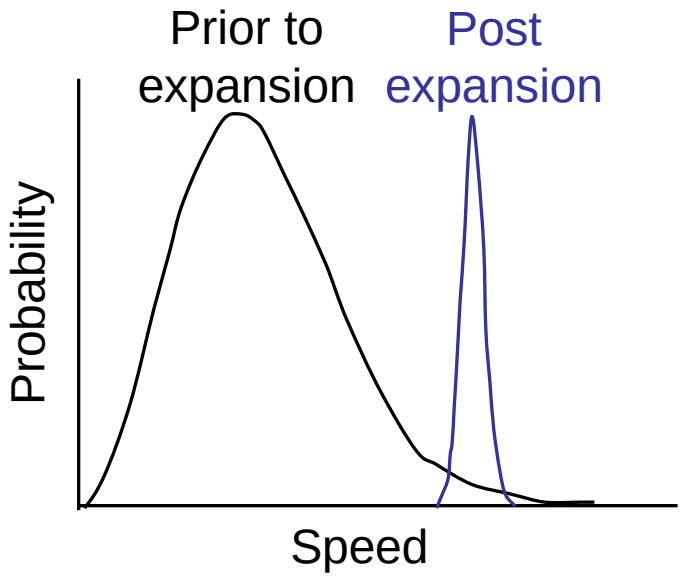

Figure 2.3. Representation of the speed distributions of a gas pre- and post-expansion. The average velocity increases and the temperature decreases. Reproduced from texts by Atkins and McQuarrie[11,12].

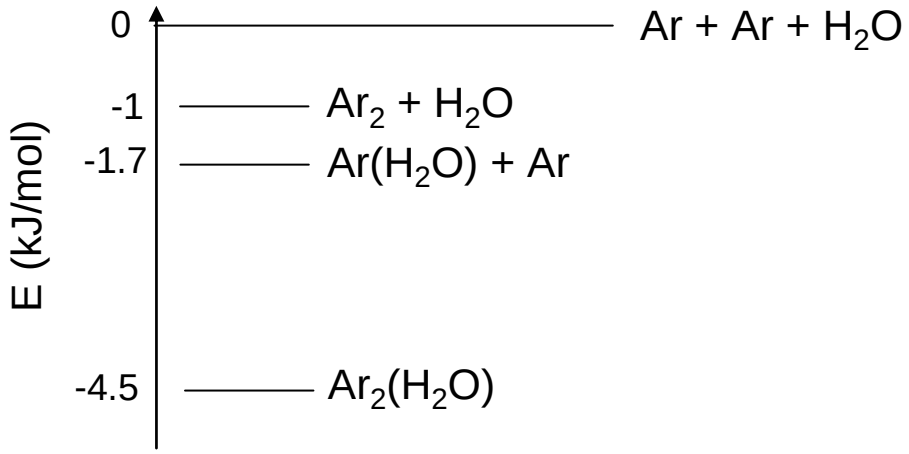

Figure 2.4. This energy diagram shows the relative energies of argon and argon/water clusters.

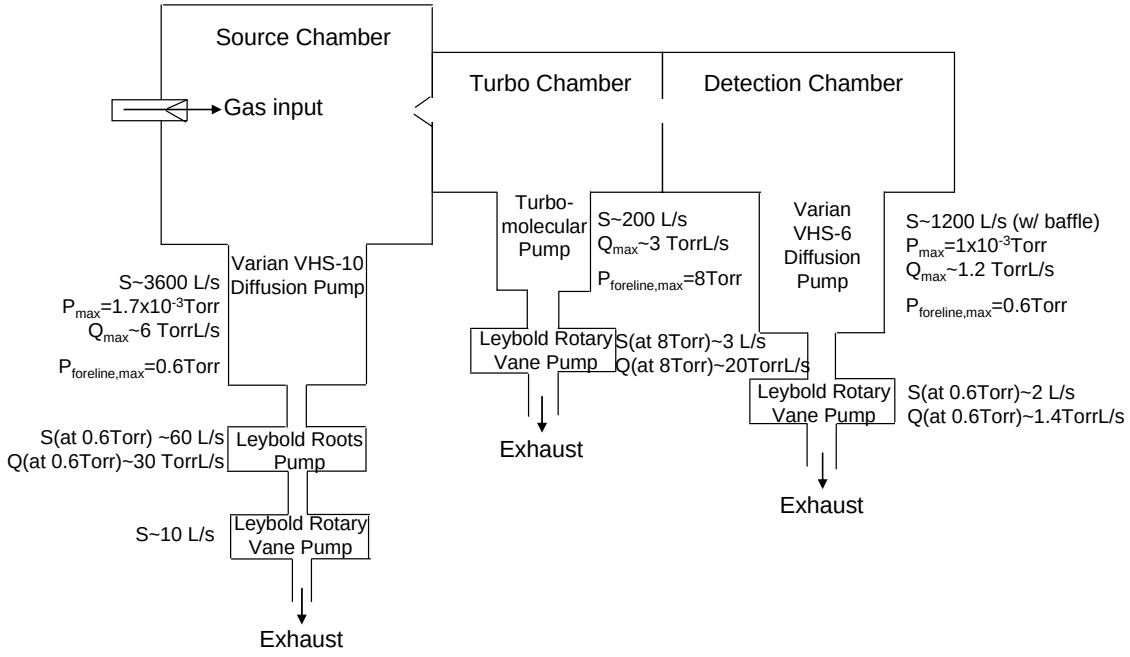

Figure 2.5. Schematic of the vacuum system for the triple quadrupole apparatus. Even when the high vacuum pumps are operated with maximum throughput and with maximum foreline pressure, the backing pumps are sufficient to ensure no gas buildup. S = pumping speed, Q = Pump throughput.

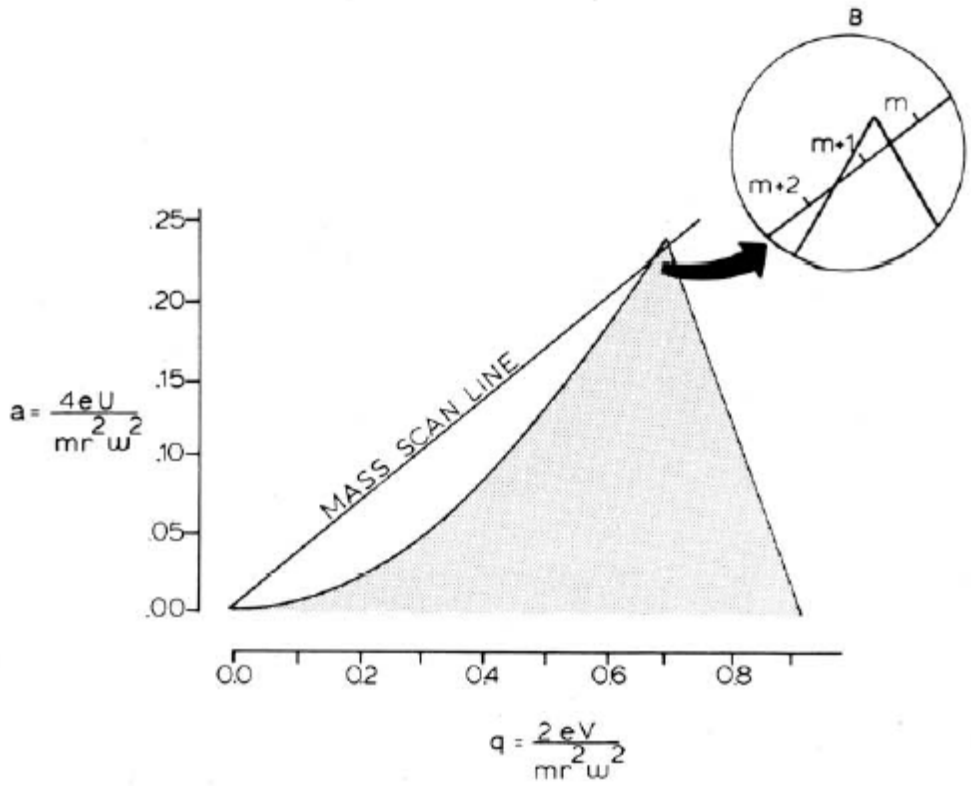

Figure 2.6. The stability diagram for a quadrupole. The shaded area represents stable trajectories. The mass scan line represents a line of constant U/V. Figure taken from Denton, et. al[4].

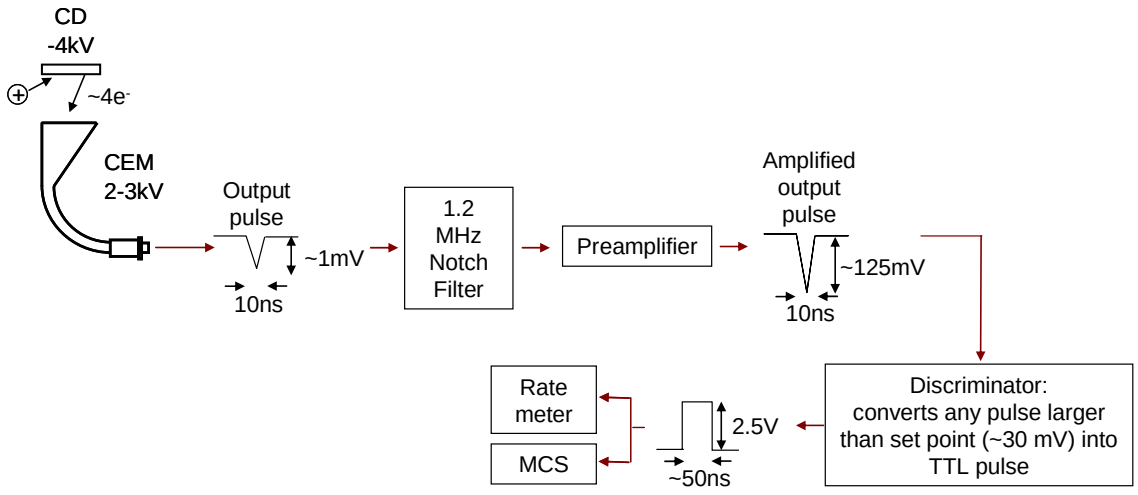

Figure 2.7. Schematic representation of the pulse counting setup used for cation detection.

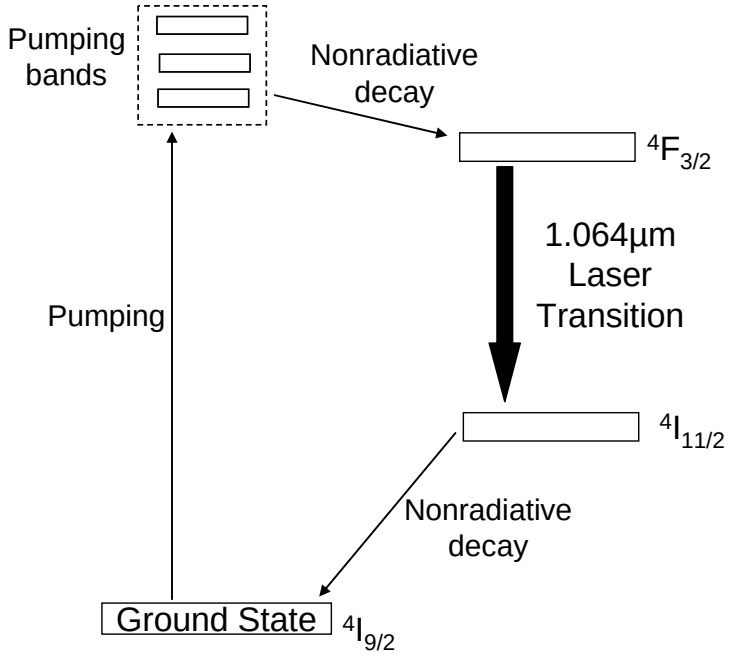

Figure 2.8. Energy level diagram for Nd^{3+}, the lasing material in a Nd^{3+} YAG laser. This is a four level, pump-and-transfer lasing process. Reproduced from *Laser Fundamentals*[5].

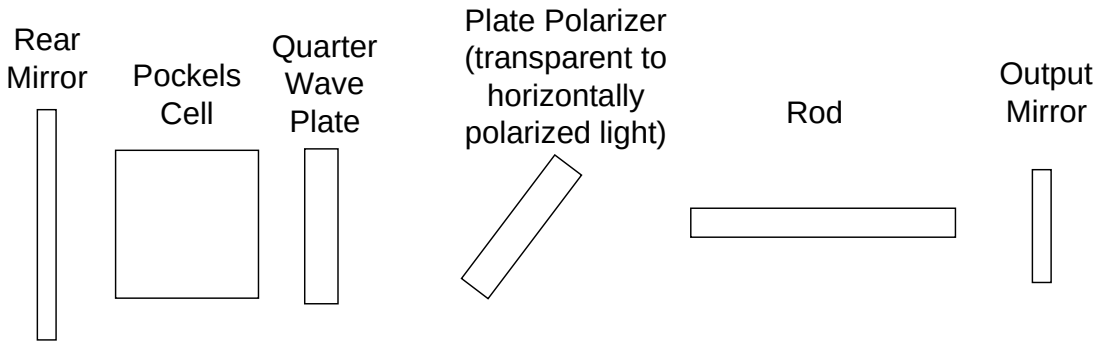

Figure 2.9. A schematic representation of the Surelite laser cavity[6].

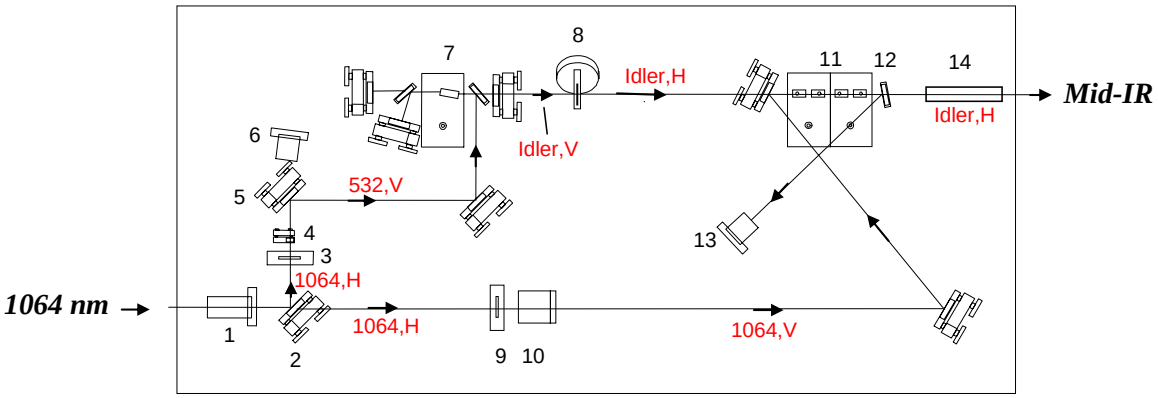

Figure 2.10. A schematic representation of the OPO/OPA system adapted from the LaserVision manual[7]. Values in red represent the relevant beams where numbers are wavelengths in nm and H and V represent horizontal and vertical polarization, respectively. 1: telescope, 2: beam splitter, 3: adjustable half-wave plate, 4: KTP frequency doubling crystal, 5: 532 nm reflective mirror, 6: 1064 nm beam dump, 7: OPO cavity containing KTP crystal, 8: half wave plate, 9: adjustable half-wave plate, 10: polarizer – passes vertically polarized light 11: OPA KTA crystals, 12: dichoric to remove 1064 nm, 13: 1064 nm beam dump, 14: polarizer to remove high frequency component of OPA

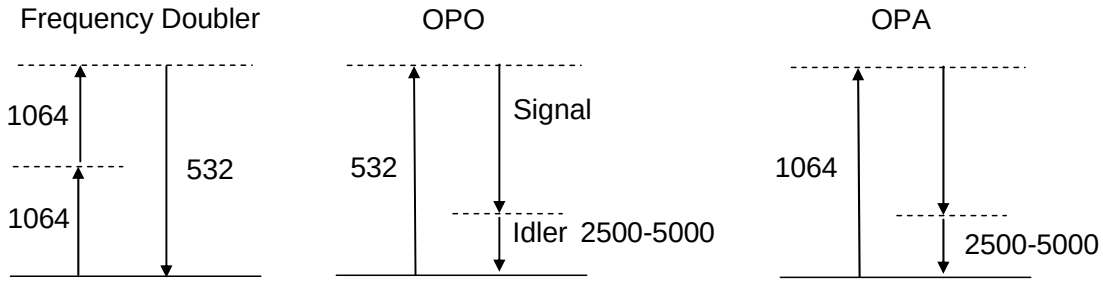

Figure 2.11. Schematic representation of frequency doubling and the OPO and OPA processes. All values are in nm.

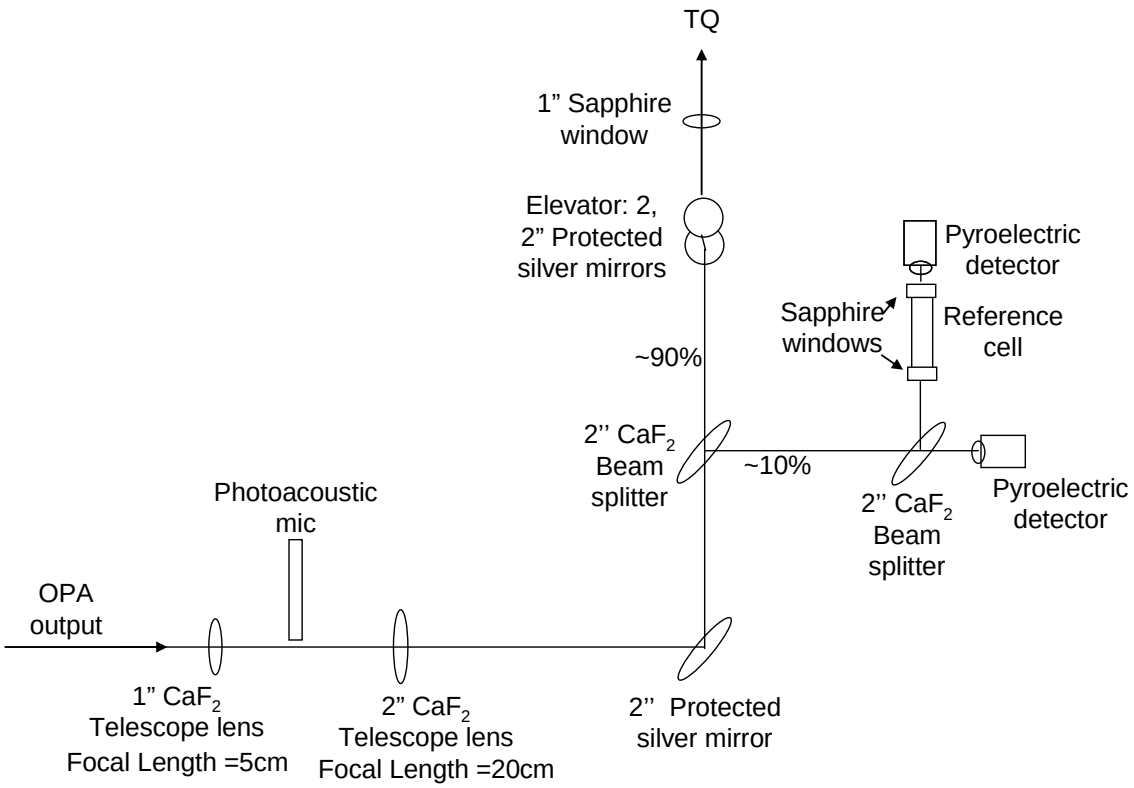

Figure 2.12. Laser table setup for focusing and steering the IR beam into the triple quadrupole apparatus.

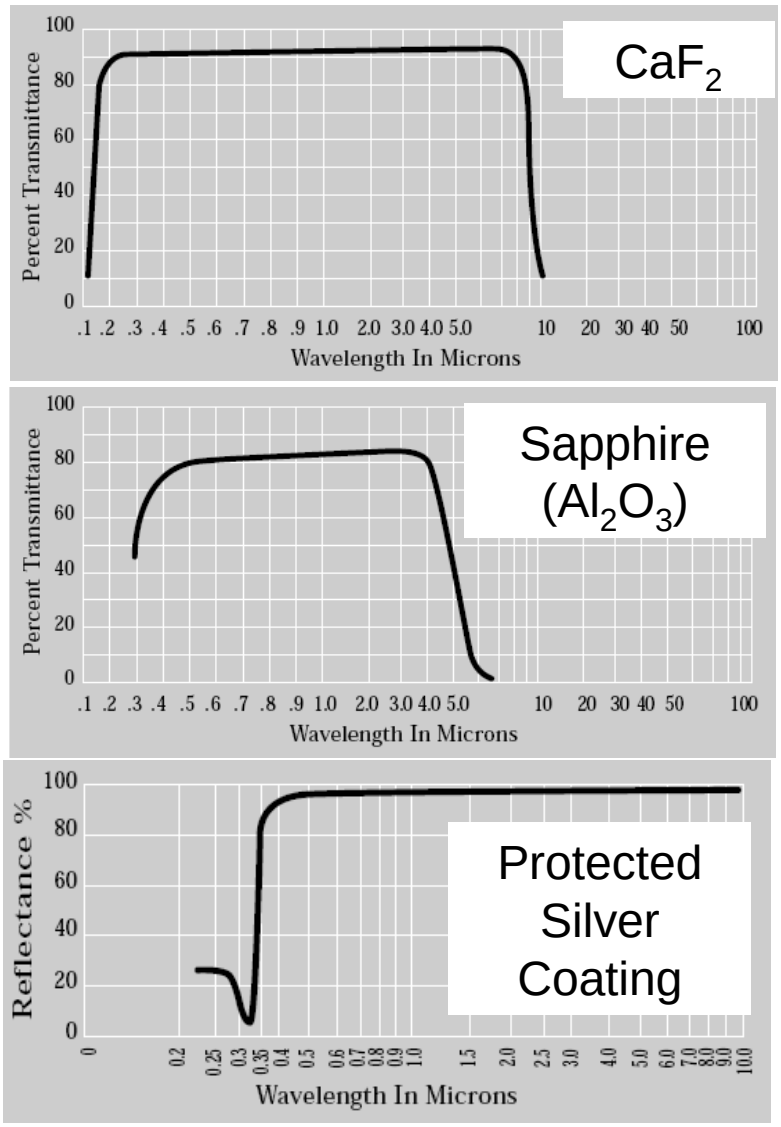

Figure 2.13. Transmittance and reflectance properties of various IR optics[13].

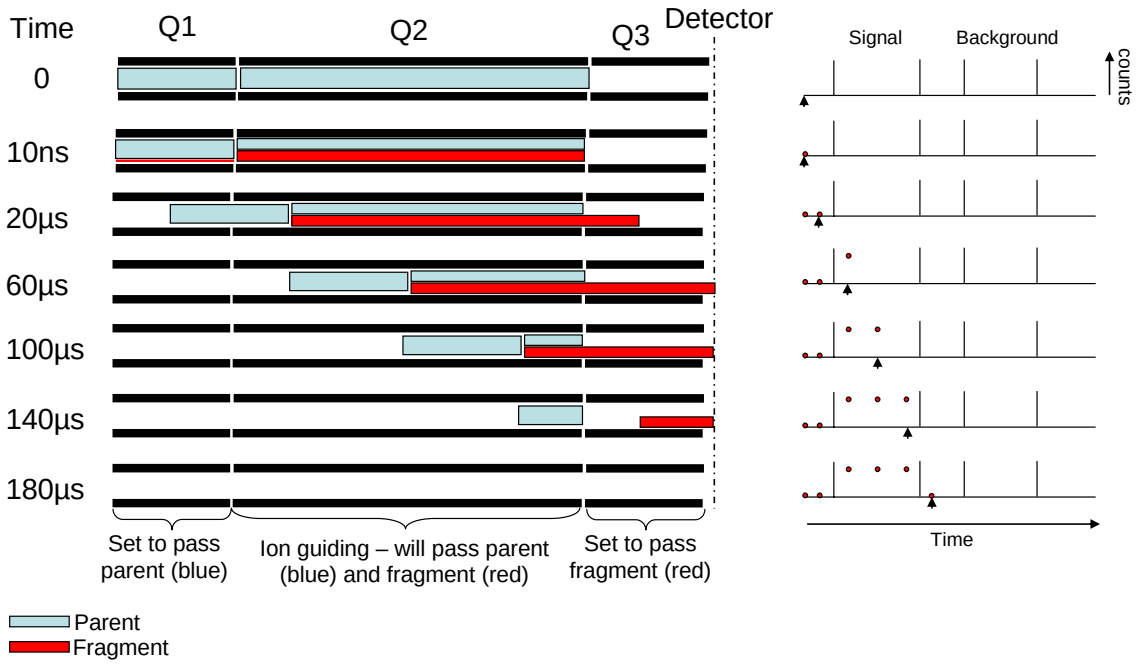

Figure 2.14. A schematic representation of an idealized IRPD experiment. The laser fires at time zero and causes 50% fragmentation of the ions in the second quadrupole and a small amount of fragmentation in the first quadrupole. The time of flight for this cluster is 200 µs.

2.7 Tables

Table 2.1. Typical values for the operation of the triple quadrupole apparatus for the production of solvated alkali metal ion clusters.

Component	Value	Unit
Ar pressure	8	psig
Flow Ar	50	sccm N_2
Flow Ar/H_2O	100	sccm N_2
Backing Pressure (P_b)	400-600	Torr
Source Chamber Pressure	$4x10^{-4}$	Torr
Source Foreline Pressure	40	mTorr
Turbo Chamber Pressure	$5x10^{-5}$	Torr
Turbo Foreline Pressure	20	mTorr
Detector Chamber Pressure	$1x10^{-7}$	Torr
Detector Foreline Pressure	10	mTorr
Ion Gun Filament Current	2.8	Amp
Ion Gun Filament Bias	26	V
Case	50	V
Ext	-20	V
L_1	-300	V
L_2	50	V
L_3	-300	V
Noz	15	V
Def	10	V
S_{in}	18	V
S_1	20	V
S_{out}	22	V
Skim	-10	V
Octapole peak-to-peak RF	730	V
Octapole RF	1.2	MHz
Octapole Float Bias	-300	V
Oct Out	-100	V
D_2	-80	V
D_3	-100	V
D_4	-30	V
D_{out}	-5000	V
$Q_{1,in}$	0	V
$Q_{1,out}$	-50	V
$Q_{3,in}$	-50	V
$Q_{3,out}$	0	V
CD	-4000	V
CEM	2500	V
Discriminator	30	mV

Table 2.2. Compilation of ionization potentials and work functions for the alkali metals used in the Lisy lab[14].

Metal	Ionization Potential, Φ (eV)	Work Function, ϕ (eV)	Φ - ϕ (eV)
Li	5.3917	2.93	2.5
Na	5.1391	2.36	2.8
K	4.3407	2.29	2.1
Rb	4.1771	2.261	1.9
Cs	3.8939	1.95	1.9

2.8 References

(1) Miller, D. R. Free Jet Sources. In *Atomic and Molecular Beam Methods*; Scoles, G., Ed.; Oxford University Press: New York, 1988; Vol. 1; pp 14.

(2) Kappes, M.; Leutwyler, S. Molecular Beams of Clusters. In *Atomic and Molecular Beam Methods*; Scoles, G., Ed.; Oxford University Press: New York, 1988; Vol. 1; pp 380.

(3) Draves, J. A.; Luthey-Schulted, Z.; Liu, W.-L.; Lisy, J. M. *The Journal of Chemical Physics* **1990**, *93*, 4589.

(4) Miller, P. E.; Denton, M. B. *Journal of Chemical Education* **1986**, *63*, 617.

(5) Silfvast, W. T. *Laser Fundamentals*; Cambridge University Press: Cambridge, 1996.

(6) Operation and Instruction Manual for Surelite Lasers Santa Clara, CA, 2002.

(7) Guyer, D., LaserVision Manual.

(8) Weinheimer, C. J. The Role of Hydrogen Bonding in Alkali Metal Ion Solvation, University of Illinois at Urbana-Champaign, 1998.

(9) Molectron Pyroelectric Detector/Amplifiers Manual Santa Clara, CA, 1985.

(10) Corbett, C. A. Study of the Interplay Among Non-covalent Interactions in Structural Determination of Gas Phase Cluster Ions, University of Illinois at Urbana-Champaign, 2001.

(11) Atkins, P.; de Paula, J. *Physical Chemistry*, 7 ed.; Oxford University Press: New York, 2002.

(12) McQuarrie, D. A.; Simon, J. D. *Physical Chemistry A Molecular Approach*; University Science Books: Sausalito, 1997.

(13) ISP Optics Infrared Catalog Irvington, NY, 2007.

(14) *CRC Handbook of Chemistry and Physics*; 89 ed.; Lide, D., R, Ed.; CRC Press, 2008.

Chapter 3: Cooperatively Enhanced Ionic Hydrogen Bonds in $Cl^-(CH_3OH)_{1-3}Ar$ Clusters[‡]

3.1 Introduction

Starting in the late 1990s, a number of papers were published describing the structure of small cluster ions consisting of a halide anion and solvent molecules capable of hydrogen bonding[1-12]. One of the key questions addressed was whether the ions were surface or interiorly solvated. The cluster ions $X^-(H_2O)_n$ showed evidence of surface solvation for X = Cl, Br, and I[1,3,8] with $n \leq 5$, whereas $F^-(H_2O)_n$ was interiorly solvated[2,6,13]. These results showed the ability of the relatively small fluoride ion to disrupt the hydrogen bonding network of the water molecules in favor of the anion···water ionic hydrogen bonds (IHB). The question was then raised whether the nature of the solvent, specifically the dual OH nature of water, was responsible for the asymmetric solvation. This was addressed by using methanol as the solvent. Interestingly, it was shown that $X^-(CH_3OH)_n$ (X = F, Cl, and I) were *all* surface solvated[7,9,11,12]. Thus, the nature of the solvent was shown to play an important role in the solvation of the fluoride ion.

The significant ion-solvent binding energies led to relatively high internal energies and broad spectra, so the technique of noble gas tagging was introduced to sharpen the spectral features of these systems[2-5,11,12]. In 2002, Johnson and coworkers studied $I^-(CH_3OH)_{1-2}Ar$ cluster ions[12], selecting the large halide ion iodide to promote the

[‡] Reproduced in part and reprinted with permission from Jordan P. Beck and James M. Lisy. Journal of Physical Chemistry A. 2010, 114 (37), pp. 10011-10015. Copyright 2010 American Chemical Society.

formation of hydrogen-bonded configurations. Two conformers were identified for $I^-(CH_3OH)_2Ar$: one with both methanols bound directly to the iodide anion and another where the two methanols formed a hydrogen-bonded dimer bound to the anion. The OH stretch of methanol bound to the anion in the latter structure exhibited an enhanced ionic hydrogen bond (EIHB) as reflected by a red-shift of ~235 cm^{-1} compared to the OH stretches in the other conformer where both methanols are in the first solvent shell.

In this chapter, results of the infrared predissociation spectra of $Cl^-(CH_3OH)_{1-3}Ar$ are reported. This offers the possibility of comparing the effects of the smaller chloride ion to the previous work on iodide. Due to its smaller size and larger charge density, the chloride ion is expected to act as a more effective structure-breaker than iodide. This was the case when comparing the spectra of the warm, non-argonated $I^-(CH_3OH)_n$[12] and $Cl^-(CH_3OH)_n$ clusters[7]. For iodide, there is a small peak from a hydrogen bonded structure already at n=2. In contrast, the $Cl^-(CH_3OH)_n$ spectra show no indication of hydrogen bonding through n=3. Thus, by using chloride in the present argon tagged study we can test whether lower internal energies can thwart the structure breaking ability of chloride and trap out hydrogen-bonded conformers. Secondly, we have expanded our study to include up to three methanols. This allows the solvent methanols to potentially form more extensive hydrogen bonded networks, creating cooperatively enhanced hydrogen bonds with very large frequency shifts.

3.2 Experimental and Computational Details

The spectra presented in this chapter were acquired using the triple-quadrupole mass spectrometer and IR laser described in detail in chapter 2. *Ab initio* calculations were carried out to aid in interpreting the experimental spectra. Locally stable

conformers of $Cl^-(CH_3OH)_{1-3}$ were calculated using GAUSSIAN 03 optimization procedures. For each of the optimized structures, harmonic frequency calculations were carried out. The calculated frequencies were scaled by a factor of 0.9576 so that the calculated frequency of the OH stretch of neutral methanol matched with its gas-phase experimental value[14] of 3681 cm^{-1}. All of the calculations were performed with an aug-cc-pVDZ basis set using the GAUSSIAN 03 software package[15] at the MP2 level of theory.

3.3 Results and Discussion

Spectra of the $Cl^-(CH_3OH)_nAr$, n=1-3 series were obtained in the CH and OH stretching regions. Since the hydrogen bonded OH stretches for the n=2-3 clusters are shifted into the CH stretching region, spectra of the singly deuterated methanol clusters were obtained to aid in assignment of the spectral features. The OD stretches of d_1-methanol are shifted well below the spectral region covered in these experiments so the $Cl^-(CH_3OD)_nAr$ spectra only contained peaks associated with CH stretches. Thus, peaks present in $Cl^-(CH_3OH)_nAr$ spectra but not in the corresponding $Cl^-(CH_3OD)_nAr$ spectra can be positively identified as involving methanol OH stretches.

We will start by analyzing the relatively straightforward spectrum of the $Cl^-(CH_3OH)_1Ar$ cluster ion, the black trace in Figure 3.1. Also shown in Figure 3.1 is the IRPD spectrum of $Cl^-(CH_3OD)_1Ar$, the red trace, which clearly demonstrates that the spectral features below the small peak at 3005 cm^{-1} are due to methyl CH stretches. The prominent feature, a doublet centered at 3097 cm^{-1}, can easily be assigned to the methanol OH stretch which forms a hydrogen bond with the chloride anion. Such ionic hydrogen bonds are known to create large red-shifts which depend on the size of the

anion[1-3,5,6,9,12]. The previously reported[7] OH stretch for the IHB in the non-argonated $Cl^-(CH_3OH)_1$ is centered at 3162 cm^{-1}, shifted 519 cm^{-1} to the red of the neutral, gas phase methanol OH stretch of 3681 cm^{-1}. The addition of the argon atom to the cluster shifts the IHB peak an additional -65 cm^{-1} to 3097 cm^{-1}. The red shift of spectral features upon addition of messenger atoms is well documented[16-19] and has been discussed extensively in the case of $I^-(CH_3OH)_nAr_m$[11,12], where the shift from the addition of a single Ar atom was ~-30 cm^{-1}. Since this red shift is due to the thermal effect of quenching out low frequency ion···methanol stretching modes, it is reasonable that the shift in the chloride case is approximately twice that of the iodide case. The binding energy of $Cl^-(CH_3OH)_1$ is ~20 kJ/mol greater than the binding energy of $I^-(CH_3OH)_1$. Under the evaporative ensemble conditions, $Cl^-(CH_3OH)_1$ will have more internal energy and more excitation of the low frequency ion•••methanol stretching modes. Therefore, cooling the clusters by argon tagging will have a larger effect on the chloride clusters than on the iodide clusters, creating a larger red shift.

The doublet structure of the dominant peak may be due to multiple conformations of the $Cl^-(CH_3OH)_1Ar$ complex. These could arise from one of two likely causes. One possibility, as demonstrated by Johnson for $I^-(ROH)_1Ar_m$ clusters[11], is from multiple argon binding sites. The different binding sites create clusters with slightly different red shifts, leading to the doublet feature observed. A second possibility is that the slight splitting of the IHB peak results from staggered and eclipsed configurations of the methyl hydrogens with respect to the chloride anion. In order to determine the likelihood that both staggered and eclipsed conformers were present, we performed *ab initio* calculations on both configurations. The staggered conformation, shown in Figure 3.1, is the lowest

energy isomer, but the eclipsed configuration is nearly iso-energetic, lying less than 1 kJ/mol higher in energy. Based on these considerations, it seems likely that both isomers are present. However, with the harmonic frequency calculations providing a splitting of only 4 cm^{-1} for the two different conformers, it is difficult to give a definite explanation for the doublet structure of the IHB OH peak.

The final assignment to make in the n=1 spectrum is the small peak at 3005 cm^{-1}. This is most likely a combination hot band involving the IHB OH stretch ($\Delta v = +1$) and a low frequency vibrational mode ($\Delta v = -1$). There is a calculated harmonic frequency at 103 cm^{-1}, which matches fairly well with the experimental value of 92 cm^{-1}.

The spectra of $Cl^-(CH_3OH)_2Ar$ and $Cl^-(CH_3OD)_2Ar$ can be seen in Figure 3.2. The deuterated spectrum was essential for sorting out the CH and OH peaks in this case. By comparing the two spectra, it is clear that the peak at 2773 and all the features above ~3000 cm^{-1} are associated with OH stretches. We anticipate two possible structural configurations, and using *ab initio* calculations, we were able to find two stable minima, labeled 2A and 2B in Figure 3.2. Structure 2A is the global minimum energy structure where both methanol ligands have an IHB. Structure 2B, which consists of a methanol dimer attached to the chloride ion, is 5.8 kJ/mol higher in energy ($D_{0,2A}$-$D_{0,2B}$) than the minimum energy structure. The addition of a second methanol into the first solvation shell, as in structure 2A, reduces the strength of the IHB compared to the n=1 structure. Thus, the OH stretches of isomer 2A are higher in frequency than the 3097 cm^{-1} peak in the n=1 spectrum. Similar to the n=1 case, we expect that the 2A OH stretches should be slightly lower in frequency for $Cl^-(CH_3OH)_2Ar$ compared to $Cl^-(CH_3OH)_2$. Based on these considerations, we assign the doublet centered at 3235 cm^{-1} and the peak at 3193

cm^{-1} to the symmetric and asymmetric OH stretches in isomer 2A. Although the calculated frequencies are once again too high, the experimental splitting of 42 cm^{-1} of these two peaks matches very well with the calculated harmonic splitting of 38 cm^{-1}.

Structure 2B has an ionic hydrogen bond and a conventional methanol-methanol hydrogen bond. The former is cooperatively enhanced by the latter and can be assigned to the peak at 2773 cm^{-1}. There are two interesting observations to be made. The first is that this peak is the most intense peak in the spectrum. In spite of being 5.8 kJ/mol higher in energy, isomer 2B is being trapped efficiently and is a major component in this ensemble of cluster ions. The second is the sheer magnitude of the red shift. At 2773 cm^{-1}, the enhanced ionic hydrogen bond OH stretching feature is shifted an additional 324 cm^{-1} to the red of the n=1 peak. The final major peak, at 3321 cm^{-1}, is assigned to the conventional hydrogen-bonded OH stretch of the second shell methanol in isomer 2B. This methanol does not interact directly with the ion and is therefore less red-shifted than the other peaks. At 3321 cm^{-1}, this second shell methanol OH stretch is still significantly red-shifted from the neutral dimer hydrogen bonded stretch at around 3570 cm^{-1} [20,21]. The influence of the ion elongates the O-H bond distance of the first shell water making the oxygen of the first shell methanol more basic. This, in turn, leads to a stronger hydrogen bond with the second shell methanol, further weakening the OH stretch and resulting in a shift from the neutral dimer value. We believe that the remainder of the peaks (most notably 2986 and 3059 cm^{-1}) come from combination bands of the intense EIHB and low frequency modes. The calculated mode involving the ion•••oxygen stretch is at 259 cm^{-1} and the mode involving the oxygen•••oxygen stretch is at 200 cm^{-1}. These frequencies agree fairly well with the two most prominent bands.

It is interesting to compare the impact of different ions on the strength of the hydrogen bonds formed in these $X^-(CH_3OH)_2Ar_m$ clusters. Table 3.1 summarizes the three components which contribute to the overall shift of the enhanced ionic bond in both $Cl^-(CH_3OH)_2Ar$ and $I^-(CH_3OH)_2Ar_3$. The shifts induced by chloride ion are between 1.5 and 2 times larger than for iodide, leading to an impressive total shift of -908 cm^{-1}.

As noted above, the harmonic frequency calculations do not adequately capture the magnitude of the shifts for the strong hydrogen bonds observed in these chloride methanol systems. Anharmonic *ab initio* calculations were attempted for these clusters, but proved to be too computationally expensive for n>1. The poor agreement between calculated and experimental frequencies motivated the following straightforward and computationally inexpensive approach to estimating the IHB and EIHB vibrational frequencies. First, the optimized geometry was obtained as described in the calculations section. Next, a one dimensional potential energy curve was obtained in the OH stretching coordinate by performing single point energy calculations at various O-H distances while keeping all other coordinates at their equilibrium values. A 1-D Schrödinger equation solver[22] was used to determine the first two vibrational energies for the OH stretch and their respective vibrationally-averaged O-H distances. Next, two 1-D potential energy curves were obtained in the O-Cl stretching coordinate with the O-H distances fixed at the value for the ground (v_{OH}=0) and first excited vibrational state (v_{OH}=1). For these calculations the O-Cl distance was varied while all other coordinates, with the exception of the O-H distance, were kept at their equilibrium values. Finally, the ground state O-Cl energy levels (v_{OCl}=0) were calculated for each of the O-Cl (v_{OH}=0,1) potentials. Thus, by comparing the $v_{OH}=0 \rightarrow v_{OH}=1$ energy splitting at large O-Cl

distances and at the vibrationally-averaged ground state distances, we have a straightforward way to evaluate the influence of the anion on the OH stretch involved in the IHB. These series of calculations were carried out for the IHB in $Cl^-(CH_3OH)_1$ and the EIHB in the 2B structure of $Cl^-(CH_3OH)_2$. The results of the calculations for n=1 are shown in Figure 3.3, where, for ease of interpretation, the O—Cl potential for v_{OH}=1 has been shifted so that the asymptotic v_{OH}=0 → v_{OH}=1 energy splitting matches the gas phase methanol value of 3681 cm^{-1}. In Figure 3.3, the v_{OH}=0 → v_{OH}=1 transition with OCl in the ground state is calculated to be at 3081 cm^{-1}. Considering the simplicity of the calculations, the agreement with the experimental value of 3097 cm^{-1} is quite good. Likewise, the results for the 2B structure of $Cl^-(CH_3OH)_2$ are shown in Figure 3.4. In this case, the potentials have been shifted to match the gas phase value of the free OH stretch of methanol dimer[21], 3684 cm^{-1}. The calculated value of the EIHB OH stretching frequency of 2767 cm^{-1} is very close to the experimental value of 2773 cm^{-1}. Given the consistent agreement between the results of these calculations and experiment, we are confident in our assignments of the prominent peaks in the n=1 and 2 spectra to the IHB and EIHB OH stretches, respectively. These calculations also indicate that the ionic hydrogen bonds lead to the most anharmonic effects in the OH stretch, while terminal methanol molecules, secured by conventional hydrogen bonds, are least perturbed by the ion, and the calculated harmonic frequencies match fairly well with experiment.

For n=3, the third methanol adds a great deal of complexity to the calculations in the search for stable minima on the potential energy surface. We have identified three local minima on the potential energy surface which correspond to the isomers labeled 3A, 3B, and 3C in Figure 3.5. Isomer 3A, in which all three methanols directly bind to the

ion, is the global minimum energy isomer. Isomer 3B has two methanols interacting directly with the ion and the third methanol in a second solvent shell secured by a conventional hydrogen bond. The highest energy isomer, 3C, calculated to be 8.8 kJ/mol above the minimum, consists of a methanol trimer chain terminated by an IHB to the ion. Although an additional optimized conformer was located with one methanol in the first solvent shell acting as a double H-bond acceptor to two methanols in the second shell, it was not deemed relevant for two reasons. First, it was calculated to be an additional 3.3 kJ/mol above the 3C isomer. Second, the double acceptor motif would be very unlikely to form with our method of cluster ion generation (*vide infra*).

The spectra of $Cl^-(CH_3OH)_3Ar$ and $Cl^-(CH_3OD)_3Ar$ are shown in Figure 3.5. The most notable feature of the $Cl^-(CH_3OH)_3Ar$ spectrum is the OH stretching peak centered at 2733 cm^{-1}. Since this peak is 40 cm^{-1} lower in frequency than the EIHB peak from conformer 2B, it must arise from an even stronger hydrogen bond. Only isomer 3C would be expected to have a hydrogen bond stronger than the EIHB in isomer 2B. Adding the third methanol to the methanol chain increases the cooperative enhancement of the ionic hydrogen bond, shifting it to lower frequency. Although the calculated harmonic frequencies are consistently high, the calculated shift of the EIHB from isomer 2B to 3C of -44 cm^{-1} is very close to the experimental shift of -40 cm^{-1}. The third shell methanol OH stretch in conformer 3C would be expected to have a higher frequency than the second shell methanol in 2B or any second shell methanols in another n=3 conformer. Thus, the peak at 3396 cm^{-1} is assigned to this stretch. The second shell methanol of cluster 3C is likely partly responsible for the broad peak centered around 3054 cm^{-1}. The peak at 3257 cm^{-1} is slightly lower in frequency from the warm, $Cl^-(CH_3OH)_3$ peak,

consistent with the minimum energy 3A structure. With this assignment, all of the major peaks in the $Cl^-(CH_3OH)_3Ar$ spectrum have been assigned except the peak at 3355 cm^{-1}. It would be difficult to rationalize the presence of this peak using only conformers 3A and 3C. It seems much more likely that another conformer, such as 3B, is present in the molecular beam. The peak at 3355 cm^{-1}, which is slightly higher in frequency than the second shell methanol in conformer 2B, may then arise from the second shell methanol in 3B. The non-enhanced IHB in conformer 3B likely cannot be resolved from the IHB stretches of 3A, while the EIHB is probably part of the broad, asymmetric peak centered at 3054 cm^{-1}.

In comparison to the warm $Cl^-(CH_3OH)_3$, which has structure 3A, the rich O-H spectrum of $Cl^-(CH_3OH)_3Ar$, has revealed a number of high energy conformers. It also appears as though our $Cl^-(CH_3OH)_2Ar$ molecular ion beam contained a larger relative fraction of the dimer (2B) clusters compared to the 2A structures in contrast to the related $I^-(CH_3OH)_2Ar$ system reported by Johnson et. al[12]. This was somewhat unexpected since chloride is smaller than iodide and therefore has stronger ion•••water interactions which would not favor hydrogen bonded structures. It is important to note that the method of cluster ion generation, even with argonated species, can determine the type and distribution of conformers. In Johnson's experiments, X^-Ar_m clusters are formed, then the solvent molecules are condensed onto these clusters[11,12,23]. Condensation energy is then dissipated through argon evaporation. In our setup, we first create $(solvent)_nAr_m$ neutral clusters enabling the solvent molecules to self-assemble into their neutral minimum energy configuration[24]. Then an ion is introduced into this cold nascent cluster. The energy introduced by the kinetic energy from the ion and the energy released

by solvation is dissipated through the efficient evaporation of argon. As first described for $Li^+(H_2O)_4Ar$[24], then subsequently seen in a number of other systems in our lab[25,26], if the barrier between a high energy $Cl^-(CH_3OH)_nAr$ configuration and the minimum energy $Cl^-(CH_3OH)_nAr$ configuration is greater than the binding energy of Ar to the cluster ion, the high energy conformer will be trapped. Considering $Cl^-(CH_3OH)_2Ar$, if the cluster ion is formed from the $(CH_3OH)_2$ hydrogen bonded dimer configuration, the minimum energy 2A isomer can only be formed by cleaving the hydrogen bond and then rearranging. The barrier to this process must be greater than the argon binding energy since a significant portion of our $Cl^-(CH_3OH)_2Ar$ clusters are the higher energy 2B isomer. Similar arguments can be made for our ability to isolate two high energy isomers in the n=3 case. The neutral methanol trimer has a cyclic hydrogen bonding structure[27]. Isomers 3A, 3B, and 3C require 3, 2, and 1 of those cyclic bonds to be broken, respectively, creating a barrier in going from the minimum energy neutral trimer configuration to the minimum energy 3A $Cl^-(CH_3OH)_3Ar$ configuration.

3.4 Conclusions

By studying the IRPD spectra of $Cl^-(CH_3OH)_{1-3}Ar$ cluster ions, we were able to observe very strong enhanced ionic hydrogen bonds. Due to the relatively small size of the chloride ion and cooperative effects, an EIHB stretch was measured at 2733 cm^{-1} for $Cl^-(CH_3OH)_3Ar$, shifted nearly 950 cm^{-1} from the neutral methanol OH vibrational frequency. Harmonic frequency calculations proved inadequate in estimating the magnitude of the frequency shifts in these systems. We therefore implemented a straightforward, computationally inexpensive procedure that approximates the IHB OH frequencies much more closely. This procedure was successfully applied to the IBH in

$Cl^-(CH_3OH)_1$ and the EIHB in conformer 2B of $Cl^-(CH_3OH)_2$, and gave notably good agreement with experiment.

The interesting observations of enhanced ionic bonds were made possible by our ability to efficiently trap high energy conformers by means of argon tagging. Introducing an ion into a pre-formed, neutral $(solvent)_nAr_m$ cluster tends to promote the production of trapped high energy conformers due to barriers between the neutral solvent configuration and the minimum cluster ion configuration.

Now that we have had success in generating and studying $Cl^-(CH_3OH)_nAr$ clusters, it would be worthwhile to investigate their $F^-(CH_3OH)_nAr$ analogs. In the case of fluoride, we anticipate that the enhanced ionic bonds will be even stronger, creating even larger shifts in the experimental spectra. This would provide another system to test our method of calculating vibrational transitions for IHB and EIHB OH stretches. It will be very interesting to determine if high energy isomers can be trapped for the smallest halide anion.

3.5 Figures

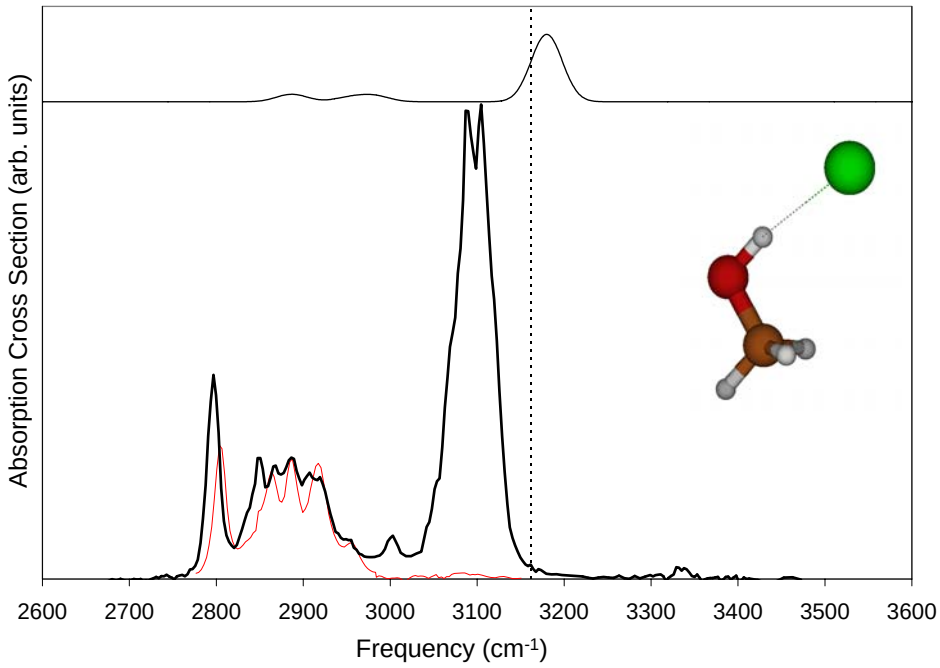

Figure 3.1. IRPD spectra of $Cl^-(CH_3OH)_1Ar$ (thick, black trace) and $Cl^-(CH_3OD)_1Ar$ (thin, red trace, scaled to the peak at 2890 cm^{-1}). Also shown is the calculated global minimum energy structure along with its simulated spectrum based on harmonic frequency calculations. The vertical dotted line represents the frequency of the OH stretch observed in $Cl^-(CH_3OH)_1$[7].

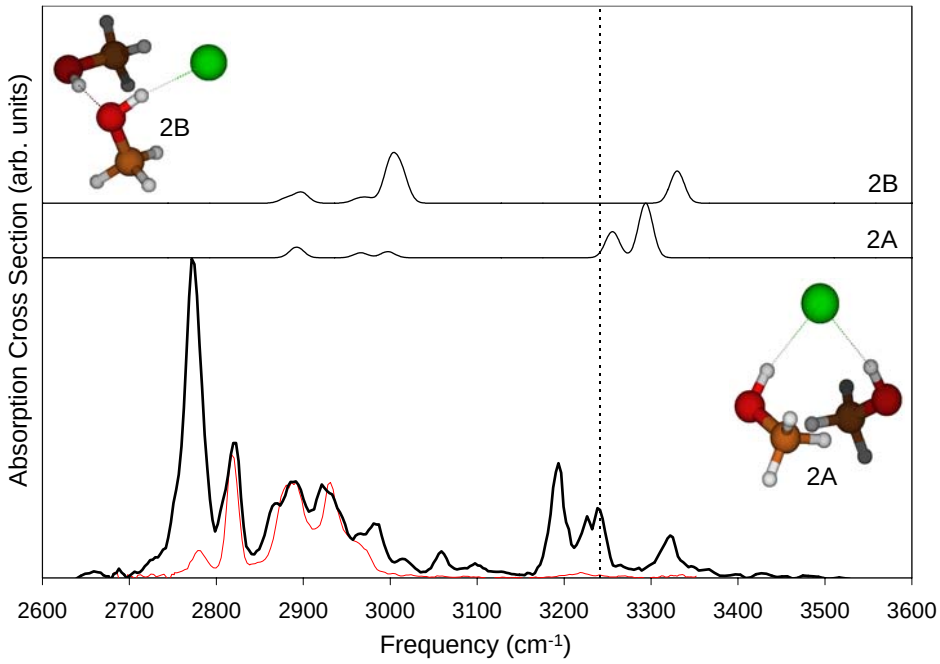

Figure 3.2. IRPD spectra of $Cl^-(CH_3OH)_2Ar$ (thick, black trace) and $Cl^-(CH_3OD)_2Ar$ (thin, red trace, scaled to the peak at 2890 cm^{-1}). Also shown are two calculated optimized structures and their corresponding simulated spectra based on harmonic frequency calculations. The vertical dotted line represents the frequency of the OH stretch observed in $Cl^-(CH_3OH)_2$[7].

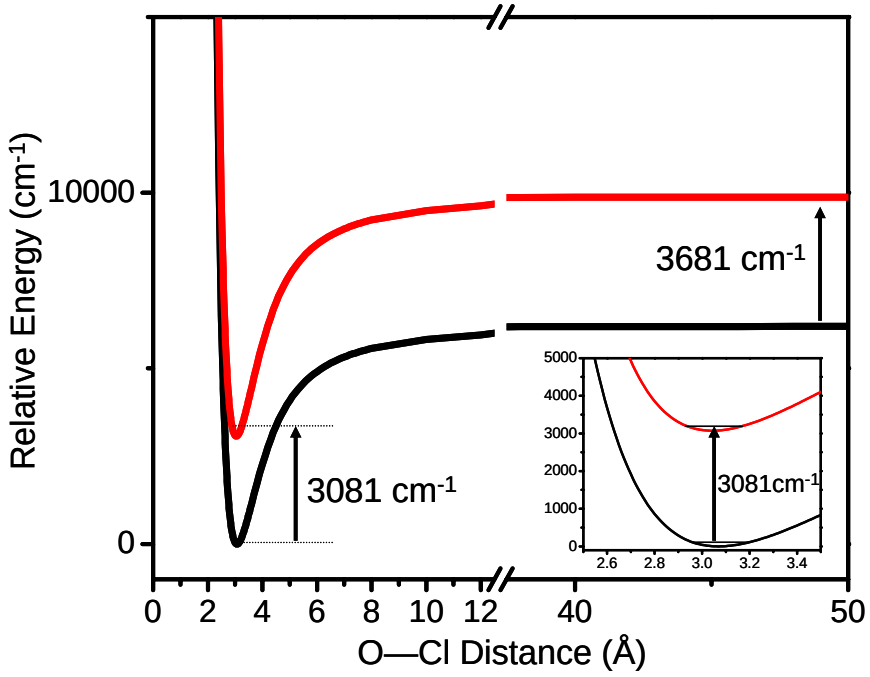

Figure 3.3. Calculated 1-D potentials for the O—Cl stretch of $Cl^-(CH_3OH)_1$ at two values of the OH distance: r_{OH} = 1.017 Å, corresponding to the average r_{OH} for ground state of the OH stretching mode (black trace), and r_{OH} = 1.067 Å, corresponding to the average r_{OH} for the first excited state of the OH stretching mode (red trace). For ease of interpretation, the red curve has been shifted so that the asymptotic $v_{OH} = 0 \rightarrow v_{OH} = 1$ value approaches the gas phase value of 3681 cm^{-1}. The inset shows an expanded view of the bottom of the potential wells where the ground state energy levels for the OCl stretching mode are shown.

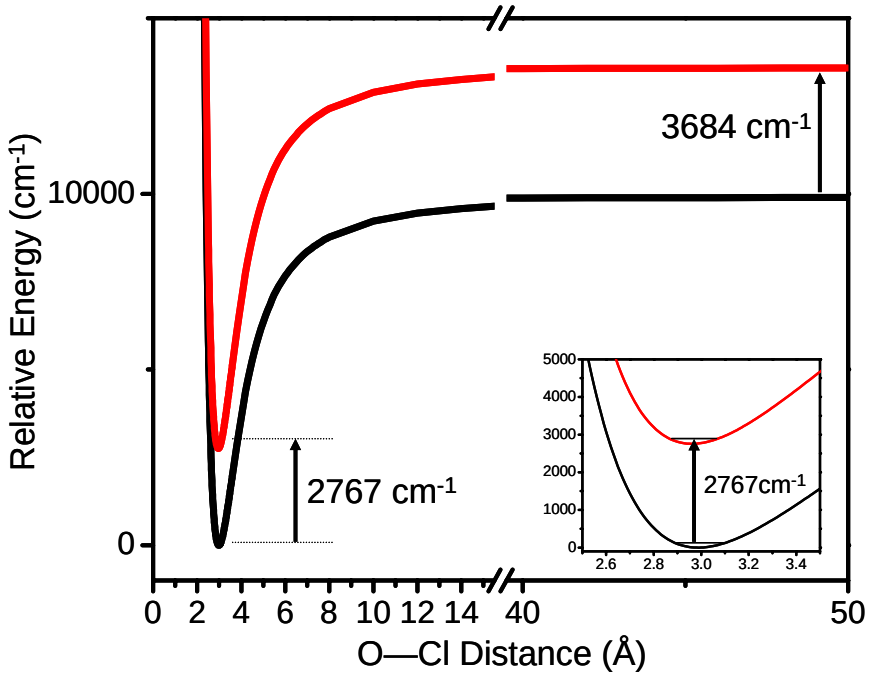

Figure 3.4. Calculated 1-D potentials for the O—Cl stretch of $Cl^-(CH_3OH)_2$ isomer 2B at two values of the EIHB OH distance: r_{OH} = 1.029 Å, corresponding to the average r_{OH} for the ground state of the OH stretching mode (black trace), and r_{OH} = 1.089 Å, corresponding to the average r_{OH} for the first excited state of the OH stretching mode (red trace). For ease of interpretation, the red curve has been shifted so that the asymptotic $v_{OH} = 0 \rightarrow v_{OH} = 1$ value approaches the gas phase value of 3684 cm^{-1} of the terminal OH in methanol dimer. The inset shows an expanded view of the bottom of the potential wells where the ground state energy levels for the OCl stretching mode are shown.

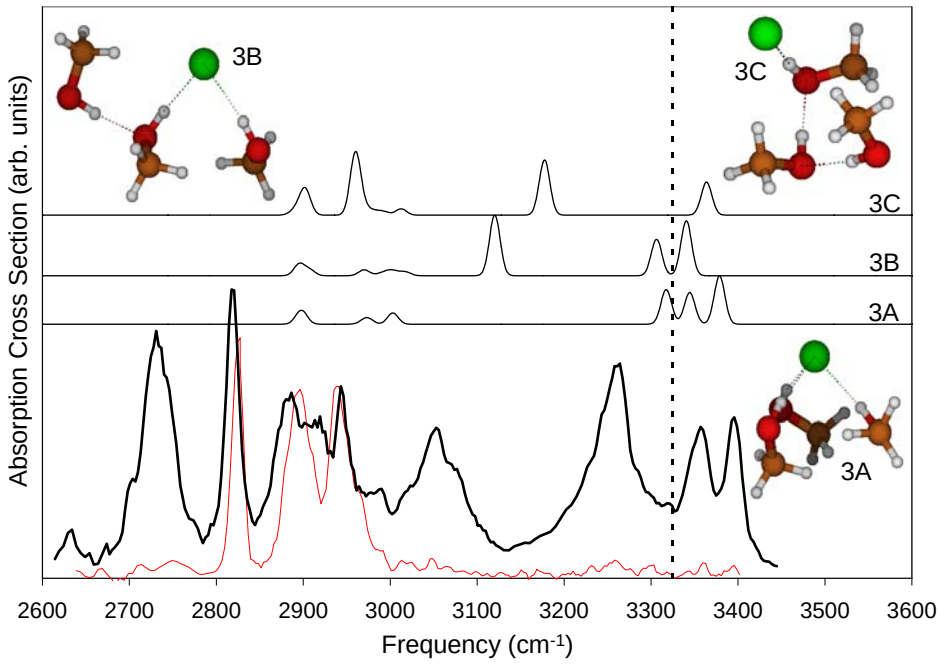

Figure 3.5. IRPD spectra of $Cl^-(CH_3OH)_3Ar$ (thick, black trace) and $Cl^-(CH_3OD)_3Ar$ (thin, red trace, scaled to the peak at 2940 cm^{-1}). Also shown are the three calculated optimized structures and their corresponding simulated spectra based on harmonic frequency calculations. The vertical dotted line represents the frequency of the OH stretch observed in $Cl^-(CH_3OH)_3$[7].

3.6 Tables

Table 3.1. Experimental red-shifts in the frequency of the OH stretch of methanol for $Cl^-(CH_3OH)_2Ar$[a] and $I^-(CH_3OH)_2Ar_3$[b]. All units are cm^{-1}.

	$Cl^-(CH_3OH)_2Ar$	$I^-(CH_3OH)_2Ar_3$
Frequency of enhanced H-bond stretch	2773	3134
Shift due to ion-MeOH ionic H-bond	-519	-331
Shift due to presence of Ar atom(s)	-65	-40
Shift due to cooperativity effects	-324	-176
Total shift from neutral, gas-phase MeOH	-908	-547

a) Ref [7]
b) Refs [11,12]

3.7 References

(1) Ayotte, P.; Bailey, C. G.; Weddle, G. H.; Johnson, M. A. *Journal of Physical Chemistry A* 1998, *102*, 3067.

(2) Ayotte, P.; Nielsen, S. B.; Weddle, G. H.; Johnson, M. A.; Xantheas, S. S. *Journal of Physical Chemistry A* 1999, *103*, 10668.

(3) Ayotte, P.; Weddle, G. H.; Johnson, M. A. *Journal of Chemical Physics* 1999, *110*, 7129.

(4) Ayotte, P.; Weddle, G. H.; Kim, J.; Johnson, M. A. *Chemical Physics* 1998, *239*, 485.

(5) Ayotte, P.; Weddle, G. H.; Kim, J.; Johnson, M. A. *Journal of the American Chemical Society* 1998, *120*, 12361.

(6) Cabarcos, O. M.; Weinheimer, C. J.; Lisy, J. M.; Xantheas, S. S. *The Journal of Chemical Physics* 1999, *110*, 5.

(7) Cabarcos, O. M.; Weinheimer, C. J.; Martinez, T. J.; Lisy, J. M. *The Journal of Chemical Physics* 1999, *110*, 9516.

(8) Choi, J.-H.; Kuwata, K. T.; Cao, Y.-B.; Okumura, M. *Journal of Physical Chemistry A* 1998, *102*, 503.

(9) Corbett, C. A.; Martinez, T. J.; Lisy, J. M. *The Journal of Physical Chemistry A* 2002, *106*, 10015.

(10) Johnson, M. S.; Kuwata, K. T.; Wong, C. K.; Okumura, M. *Chemical Physics Letters* 1996, *260*, 551.

(11) Nielsen, S. B.; Ayotte, P.; Kelley, J. A.; Johnson, M. A. *Journal of Chemical Physics* 1999, *111*, 9593.

(12) Robertson, W. H.; Karapetian, K.; Ayotte, P.; Jordan, K. D.; Johnson, M. A. *The Journal of Chemical Physics* 2002, *116*, 4853.

(13) Robertson, W. H.; Diken, E. G.; Price, E. A.; Shin, J.-W.; Johnson, M. A. *Science* 2003, *299*, 1367.

(14) Serrallach, A.; Meyer, R.; Gunthard, H. H. *Journal of Molecular Spectroscopy* 1974, *52*, 94.

(15) Frisch, M. J. T., G. W.; Schlegel, H. B.; Scuseria, G. E.; Robb, M. A.; Cheeseman, J. R.; Montgomery, Jr., J. A.; Vreven, T.; Kudin, K. N.; Burant, J. C.; Millam, J. M.; Iyengar, S. S.; Tomasi, J.; Barone, V.; Mennucci, B.; Cossi, M.; Scalmani, G.; Rega, N.; Petersson, G. A.; Nakatsuji, H.; Hada, M.; Ehara, M.; Toyota, K.; Fukuda, R.; Hasegawa, J.; Ishida, M.; Nakajima, T.; Honda, Y.; Kitao, O.; Nakai, H.; Klene, M.; Li, X.; Knox, J. E.; Hratchian, H. P.; Cross, J. B.; Bakken, V.; Adamo, C.; Jaramillo, J.; Gomperts, R.; Stratmann, R. E.; Yazyev, O.; Austin, A. J.; Cammi, R.; Pomelli, C.; Ochterski, J. W.; Ayala, P. Y.; Morokuma, K.; Voth, G. A.; Salvador, P.; Dannenberg, J. J.; Zakrzewski, V. G.; Dapprich, S.; Daniels, A. D.; Strain, M. C.; Farkas, O.; Malick, D. K.; Rabuck, A. D.; Raghavachari, K.; Foresman, J. B.; Ortiz, J. V.; Cui, Q.; Baboul, A. G.; Clifford, S.; Cioslowski, J.; Stefanov, B. B.; Liu, G.; Liashenko, A.; Piskorz, P.; Komaromi, I.; Martin, R. L.; Fox, D. J.; Keith, T.; Al-Laham, M. A.; Peng, C. Y.; Nanayakkara, A.; Challacombe, M.; Gill, P. M. W.; Johnson, B.; Chen, W.; Wong, M. W.; Gonzalez, C.; and Pople, J. A. Gaussian 03, Revision D.01; Gaussian, Inc.: Wallingford CT, 2004.

(16) Ayotte, P.; Bailey, C. G.; Kim, J.; Johnson, M. A. *Journal of Chemical Physics* 1998, *108*, 444.
(17) Huisken, F.; Kaloudis, M.; Kulcke, A. *The Journal of Chemical Physics* 1996, *104*, 17.
(18) Huisken, F.; Kaloudis, M.; Vigasin, A. A. *Chemical Physics Letters* 1997, *269*, 235.
(19) Huisken, F.; Stemmler, M. *The Journal of Chemical Physics* 1993, *98*, 7680.
(20) Buck, U.; Huisken, F. *Chemical Reviews* 2000, *100*, 3863.
(21) Huisken, F.; Kulcke, A.; Laush, C.; Lisy, J. M. *The Journal of Chemical Physics* 1991, *95*, 3924.
(22) Le Roy, R. J. LEVEL 8.0: A Computer Program for Solving the Radial Schrodinger Equation for Bound and Quasibound Levels University of Waterloo Chemical Physics Research Report CP-663, 2007.
(23) Robertson, W. H.; Kelley, J. A.; Johnson, M. A. *Review of Scientific Instruments* 2000, *71*, 4431.
(24) Miller, D. J.; Lisy, J. M. *Journal of the American Chemical Society* 2008, *130*, 15381.
(25) Nicely, A. L.; Miller, D. J.; Lisy, J. M. *Journal of the American Chemical Society* 2009, *131*, 6314.
(26) Rodriguez, J. D.; Lisy, J. M. *International Journal of Mass Spectrometry* 2009, *283*, 135.
(27) Huisken, F.; Kaloudis, M.; Koch, M.; Werhahn, O. *Journal of Chemical Physics* 1996, *105*, 8965.

Chapter 4: Chloride•••Amide Ionic Hydrogen Bonds in Cl^-(*N*-methylacetamide)$_1(H_2O)_{0-2}Ar_2$ Cluster Ions

4.1 Introduction

When two amino acids combine in a condensation reaction, an amide functional group is formed[1]. Due to their prevalence in biological systems, understanding amide groups and their interactions with their surroundings is very important. A currently unresolved question is how common salts interact with the protein backbone in aqueous environments and how these interactions impact the denaturing ability of various ions as seen in the Hofmeister series[2,3]. Our approach in addressing this question is to study small clusters containing an ion, an amide containing molecule, and an incrementally increasing number of water molecules using gas-phase infrared predissociation spectroscopy (IRPD)[4]. In this way, the importance of various non-covalent interactions such as ion•••amide, ion•••water, water•••amide, and water•••water can be determined.

N-methylacetamide (NMA) is one of the smallest and most tractable molecules containing the amide functional group and is often used to model the peptide backbone. Therefore, NMA has been studied extensively both experimentally[4-23] and computationally[11,24-31]. Recently, our group reported spectra of $M^+(NMA)_1(H_2O)_{0-3}$ for M = Na and K[4]. These results demonstrated that with two or fewer water molecules in this model system, the NMA adopted the *trans*-configuration with the cation bound to the carbonyl oxygen through an electrostatic interaction[4]. Subsequently, Heyda, et. al. performed MD simulations of 1M NMA in 1M solutions of NaCl, KCl, NaBr, and KBr[31]. Their results showed that both cations had an affinity for the carbonyl oxygen, consistent with the experimental observations[4]. Intriguingly, these same calculations indicated that

the anions had no affinity for the amine hydrogen, but rather had an affinity for the methyl groups. This was surprising in light of experimental studies where the anions have been shown to interact with the amide N-H site in crystal structures[5,6,8], NMA-benezene-salt solutions[15], and NMA in concentrated aqueous salt solutions[17]. In addition, Yu, et. al. have reported *ab initio* calculations where the Cl^-(NMA) complex has a N-H•••Cl^- structure[12]. Given these apparently conflicting results, we have elected to investigate $Cl^-(NMA)_1(H_2O)_n$ cluster ions.

4.2 Experimental and Computational Details

The experimental apparatus has been described in detail in chapter 2. The NMA was purchased from Sigma Aldrich and introduced to the system using the heated sample holder (~40^{o}C). In this chapter all spectra were recorded in the mass channel corresponding to the loss of two argons. No signal was observed in any other mass channels. Fluence-corrected photodissociation cross-sections are reported as a function of IR frequency.

Ab initio calculations were performed at the MP2/6-31+G* level of theory. Reported relative energies include zero point energy corrections. The calculated OH and NH stretching frequencies are scaled by 0.970 and 0.939, respectively, to match neutral values.

4.3 Results and Discussion

The large $Cl^-(NMA)_1$ binding energy (~70-100 kJ/mol)[12] precludes the direct acquisition of a $Cl^-(NMA)_1$ spectrum using IRPD spectroscopy. Thus, the argon tagging method was necessary in order to probe this small cluster. For consistency, argon tagging was used for the hydrated clusters as well, thus spectra of $Cl^-(NMA)_1(H_2O)_{0-2}Ar_2$ are

presented below. We also recorded a spectrum of $Cl^-(NMA)_1Ar_1$. The spectra of $Cl^-(NMA)_1Ar_1$ and $Cl^-(NMA)_1Ar_2$ are essentially identical, indicating that the argon atoms are not affecting the spectral frequencies and therefore only the $Cl^-(NMA)_1Ar_2$ spectrum is reported.

Before continuing, it is helpful to understand the structure of neutral NMA. Neutral NMA has two observed conformers, the *trans*- and *cis*-conformers, with the *trans*-conformer more stable and therefore the major conformer. The free-NH stretching frequencies of these two conformers are 3471 cm^{-1} (*trans*-NMA) and 3433 cm^{-1} (*cis*-NMA)[7,9]. The spectrum of $Cl^-(NMA)_1Ar_2$ is shown at the bottom of Figure 4.1. This spectrum has no features above 3200 cm^{-1}, indicating an N-H•••Cl^- ionic hydrogen bond. Such ionic hydrogen bonds are known to produce large red shifts in stretching frequencies as is seen here[32-37]. In order to determine the structure of the $Cl^-(NMA)_1$ complex that gives rise to the spectra in Figure 4.1, we performed *ab initio* geometry optimization and harmonic frequency calculations. The lowest energy Cl^-(*trans*-NMA) and Cl^-(*cis*-NMA) structures along with their simulated spectra are shown in Figure 4.2. According to the calculations, the Cl^-(*trans*-NMA) conformer is the minimum energy structure with the Cl^-(*cis*-NMA) conformer 38 kJ/mol higher in energy. Also, the harmonic frequency calculations predict that the Cl^-(*cis*-NMA) conformer will have an NH stretching frequency ~165 cm^{-1} *higher* in frequency than the Cl^-(*trans*-NMA) conformer. This reflects the more direct (linear) N-H•••Cl^- interaction in the latter compared to the former. The experimental spectrum shows one very sharp and prominent peak at 2835 cm^{-1} which is assigned to the NH stretch of the minimum energy Cl^-(*trans*-NMA) conformer. Since there are no major peaks ~165 cm^{-1} higher in

frequency than the 2835 cm^{-1} peak, we believe that the Cl^-(*cis*-NMA) conformer is either not present or only a minor component in the experiment.

The spectrum of $Cl^-(NMA)_1(H_2O)_1Ar_2$ is shown in the middle of Figure 4.1 with calculated structures and spectra of two low lying conformers shown in Figure 4.2. The most notable feature of this spectrum is the prominent peak centered at 2740 cm^{-1}, 95 cm^{-1} lower in frequency than the prominent peak from $Cl^-(NMA)_1Ar_2$. This observation can be explained by the cooperative effect of having the water bound to the carbonyl oxygen, as shown in the calculated global minimum energy structure for $Cl^-(NMA)_1(H_2O)_1$, isomer A in Figure 4.2. The presence of the water induces a further polarization of the C=O bond, which causes a shift of charge density away from the nitrogen and toward the carbonyl, strengthening the N-H•••Cl^- ionic hydrogen bond and shifting the N-H stretch to a lower frequency. The harmonic frequency calculations predict a red shift of ~80 cm^{-1} in the NH stretching frequency from $Cl^-(NMA)_1$ to $Cl^-(NMA)_1(H_2O)_1$, similar to the experimental shift of 95 cm^{-1}. Therefore, we assign the main peak in the $Cl^-(NMA)_1(H_2O)_1Ar_2$ spectrum to the NH stretch of isomer A shown in Figure 4.2. This structure also has two OH stretches, a hydrogen bonded OH and a free-OH, from the water molecule which would account for the two peaks at 3320 cm^{-1} and 3716 cm^{-1}, respectively.

The assignment of the feature at 3226 cm^{-1} is slightly more ambiguous. Since $Cl^-(NMA)_1(H_2O)_1$ isomer B has a calculated NH stretching mode in this frequency region, it was important to distinguish between experimental OH and NH stretching features. To accomplish this, we acquired a spectrum of $Cl^-(NMA)_1(D_2O)_1Ar_2$ as shown in Figure 4.3. Since the OD stretching vibrations are lower in frequency than our spectral

region, the $Cl^-(NMA)_1(D_2O)_1Ar_2$ contains only NH and CH stretching features. The two features between 3200-3350 in the $Cl^-(NMA)_1(H_2O)_1Ar_2$ spectrum are absent in the $Cl^-(NMA)_1(D_2O)_1Ar_2$ spectrum. This indicates that water OH stretching modes are responsible for these features and eliminates any possibility of a conformer, such as isomer B shown in Figure 4.2, with a weaker NH hydrogen bond giving rise to a feature in this region. We therefore conclude that the feature at 3226 cm^{-1} in the spectrum of $Cl^-(NMA)_1(H_2O)_1Ar_2$ is likely due to an overtone of the water bending mode, which is known to fall in the 3200-3300 cm^{-1} frequency range[37].

The spectrum of $Cl^-(NMA)_1(H_2O)_2Ar_2$ is shown at the top of Figure 4.1. The most prominent peak has shifted to even lower frequency, appearing at 2633 cm^{-1}. This red shift indicates that the N-H•••Cl^- bond increases in strength from $Cl^-(NMA)_1(H_2O)_1Ar_2$ to $Cl^-(NMA)_1(H_2O)_2Ar_2$, consistent with the addition of the second water to the carbonyl side of the structure. Unfortunately, the addition of the second water increases the complexity and time requirements of the calculations considerably, not allowing a full MP2 investigation to be performed.

4.4 Conclusions

IRPD spectra of $Cl^-(NMA)_1(H_2O)_{0\text{-}2}Ar_2$ show that the chloride ion is bound to the amine hydrogen, forming a strong ionic hydrogen bond. The presence of the waters strengthens the ionic hydrogen bond through cooperative effects induced by binding with the carbonyl oxygen. These results are not in agreement with the calculations of Heyda, et. al. for NMA in aqueous salt solutions, but appear more in line with previous experiments showing anion•••amine interactions. The discrepancy with the work of Heyda, et. al. could be due to the limited number of water molecules included in our

experiment. Alternatively, our results could indicate a limitation of the force fields used in their MD simulations. In either case, further investigation of this simple model of a peptide backbone is warranted.

4.5 Figures

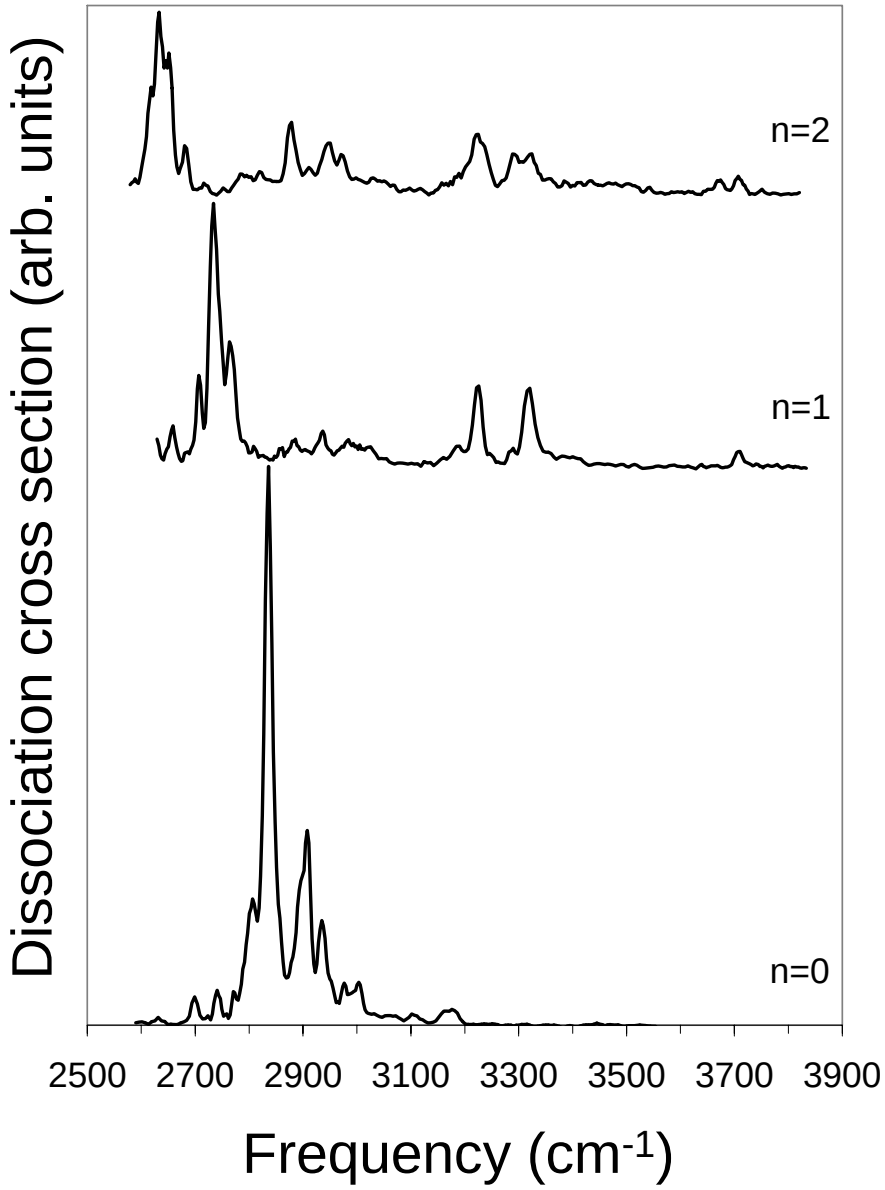

Figure 4.1. IRPD spectra of $Cl^-(NMA)_1(H_2O)_nAr_2$ with n = 0-2.

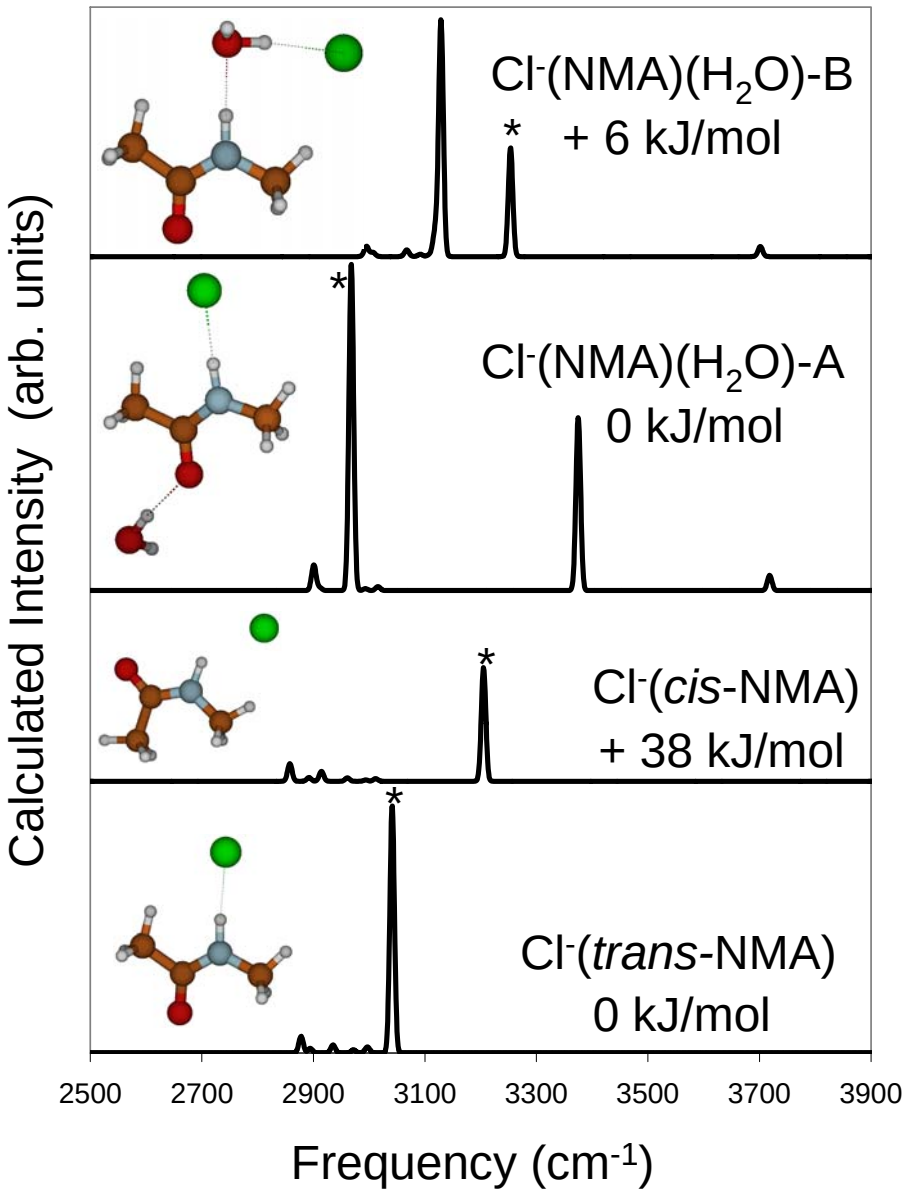

Figure 4.2. Calculated structures, simulated spectra, and relative energies for Cl^-(*trans*-NMA), Cl^-(*cis*-NMA), and two conformers of $Cl^-(NMA)_1(H_2O)_1$. In each of the spectra, the feature associated with the NH stretch is marked with an asterisk (*). Calculations were performed at the MP2/6-31+G* level. Zero point energy corrections are included.

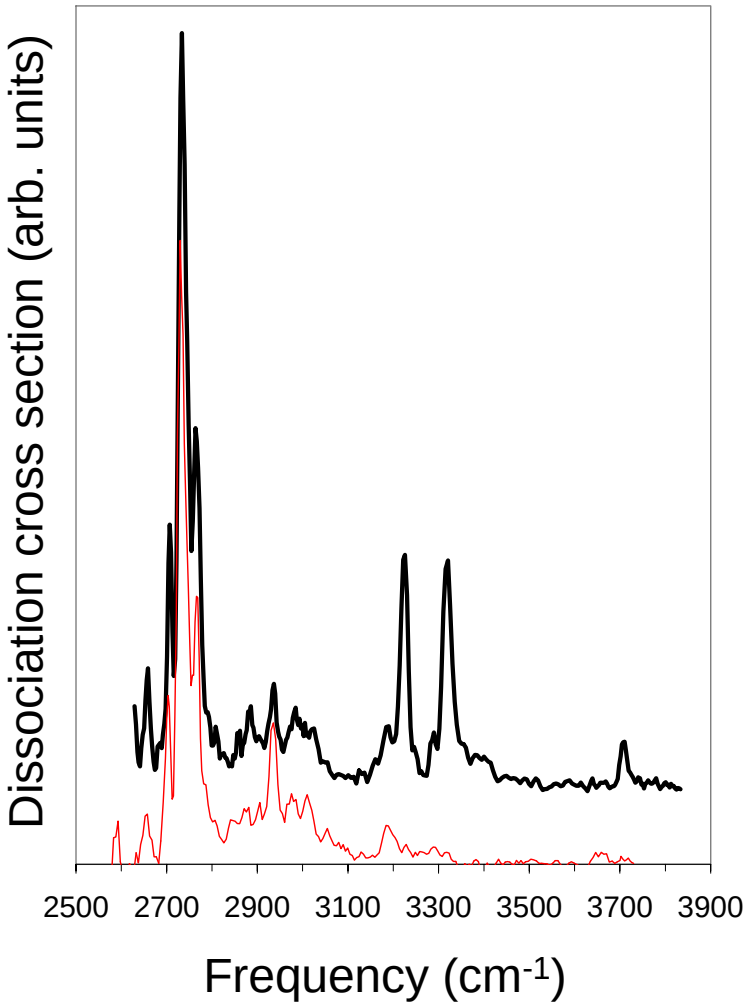

Figure 4.3. IRPD spectra of $Cl^-(NMA)_1(H_2O)_1Ar_2$, thick black trace, and $Cl^-(NMA)_1(D_2O)_1Ar_2$, thin red trace. Features present in the $Cl^-(NMA)_1(H_2O)_1Ar_2$ spectrum but absent from the $Cl^-(NMA)_1(D_2O)_1Ar_2$ spectrum are due to water. Features present in both spectra are due to NMA.

4.6 References

(1) Nelson, D. L.; Cox, N. M. *Lehninger Principles of Biochemistry*, 3rd ed.; Worth Publishers: New York, NY, 2000.
(2) Sedlak, E.; Stagg, L.; Wittung-Stafshede, P. *Archives of Biochemistry and Biophysics* 2008, *479*, 69.
(3) Zhang, Y.; Cremer, P. S. *Current Opinion in Chemical Biology* 2006, *10*, 658.
(4) Miller, D. J.; Lisy, J. M. *The Journal of Physical Chemistry A* 2007, *111*, 12409.
(5) Balasubramanian, D.; Shaikh, R. *Biopolymers* 1973, *12*, 1639.
(6) Bello, J.; Haas, D.; Bello, H. R. *Biochemistry* 1966, *5*, 2539.
(7) Czarnecki, M. A.; Haufa, K. Z. *Journal of Physical Chemistry A* 2005, *109*, 1015.
(8) Haas, D. J. *Nature* 1964, *201*, 64.
(9) Koddermann, T.; Ludwig, R. *Physical Chemistry Chemical Physics* 2004, *6*, 1867.
(10) Tsang, Y.; Siu, F. M.; Ho, C. S.; Ma, N. L.; Tsang, C. W. *Rapid Communications in Mass Spectrometry* 2004, *18*, 345.
(11) Whitfield, T. W.; Crain, J.; Martyna, G. J. *Journal of Chemical Physics* 2006, *124*.
(12) Yu, H.; Mazzanti, C. L.; Whitfield, T. W.; Koeppe, R. E.; Andersen, O. S.; Roux, B. *Journal of the American Chemical Society* 2010, *132*, 10847.
(13) Zhang, R.; Li, H.; Lei, Y.; Han, S. *Journal of Molecular Structure* 2004, *693*, 17.
(14) Ataka, S.; Takeuchi, H.; Tasumi, M. *Journal of Molecular Structure* 1984, *113*, 147.
(15) Bufalini, J.; Stern, K. H. *Journal of the American Chemical Society* 1961, *83*, 4362.
(16) Herrebout, W. A.; Clou, K.; Desseyn, H. O. *Journal of Physical Chemistry A* 2001, *105*, 4865.
(17) Hinton, J. F.; Amis, E. S.; Mettetal, W. *Spectrochimica Acta Part A: Molecular Spectroscopy* 1969, *25*, 119.
(18) Klassen, J. S.; Anderson, S. G.; Blades, A. T.; Kebarle, P. *Journal of Physical Chemistry* 1996, *100*, 14218.
(19) Lumley Jones, R. *Journal of Molecular Spectroscopy* 1963, *11*, 411.
(20) Mayne, L. C.; Hudson, B. *Journal of Physical Chemistry* 1991, *95*, 2962.
(21) Radzicka, A.; Pedersen, L.; Wolfenden, R. *BiochemistryÂ®* 1988, *27*, 4538.
(22) Russell, R. A.; Thompson, H. W. *Spectrochimica Acta* 1956, *8*, 138.
(23) Schrier, E. E.; Schrier, E. B. *The Journal of physical chemistry* 1967, *71*, 1851.
(24) Allison, S. K.; Bates, S. P.; Crain, J.; Martyna, G. J. *Journal of Physical Chemistry B* 2006, *110*, 21319.
(25) Beglov, D.; Roux, B. *Journal of Chemical Physics* 1996, *104*, 8678.
(26) Harder, E.; Anisimov, V. M.; Whitfield, T.; MacKerell Jr, A. D.; Roux, B. *Journal of Physical Chemistry B* 2008, *112*, 3509.
(27) Li, Z.; Yu, H.; Zhuang, W.; Mukamel, S. *Chemical Physics Letters* 2008, *452*, 78.
(28) Roux, B.; BernÃ¨che, S. *Biophysical Journal* 2002, *82*, 1681.
(29) Roux, B.; Karplus, M. *Journal of Computational Chemistry* 1995, *16*, 690.
(30) Whitfield, T. W.; Martyna, G. J.; Allison, S.; Bates, S. P.; Crain, J. *Chemical Physics Letters* 2005, *414*, 210.

(31) Heyda, J.; Vincent, J. C.; Tobias, D. J.; Dzubiella, J.; Jungwirth, P. *The Journal of Physical Chemistry B* 2010, *114*, 1213.
(32) Ayotte, P.; Nielsen, S. B.; Weddle, G. H.; Johnson, M. A.; Xantheas, S. S. *Journal of Physical Chemistry A* 1999, *103*, 10668.
(33) Ayotte, P.; Weddle, G. H.; Johnson, M. A. *Journal of Chemical Physics* 1999, *110*, 7129.
(34) Ayotte, P.; Weddle, G. H.; Kim, J.; Johnson, M. A. *Journal of the American Chemical Society* 1998, *120*, 12361.
(35) Beck, J. P.; Lisy, J. M. *The Journal of Physical Chemistry A* 2010, *114*, 10011.
(36) Choi, J.-H.; Kuwata, K. T.; Cao, Y.-B.; Okumura, M. *Journal of Physical Chemistry A* 1998, *102*, 503.
(37) Robertson, W. H.; Weddle, G. H.; Kelley, J. A.; Johnson, M. A. *Journal of Physical Chemistry A* 2002, *106*, 1205.

Chapter 5: Infrared Predissociation Spectroscopy of $M^+(C_6H_6)_{1-4}(H_2O)_{1-2}Ar_{0-1}$ Cluster Ions, M = Li, Na[‡]

5.1 Introduction

Non-covalent interactions are extremely important in chemistry and biochemistry. Examples include the ordered structure of ice[1], determining the secondary and tertiary structures of proteins[2], long range interactions in gases[3], and dictating ion transport and selectivity in ion channels[4,5]. It is important to study and understand non-covalent interactions at the fundamental level, and gas phase clusters are an ideal medium in which to study such interactions. By adjusting the composition, temperature, or size of the clusters, it is possible to select and probe specific non-covalent interactions or combinations of interactions. Of particular interest are $M^+(C_6H_6)_{1-4}(H_2O)_{1-2}Ar_{0-1}$ cluster ions (M=Li and Na), which can simultaneously incorporate several different types of non-covalent interactions present in biological systems: cation-π, cation-dipole, π-hydrogen bonds, and water-water hydrogen bonds.

Cation-π interactions have been discussed in detail by Dougherty, et. al[5-8]. In one computational study, they explored the impact of ion size on the stability of benzene-ion complexes in an aqueous environment where cation-π and cation-dipole interactions directly compete[6]. In this aqueous environment, K^+ was shown to form a more stable $M^+(C_6H_6)_2$ complex than Li^+. Although the individual Li^+-benzene interaction was greater than the K^+-benzene interaction, the small size of the lithium ion led to a larger energetic cost to dehydrate lithium.

[‡] This chapter is reproduced in part from a publication by Jordan P. Beck and James M. Lisy. Journal of Physical Chemistry A. In Press. American Chemical Society.

Weak π-hydrogen bonds were observed experimentally by Zwier et. al in neutral $(H_2O)_n(C_6H_6)_1$ clusters[9-12]. However, when an ion is introduced into the system, cluster structures and the strength of various non-covalent interactions change considerably. An initial study of competition between various non-covalent interactions was performed for $M^+(C_6H_6)_m(H_2O)_n$, M = Na and K[13,14] in the OH stretching region. In the Na^+ containing clusters with up to four waters, ion-dipole interactions led to structures with all the water ligands bound directly to the ion. This was in sharp contrast to the K^+ containing clusters where there was evidence that ion-π interactions were favored over ion-dipole interactions in some cases, leading to structures with water-water hydrogen bonding. These experiments provided insight into ion size-selectivity based on competing non-covalent interactions.

In the present chapter, we characterize non-covalent interactions in a second set of ion-benzene-water clusters based on infrared predissociation (IRPD) spectra of $Li^+(C_6H_6)_{1-4}(H_2O)_{1-2}Ar_{0-1}$, $Na^+(C_6H_6)_{2,4}(H_2O)_1Ar$ and $Na^+(C_6H_6)_{2-3}(H_2O)_2Ar$, and supporting *ab initio* calculations. By comparing argonated and nonargonated species, the effects of varying the internal energy (or effective temperature) can be observed. Argon tagging also provides the opportunity to kinetically trap high energy conformers of the argon-bearing species[15-17]. By varying the ion, we can compare and contrast the magnitude of the electrostatic interactions induced by the lithium and sodium ions.

5.2 Experimental and Computational Details

IRPD spectra were acquired using the triple-quadrupole mass spectrometer and tunable IR laser described in chapter 2 of this dissertation. As mentioned there, photon absorption leads to cluster fragmentation. In some instances, multiple-ligand loss can

follow photon absorption. Therefore, multiple spectra of the same parent ion are obtained by mass-selecting different fragment ions, corresponding to the different photodissociation loss channels, in the third quadrupole.

To aid in interpreting the experimental spectra, DFT (B3LYP/6-31+G*) calculations were performed for $Li^+(C_6H_6)_{1-4}(H_2O)_{1-2}$ and $Na^+(C_6H_6)_{2-4}(H_2O)_{1-2}$. This relatively small basis set has been used successfully in previous studies to identify stable configurations for large systems where higher level calculations have been computationally prohibitive[16,18,19]. For each cluster, a graphical interface was used to generate several (up to 10) input geometries. The GAUSSIAN 03 software package[20] was used to perform geometry optimizations on each of the input structures, many of which converged to the same geometry. The GAUSSIAN 03 software package was then used to calculate harmonic vibrational frequencies on the unique structures to ensure that a true minimum was located. The calculated frequencies were scaled by a factor of 0.975 so as to match the calculated average frequency of the symmetric and asymmetric stretch of neutral water with the experimental, gas phase average value[21]. Simulated spectra were generated using the SWIZARD program[22] giving each peak a Gaussian line shape with a 10 cm^{-1} width (FWHM). Although the calculations did not explicitly include argon, the calculated spectra were found to be in good agreement with the experimental spectra (*vide infra*). This indicated that the argon atom did not significantly perturb the O-H vibrational frequencies based on the structures of the cluster ions which were determined from the computed minima found on the potential energy surface of the non-argonated clusters.

MP2/6-31+G* calculations were also performed to obtain more accurate relative isomer energies, ligand binding energies, and to include effects from dispersion. Due to computational time requirements, fully optimized MP2/6-31+G* calculations were only used for the lithium clusters with fewer than five ligands, and were also extended to $Li^+(C_6H_6)_1(H_2O)_1Ar$ and $Li^+(C_6H_6)_2(H_2O)_2Ar$ cluster ions to estimate the Ar binding energy. All reported relative energies (unless noted otherwise) and binding energies were based on the MP2/6-31+G* calculations, which include vibrational zero-point energy corrections.

Calculations were also performed to estimate the average internal energy and effective temperature of the $Li^+(C_6H_6)_m(H_2O)_nAr_{0-1}$ clusters in our experiments. Since the clusters in these experiments are stabilized via evaporative cooling, their internal energy was modeled with the Rice-Ramsperger-Kassel-Marcus[23] evaporative ensemble[24-26] (RRKM-EE) formalism. We have used such calculations to model the internal energy content and effective temperatures of a variety of argonated[27] and non-argonated systems[28,29]. In general, clusters that contain argon and are formed via the evaporation of weakly bound argon atoms, have significantly less internal energy and lower effective temperatures than their non-argon-tagged counterparts. The RRKM-EE calculations for the $Li^+(C_6H_6)_m(H_2O)_nAr_{0-1}$ clusters bear out this general finding. The results of these calculations are summarized in Table 5.1. The non-argonated clusters have very broad internal energy distributions with average energies of ~ 40-80 kJ/mol depending on the cluster size and composition, corresponding to average effective temperatures from ~ 240-600 K. The argonated clusters, due to the lower binding energy of argon, have significantly less internal energy (~ 4 kJ/mol) and much lower effective

temperatures (~ 50-70 K). The dramatically lower internal energies and binding energies of the argonated clusters compared to their non-argonated counterparts have two effects: the IRPD spectra of the argonated clusters have sharper, more well-defined features, and argon tagging provides a mechanism to kinetically trap high-energy isomers.

5.3 Results and Discussion

$Li^+(C_6H_6)_{1-4}(H_2O)_1Ar$

The effect of sequentially adding benzene to the monohydrated, $Li^+(C_6H_6)_n(H_2O)_1Ar$ clusters is demonstrated by the experimental IRPD spectra shown on the left side of Figure 5.1. The most notable aspect of these spectra is the monotonically increasing interaction between the water and benzenes as more benzene ligands are added, as evidenced by the red shifts of the OH stretching features. For n=1, there is no detectable benzene-water interaction, but in the n=2 spectrum, the low-frequency band has shifted 60 cm^{-1} to lower frequency. This indicates that one of the water OH groups in $Li^+(C_6H_6)_2(H_2O)_1Ar$ is weakly interacting with a benzene molecule. In the n=3 spectrum, both OH stretching features are shifted to lower frequency compared to n=1, which indicates that both water OH groups directly interact with a benzene. Based on the magnitude of the spectral shifts, one OH group is perturbed only weakly by the benzene, while the other shows evidence of a stronger interaction indicative of a π-hydrogen bond. The trend is completed in the spectrum of $Li^+(C_6H_6)_4(H_2O)_1Ar$ where both bands are significantly red shifted, indicating a structure where each OH group is interacting with a benzene via a π-hydrogen bond.

The calculated global minimum energy structures and their corresponding simulated spectra are displayed side-by-side with the IRPD spectra in Figure 5.1. The

simulated spectra are remarkably consistent with the experimental spectra and were used to make the spectral assignments summarized in Table 5.2. The trends discussed above can be readily understood in terms of the structures presented in Figure 5.1. The water-benzene interaction in the n=2 cluster comes from one water OH group in the first solvent shell slightly perturbed by a benzene which is also in the first solvent shell. The interaction is weak because the OH group cannot directly interact with the π cloud of the adjacent benzene, where the O-H-C (C represents the nearest carbon) angle is an unfavorable 141°. When a third benzene molecule is added to the system, it occupies a position in a second solvation shell. The interaction between the first shell water and the second shell benzene has a more favorable overlap with the π cloud and an improved O-H-C angle (162°), giving rise to the stronger π-hydrogen bond observed in the n=3 structure. For $Li^+(C_6H_6)_4(H_2O)_1Ar$, both water OH groups have favorable overlap with the π clouds of second shell benzene molecules (at angles near 166°), giving rise to symmetric and asymmetric π-hydrogen bonded OH stretches.

In addition to the spectra of the argonated clusters presented in Figure 5.1, we also obtained spectra of the non-argonated $Li^+(C_6H_6)_{2-4}(H_2O)_1$ clusters. With binding energies of 132 kJ/mol for benzene and 126 kJ/mol for water, photodissociation was not observed for $Li^+(C_6H_6)_1(H_2O)_1$. The spectra of these non-argonated $Li^+(C_6H_6)_{2-4}(H_2O)_1$ clusters were acquired in the benzene loss channel and are very similar to their argonated counterparts so are not presented here. However, there are two major differences between the argonated and non-argonated spectra. First, the spectra of the non-argonated clusters show broader and less-defined features. This is a result of the larger amount of internal energy (higher effective temperature) of non-argonated clusters compared to

argonated clusters (see Table 5.1). The second difference comes from the spectrum of $Li^+(C_6H_6)_2(H_2O)_1$, shown in Figure 5.2. In addition to the two features associated with isomer 2-1A, the spectrum of $Li^+(C_6H_6)_2(H_2O)_1$ contains a third band at 3480 cm^{-1}, which must come from a different conformer with a stronger hydrogen bond. A second minimum on the potential energy surface was identified and labeled 2-1B, and is likely the structure responsible for the additional band. As can be seen in Figure 5.2, the position of a benzene in the second solvent shell, in 2-1B, will give rise to a near-optimal π-hydrogen bonded OH stretch, which is shifted to lower frequency than the weaker interaction in 2-1A. The presence of this conformer is only possible due to the large internal energy content of the non-argonated $Li^+(C_6H_6)_2(H_2O)_1$ cluster. As shown in Table 5.1, the $Li^+(C_6H_6)_2(H_2O)_1$ clusters have a very broad energy distribution centered around 48 kJ/mol. Since isomer 2-1B is only 18 kJ/mol higher in energy than isomer 2-1A, a small portion of the cluster ensemble can populate this configuration based on the internal energy. However, the weak intensity of the feature at 3480 cm^{-1} suggests that isomer 2-1B is a minor contributor to the overall $Li^+(C_6H_6)_2(H_2O)_1$ cluster distribution. The major isomer for both the argonated and non-argonated cases is the minimum energy isomer 2-1A.

$Li^+(C_6H_6)_{1\text{-}4}(H_2O)_2Ar_{0\text{-}1}$

The spectra of $Li^+(C_6H_6)_1(H_2O)_2Ar_{0\text{-}1}$, shown in Figure 5.3, serve as a baseline for dihydrated cluster ions with no hydrogen bonds. The spectra of the argonated and non-argonated spectra are similar, differing in the widths and heights of the spectral peaks. The observed bands correspond to symmetric and asymmetric OH stretching modes consistent with structure 1-2A, where all three ligands are in the first solvent shell.

The addition of a second benzene leads to a number of interesting effects and richer spectra as seen in Figure 5.4. Once again, the spectrum of the non-argonated $Li^+(C_6H_6)_2(H_2O)_2$ cluster obtained in the benzene loss channel (shown in red) is very similar to the spectrum of $Li^+(C_6H_6)_2(H_2O)_2Ar$ obtained in the argon loss channel (shown in black). These spectra are remarkably simple with only two bands in the OH stretching region. This indicates that the two water molecules in these clusters are in essentially identical environments, consistent with the calculated IR spectrum from the global minimum energy structure 2-2A, where one OH group from each water forms a π-hydrogen bond to the same second shell benzene molecule. This compact structure with one benzene molecule interacting with two water molecules was not observed in the analogous Na^+ and K^+ clusters[13,14] and appears to be a unique result owing to the smaller size of Li^+.

A radically different spectrum of $Li^+(C_6H_6)_2(H_2O)_2Ar$, also shown in Figure 5.4, is obtained when the ($Ar + C_6H_6$) loss channel (shown in blue) is monitored. In addition to the two bands identified with structure 2-2A, this spectrum has four new prominent bands, signaling the presence of another conformer. These new bands are narrow, indicating a low effective temperature, but can only come from a higher energy conformer with sufficient energy, when combined with the photon energy, to dissociate both ligands. Structure 2-2B, shown in Figure 5.4, is calculated to be 13 kJ/mol higher in energy than the minimum energy 2-2A isomer. It also has a calculated spectrum with four bands that make an excellent match with the new features in the ($Ar + C_6H_6$) loss channel spectrum. The most prominent band at 3390 cm^{-1} is due to an OH participating as a proton donor in a water-water hydrogen bond. This assignment is supported by noting

the similarity between conformers 3-1A (Figure 5.1) and 2-2B, where the second shell benzene in the former is replaced by a water in the latter. We also note that the OH stretch of the donating group in the water-water hydrogen bond at 3390 cm^{-1} is in the region of 3350-3490cm^{-1} where linear hydrogen bonded OH stretches were observed in IRPD spectra $Li^+(H_2O)_5Ar$[15].

The presence of the high energy 2-2B conformer is due to the formation mechanism of the argonated cluster ions. These clusters are formed when the ion collides with a neutral cluster containing a large number of argon atoms. The ion approaches a cold neutral cluster (in this case $(C_6H_6)_2(H_2O)_2$) imbedded in argon. Kinetic energy, released as the ion approaches the neutral molecular cluster, is rapidly dissipated by argon evaporation. If the barrier to rearrangement of this nascent cluster-ion configuration to a lower energy configuration is greater than the binding energy of argon, a high energy conformation of $Li^+(C_6H_6)_2(H_2O)_2Ar_1$ can be trapped. We have observed the results of this trapping mechanism in other systems such as $Li^+(H_2O)_nAr$ [15], K^+(18-crown-6 ether)$(H_2O)_1Ar_{1-4}$ [16] and $Cl^-(CH_3OH)_nAr$ [17].

Upon IR excitation of the conformer 2-2B, both an argon and a benzene are dissociated. The exact mechanism of dissociation is not known, but the energy provided by the photon should be sufficient to overcome any barriers to rearrangement. It then becomes a matter of considering the energy required to access the dissociation channel of the fragment (product) cluster ion. A summary of the energies calculated for the Li^+ containing clusters is given in Table 5.3. The benzene binding energy of isomer 2-2A is 50 kJ/mol. Since isomer 2-2B is 13 kJ/mol higher in energy than isomer 2-2A, the energy required to dissociate one benzene from isomer 2-2B to form isomer 1-2A is 37

kJ/mol. Adding the argon binding energy of 7 kJ/mol, a total of 44 kJ/mol is required to dissociate both argon and benzene from isomer 2-2B. This is within the range of the photon energy (40-45 kJ/mol) used in these experiments.

Based on the relatively small peaks at 3540 and 3710 cm^{-1}, conformer 2-2A also contributes to the loss of ($Ar + C_6H_6$) spectrum from $Li^+(C_6H_6)_2(H_2O)_2Ar$. By comparing the integrated photodissociation cross-sections, 90% of the $Li^+(C_6H_6)_2(H_2O)_2Ar_1$ 2-2A cluster ions dissociate via the argon loss channel, suggesting that only a small portion of the 2-2A clusters lose ($Ar + C_6H_6$). However, combining the photon energy of 42 to 44 kJ/mol (3540-3710 cm^{-1}) with the internal energy of less than 10 kJ/mol, the available energy of 52-54 kJ/mol appears to be insufficient for photodissociation of the 2-2A conformer by loss of ($Ar + C_6H_6$), which requires 57 kJ/mol (7 kJ/mol for argon plus 50 kJ/mol for benzene) based on the MP2 binding energies (Table 5.3). This suggests that the calculated binding energies (MP2/6-31+G* corrected for zero-point energy) may be somewhat inaccurate, which may reflect basis set limitations. If the calculated benzene binding energy of isomer 2-2A was just ~10-15% lower, then the calculated results would be in line with the experiment. Other photofragmentation loss channels: ($2\ C_6H_6 + Ar$) or ($H_2O + Ar$) requiring energies of 123 and 77 kJ/mol, respectively, were not observed, as they are well beyond the total available energy.

The structures of the $Li^+(C_6H_6)_2(H_2O)_2Ar_{0-1}$ clusters serve as a base unit on which larger clusters are built. For example, the spectra of $Li^+(C_6H_6)_3(H_2O)_2Ar_{0-1}$ are displayed in Figure 5.5. Once again, the spectrum of the non-argonated $Li^+(C_6H_6)_3(H_2O)_2$ cluster (red) and the Ar loss spectrum from $Li^+(C_6H_6)_3(H_2O)_2Ar_1$ (black) are similar and match well with the calculated spectrum of the global minimum energy isomer 3-2A. This

conformer preserves the structure of the 2-2A conformer with the third benzene bound to one of the free OH groups. The (Ar + C_6H_6) loss spectrum of $Li^+(C_6H_6)_3(H_2O)_2Ar_1$ (blue spectrum in Figure 5.5) contains four additional prominent peaks that match well with the calculated spectrum of conformer 3-2B. In this case, the 2-2B conformer is the base unit, with the third benzene bound to the free OH of the first shell water. The assignment of each experimentally observed feature is readily made by comparison with the calculated spectra of the two structures shown in Figure 5.5. The experimental and calculated frequencies of all of the features from the argonated spectra and their assignments are summarized in Table 5.4.

Similar results are obtained for $Li^+(C_6H_6)_4(H_2O)_2Ar_{0-1}$, displayed in Figure 5.6. The spectra (red) of the non-argonated cluster and the Ar loss spectrum (black) of the argonated cluster are similar to each other. The simplicity of the spectra, with the presence of only two bands, suggests a structure where both waters are in identical environments. This is consistent with isomer 4-2A, where the 2-2A conformer is the building unit with the free OH groups capped by benzene molecules. However, the spectrum of $Li^+(C_6H_6)_4(H_2O)_2Ar$ acquired in the (Ar + C_6H_6) loss channel has new and prominent features. These new features can be assigned based by comparison with the calculated vibrational spectrum of the high-energy 4-2B conformer, with the exception of the two lowest frequency peaks at 3266 and 3243 cm^{-1}. Similar bands have been previously observed[30,31] and identified as bend overtones of water that gain intensity via Fermi resonance from nearby hydrogen-bonded OH vibrations. In this case, the OH stretch associated with the water-water hydrogen bond at 3322 cm^{-1} provides intensity for the bend overtones from the first and second shell waters. These features are not present

in the calculations which are based on the double harmonic approximation of vibrations and transition moments. The origin of the structure of the 4-2B conformer is clearly seen by comparison to the 3-2B unit with the additional benzene bound to the second shell water.

To observe the spectral evolution of the trapped, high energy conformers, a compilation is presented in Figure 5.7 with the features from the high energy isomers highlighted in blue. In contrast to the monotonic effect of additional benzene molecules on the OH stretches in $Li^+(C_6H_6)_n(H_2O)_1Ar$ shown in Figure 5.1, the impact of additional benzene molecules on the water-water hydrogen bonded OH stretch in $Li^+(C_6H_6)_n(H_2O)_2Ar$ is not as straightforward. Relative to $Li^+(C_6H_6)_2(H_2O)_2Ar$, the water-water hydrogen bond OH stretch actually shifts higher in frequency in $Li^+(C_6H_6)_3(H_2O)_2Ar$. The third benzene binding to the first shell water causes a weakening of the water-water interaction, when compared to $Li^+(C_6H_6)_2(H_2O)_2Ar$. As the fourth benzene is added to the system, it binds to the second shell water enhancing the hydrogen-bonding network, which in turn strengthens the water-water interaction. Thus, for $Li^+(C_6H_6)_4(H_2O)_2Ar$, the water-water hydrogen bonded OH stretch appears at 3322 cm^{-1}, lower in frequency than the hydrogen-bonded OH stretch observed in $Li^+(C_6H_6)_2(H_2O)_2Ar$.

Comparison of Li^+ and Na^+ containing clusters

The effects of ion size are elucidated by comparing the $Li^+(C_6H_6)_{1-4}(H_2O)_{1-2}Ar$ spectra with the spectra of $Na^+(C_6H_6)_{1-4}(H_2O)_{1-2}Ar$. The two mono-hydrated clusters with the most striking spectral differences are $M^+(C_6H_6)_{2,4}(H_2O)_1Ar$ for Li^+ and Na^+. These spectra are shown in Figure 5.8. With $Li^+(C_6H_6)_2(H_2O)_1Ar$ (on the left panel of

Figure 5.8), a very weak interaction was noted between the water and one benzene in the first shell, resulting in a shift of one OH band to below 3600 cm^{-1}. For $Na^+(C_6H_6)_2(H_2O)_1Ar$, there is no detectable interaction between the benzene and water as reflected by the OH symmetric and asymmetric stretches of water at 3650 and 3730 cm^{-1}. The experimentally observed symmetric and asymmetric OH stretching frequencies for $Na^+(H_2O)_3Ar$, a cluster with no observed hydrogen bonding, were reported as 3650 cm^{-1} and 3718 cm^{-1}, respectively[15]. The good agreement between the spectra of $Na^+(H_2O)_3Ar$ and $Na^+(C_6H_6)_2(H_2O)_1Ar$ supports the structural assignment given for $Na^+(C_6H_6)_2(H_2O)_1Ar$. The larger size of the sodium cation has the effect of positioning the two benzene molecules and one water molecule further away from the ion, making any ligand-ligand interaction unfavorable.

In the four-benzene spectra (the right panel of Figure 5.8), $Li^+(C_6H_6)_4(H_2O)_1Ar$ clearly has a water with two π-hydrogen bonds, while the $Na^+(C_6H_6)_4(H_2O)_1Ar$ spectrum has two dominant peaks at 3564 and 3690 cm^{-1}. The lower frequency band strongly supports a structure with a normal π-hydrogen bond. The high frequency band at 3690 cm^{-1}, is very close to the free OH stretching frequency (typically in the 3706-13 cm^{-1} range). This suggests a situation similar to $Li^+(C_6H_6)_3(H_2O)_1Ar$ where the nominally free OH slightly interacts with a first shell benzene, while the other OH group forms a more conventional π-hydrogen bond. In $Li^+(C_6H_6)_3(H_2O)_1Ar$, the two bands occur at 3540 and 3655 cm^{-1}, slightly lower in frequency than for $Na^+(C_6H_6)_4(H_2O)_1Ar$, which exerts a weaker electrostatic enhancement of the hydrogen bond interactions. These conclusions are supported by the calculated global minimum energy structure of $Na^+(C_6H_6)_4(H_2O)_1$ shown in Figure 5.8. The calculated structure shows that there are four ligands in the first

solvent shell with one of the first shell benzenes interacting with both the Na^+ ion and the water molecule. (The non-argonated $Na^+(C_6H_6)_4(H_2O)_1$ spectrum has been reported previously[14] and showed a combination of isomers, some with only one π-hydrogen bond and some with two π-hydrogen bonds. By argonating the cluster, we have shown that the preferred configuration at lower effective temperature has one π-hydrogen bond and four ligands in the first shell.)

The most interesting comparison between Li^+ and Na^+ for the di-hydrated clusters are $M^+(C_6H_6)_{2\text{-}3}(H_2O)_2Ar$, as shown in Figure 5.9. The $Na^+(C_6H_6)_2(H_2O)_2Ar$ spectrum (left panel) clearly indicates the presence of a structure with a water-water hydrogen bond, similar to the 2-2B, lithium cluster. The $Li^+(C_6H_6)_2(H_2O)_2Ar$ (Ar + C_6H_6) loss spectrum (with the features from 2-2B highlighted in blue) is given just below to show the analogous vibrational features. In the non-argonated $Na^+(C_6H_6)_2(H_2O)_2$ spectrum reported previously[14], all four ligands were in the first shell with no observed hydrogen bonding. Thus $Na^+(C_6H_6)_2(H_2O)_2Ar$ is another example of high energy isomer trapping induced by argon tagging. Here, the trapped isomer is ~ 3.5 kJ/mol higher in energy (based on DFT calculations) than the structure with all four ligands in the first solvent shell. It is possible that the $Na^+(C_6H_6)_2(H_2O)_2Ar$ spectrum contains some contribution from a structure with all four ligands in the first shell, since the symmetric and asymmetric water stretches in such a structure would overlap with the symmetric and asymmetric stretches of the second shell water in the water-water hydrogen-bonded structure. It is clear, though, that in contrast to the $Li^+(C_6H_6)_2(H_2O)_2Ar$ global minimum structure 2-2A, there is no indication of a π-hydrogen bond in $Na^+(C_6H_6)_2(H_2O)_2Ar$.

The addition of a third benzene in the Na^+ system dramatically alters the hydrogen bonding. The $Na^+(C_6H_6)_3(H_2O)_2Ar$ spectrum shows no indication of water-water hydrogen bonding and bears no resemblance to either of the structures observed for $Li^+(C_6H_6)_3(H_2O)_2Ar$. Instead, with only two features, the $Na^+(C_6H_6)_3(H_2O)_2Ar$ spectrum suggests a structure with the waters in identical environments, consistent with the more open type structure depicted for $Na^+(C_6H_6)_3(H_2O)_2$ in Figure 5.9. One OH group of each water is capped by a different benzene.

It is also quite interesting to consider the difference between $Na^+(C_6H_6)_2(H_2O)_2$ and $Na^+(C_6H_6)_3(H_2O)_2$. For $Na^+(C_6H_6)_3(H_2O)_2$, both the argonated version (shown in Figure 5.9) and the non-argonated version[14] consist of two singly capped water molecules with a total of three ligands in the first shell. However, the non-argonated spectrum of $Na^+(C_6H_6)_2(H_2O)_2$ with no hydrogen bonds indicates a structure with all four ligands in the first shell. The addition of a third benzene thus favors a reordering of the solvent shell structure with three ligands (two waters and one benzene) in the first shell. This once again underscores the delicate balance between competing non-covalent interactions.

5.4 Conclusions

The competition between electrostatic interactions, water-water hydrogen bonds, and π-hydrogen bonds in $M^+(C_6H_6)_{1-4}(H_2O)_{1-2}Ar_{0-1}$, M = Li, Na was studied by IRPD spectroscopy and electronic structure calculations. Both the experimental spectra and the electronic structure calculations indicate a compact global minimum energy structure for $Li^+(C_6H_6)_2(H_2O)_2$ where one benzene in the second shell interacts with both water molecules. This type of structure was not observed with the larger Na^+ or K^+ and seems

to be a result of the small lithium ion size[13,14]. This structure appears to be robust and is preserved upon the addition of more benzene molecules, with the third and fourth benzene ligands attaching to the remaining available OH groups.

For the Li^+ cluster ions bearing an argon atom and formed by argon evaporation, high energy isomers were identified and detected exclusively by monitoring the (Ar + C_6H_6) loss channel. These conformers exhibited water-water hydrogen bonding for $Li^+(C_6H_6)_{2\text{-}4}(H_2O)_2Ar$. Considering the structure-breaking ability of the lithium cation, observation of water-water hydrogen bonding in a cluster as small as $Li^+(C_6H_6)_2(H_2O)_2Ar$ was initially surprising. However, the strong electrostatic interaction responsible for structure-breaking also appears to be responsible for generating multiple minima on the potential energy surface with sufficient depth to permit their trapping and detection. This competition between various non-covalent interactions opens up the exploration of the potential energy surface in charged species in a manner similar to that applied to neutral clusters and flexible biomolecules[32,33].

In contrast to the di-hydrated clusters, no high energy isomers were detected for the mono-hydrated $Li^+(C_6H_6)_{1\text{-}4}(H_2O)_1Ar$ clusters. Rather, a smooth progression from a structure with no significant benzene-water interaction in $Li^+(C_6H_6)_1(H_2O)_1Ar$ to a structure with two π-hydrogen bonds in $Li^+(C_6H_6)_4(H_2O)_1Ar$ was observed and assigned based on global minimum energy structures. In each case, the lithium cation can readily accommodate three ligands in its first solvent shell. However, due to its small ionic radius, it is possible for the water to interact with one of the first shell benzenes.

The impact of ion size on $M^+(C_6H_6)_{1\text{-}4}(H_2O)_{1\text{-}2}Ar_{0\text{-}1}$ was probed by comparing spectra from clusters containing Li^+ with those containing Na^+. The differences in the

mono-hydrated spectra can be explained simply by the difference in space available around the ion. Unlike Li^+, the larger Na^+ ion can accommodate two benzenes and one water in its first solvent shell with no detectable water-benzene interaction. Also, while Li^+ can only accommodate three ligands in its first solvent shell, the larger Na^+ is able to accommodate four ligands in its first solvent shell. This leads to a difference in the spectra of $M^+(C_6H_6)_4(H_2O)_1Ar$ where the cluster with Li^+ has two π-hydrogen bonds while the cluster with Na^+ has only one. Finally, structures with one benzene interacting with two water molecules, which were observed in the di-hydrated, Li^+-containing clusters, were not observed in the Na^+-containing clusters. This emphasizes the important role of the ion in determining the most favorable balance of competing non-covalent interactions.

5.5 Figures

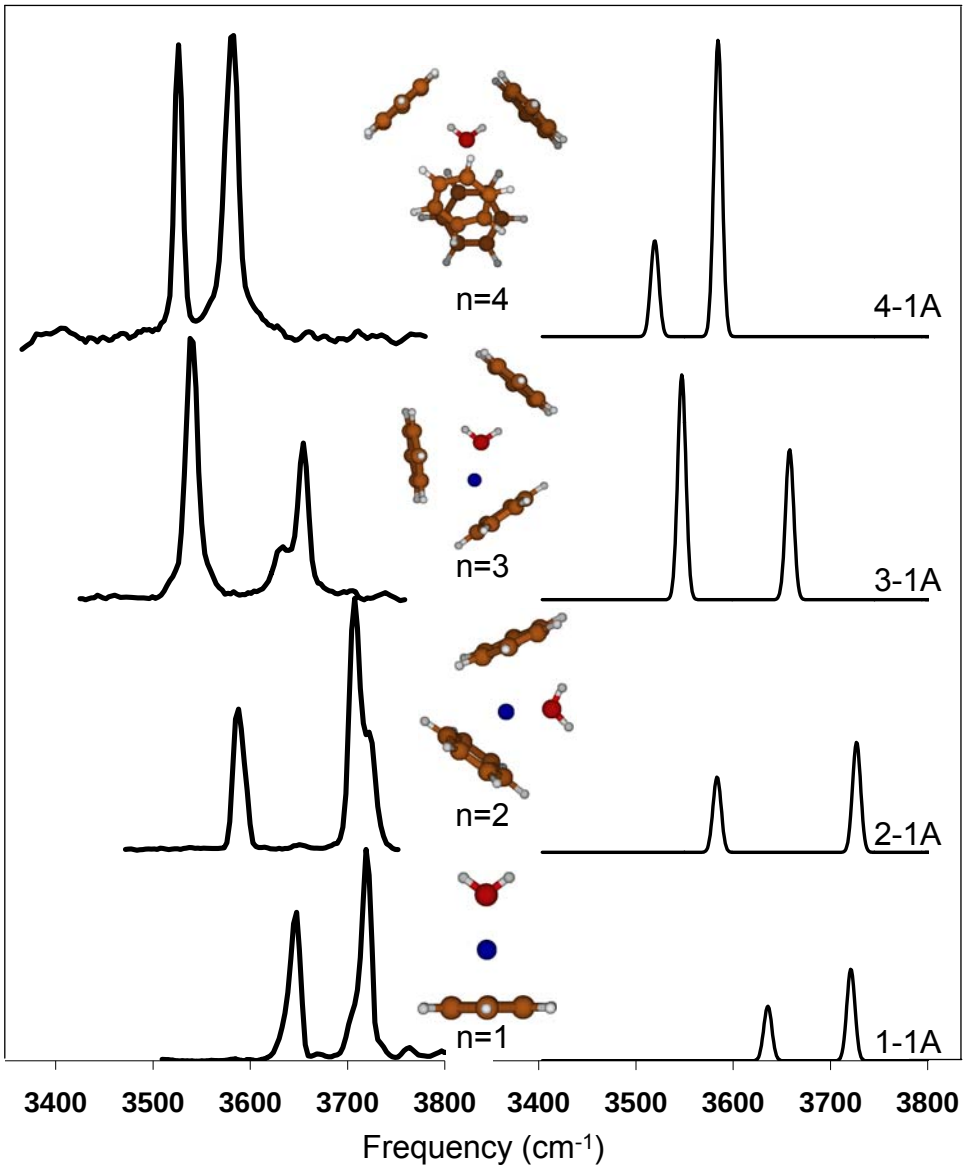

Figure 5.1. IRPD spectra (left) of $Li^+(C_6H_6)_n(H_2O)_1Ar$ recorded in the Ar loss channel. The photodissociation cross section (arb. units) is plotted as a function of laser frequency (cm^{-1}). The calculated global minimum energy structures and their simulated spectra (right) are also shown.

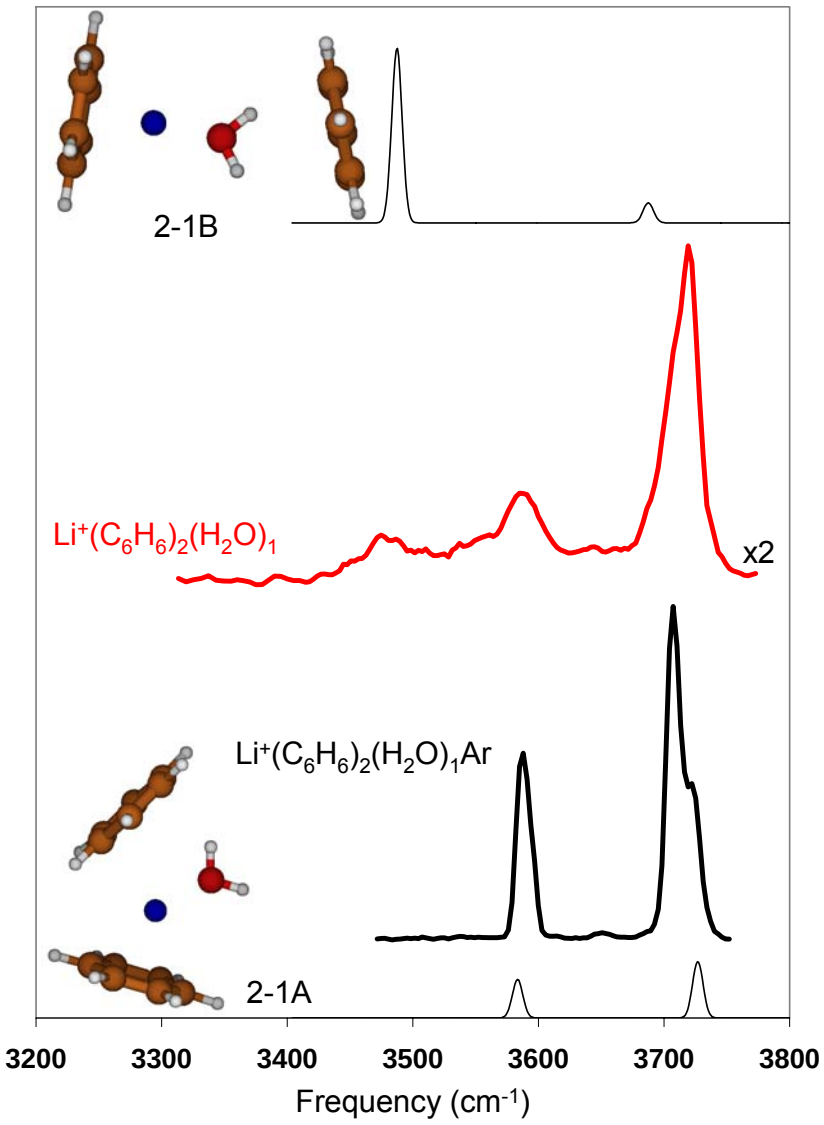

Figure 5.2. IRPD spectra of $Li^+(C_6H_6)_2(H_2O)_1Ar$ (black trace) and $Li^+(C_6H_6)_2(H_2O)_1$ (red trace, scaled by a constant value of 2). Calculated structures and spectra of isomers 2-1A (bottom) and 2-1B (top) are also displayed.

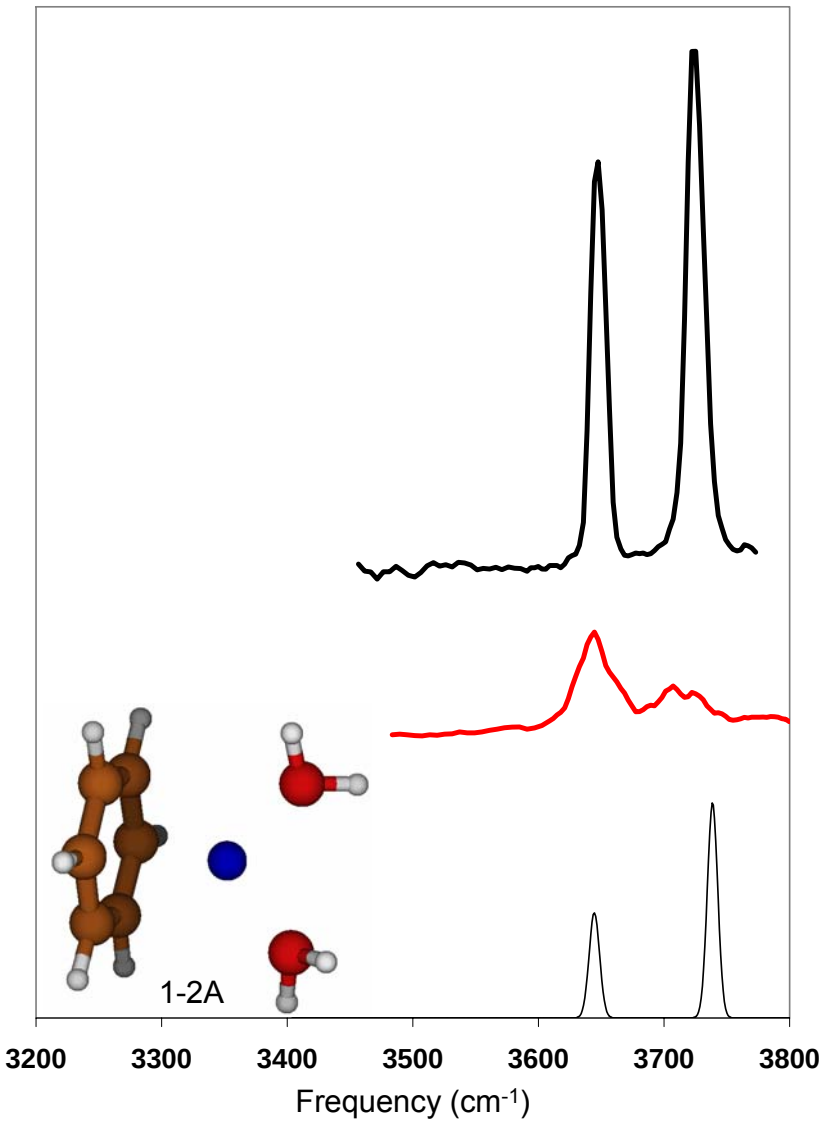

Figure 5.3. IRPD spectra of $Li^+(C_6H_6)_1(H_2O)_2$ (red trace, middle) and $Li^+(C_6H_6)_1(H_2O)_2Ar$ (black trace, top). The calculated structure and spectra of the global minimum energy isomer 1-2A are also displayed at the bottom.

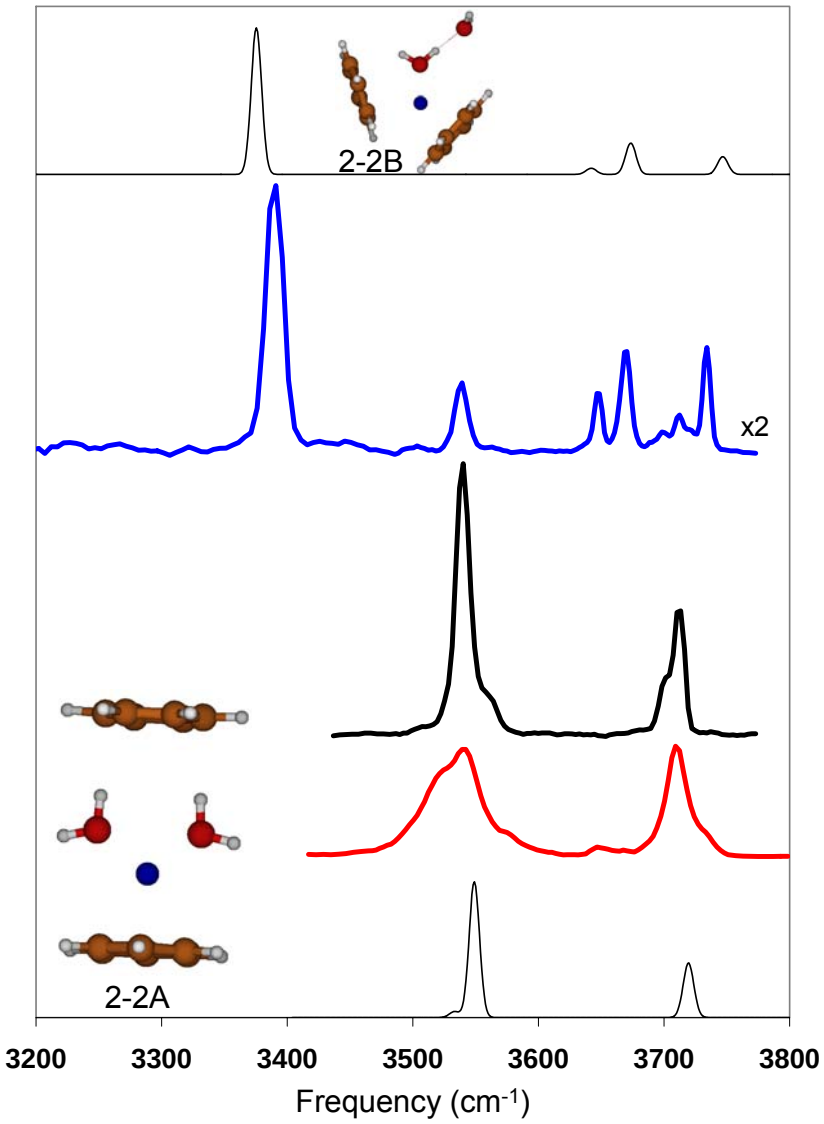

Figure 5.4. IRPD spectra of $Li^+(C_6H_6)_2(H_2O)_2$ (red trace, second from bottom) and $Li^+(C_6H_6)_2(H_2O)_2Ar$ in the Ar (black trace, third from bottom) and Ar + C_6H_6 (blue trace, fourth from bottom, scaled by a constant value of 2) loss channels. Calculated structures and spectra of isomers 2-2A (bottom) and 2-2B (top) are also displayed.

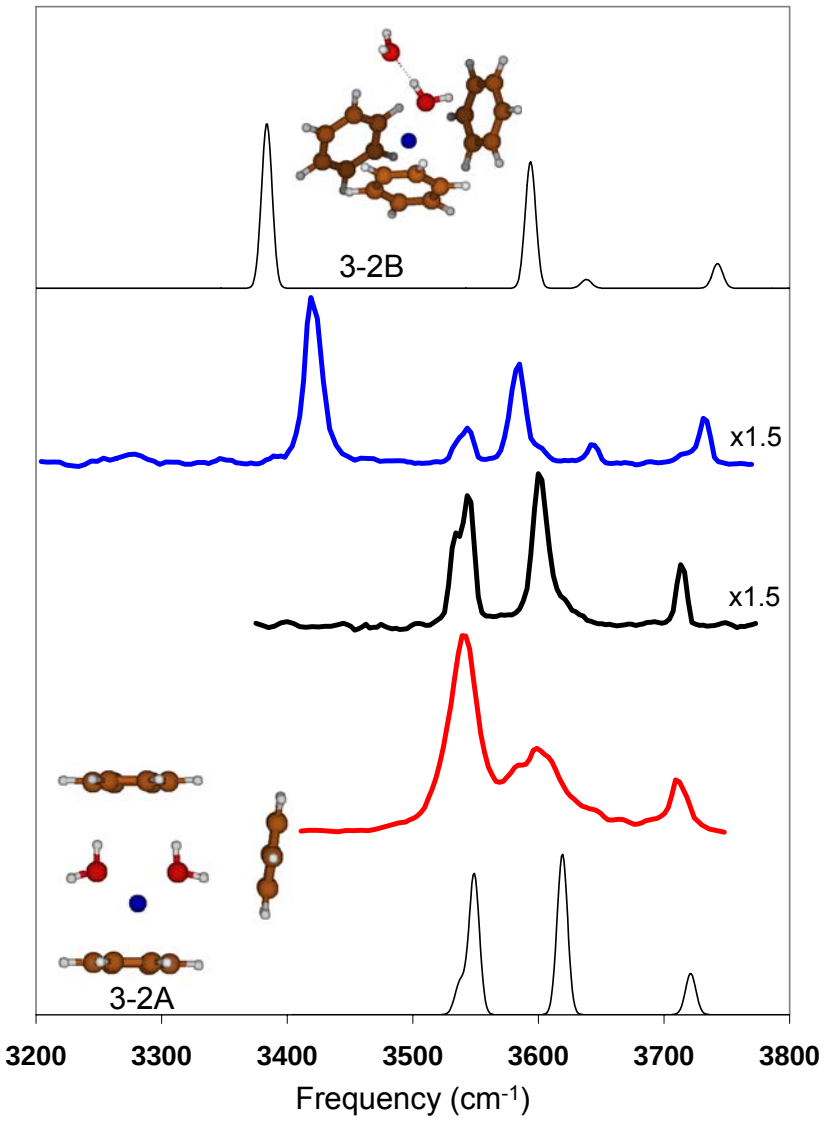

Figure 5.5. IRPD spectra of $Li^+(C_6H_6)_3(H_2O)_2$ (red trace, second from bottom) and $Li^+(C_6H_6)_3(H_2O)_2Ar$ in the Ar (black trace, third from bottom) and Ar + C_6H_6 (blue trace, fourth from bottom) loss channels. The experimental IRPD $Li^+(C_6H_6)_3(H_2O)_2Ar$ spectra have been scaled by a constant value of 1.5 for better visualization. Calculated structures and spectra of isomers 3-2A (bottom) and 3-2B (top) are also displayed.

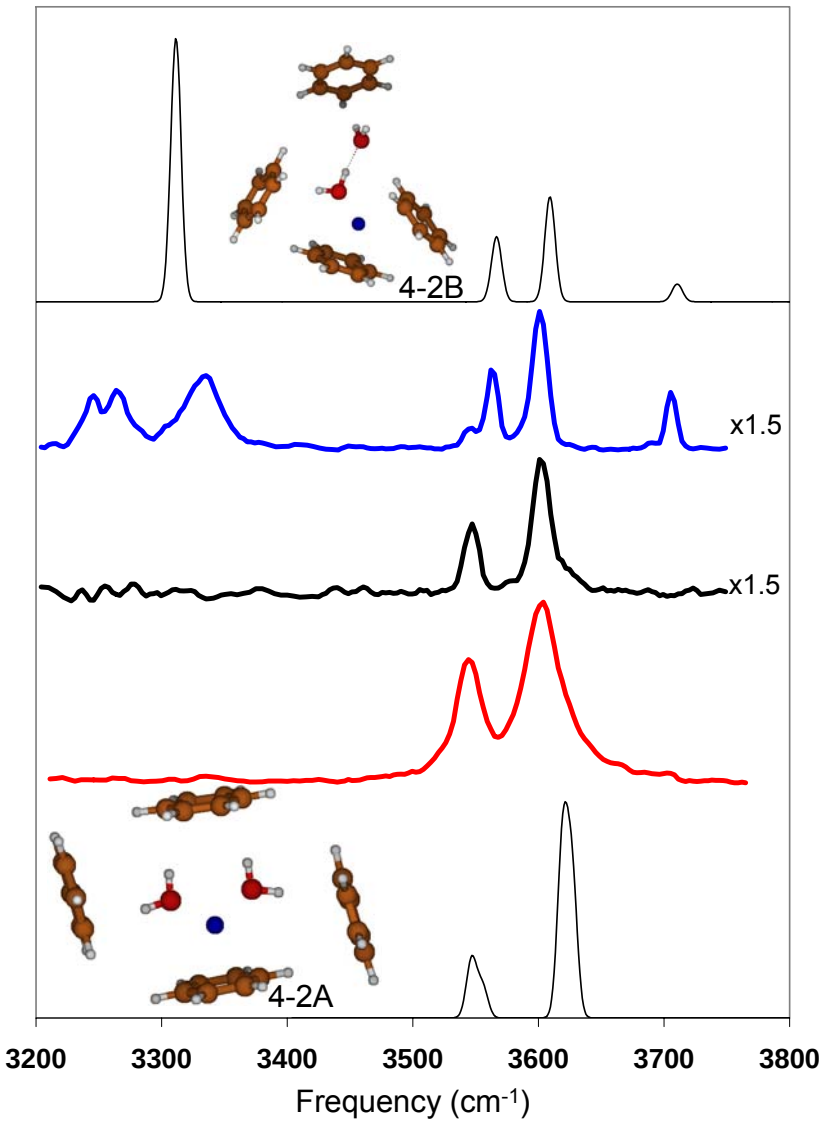

Figure 5.6. IRPD spectra of $Li^+(C_6H_6)_4(H_2O)_2$ (red trace, second from bottom) and $Li^+(C_6H_6)_4(H_2O)_2Ar$ in the Ar (black trace, third from bottom) and Ar + C_6H_6 (blue trace, fourth from bottom) loss channels. The experimental IRPD $Li^+(C_6H_6)_4(H_2O)_2Ar$ spectra have been scaled by a constant value of 1.5 for better visualization. Calculated structures and spectra of isomers 4-2A (bottom) and 4-2B (top) are also displayed.

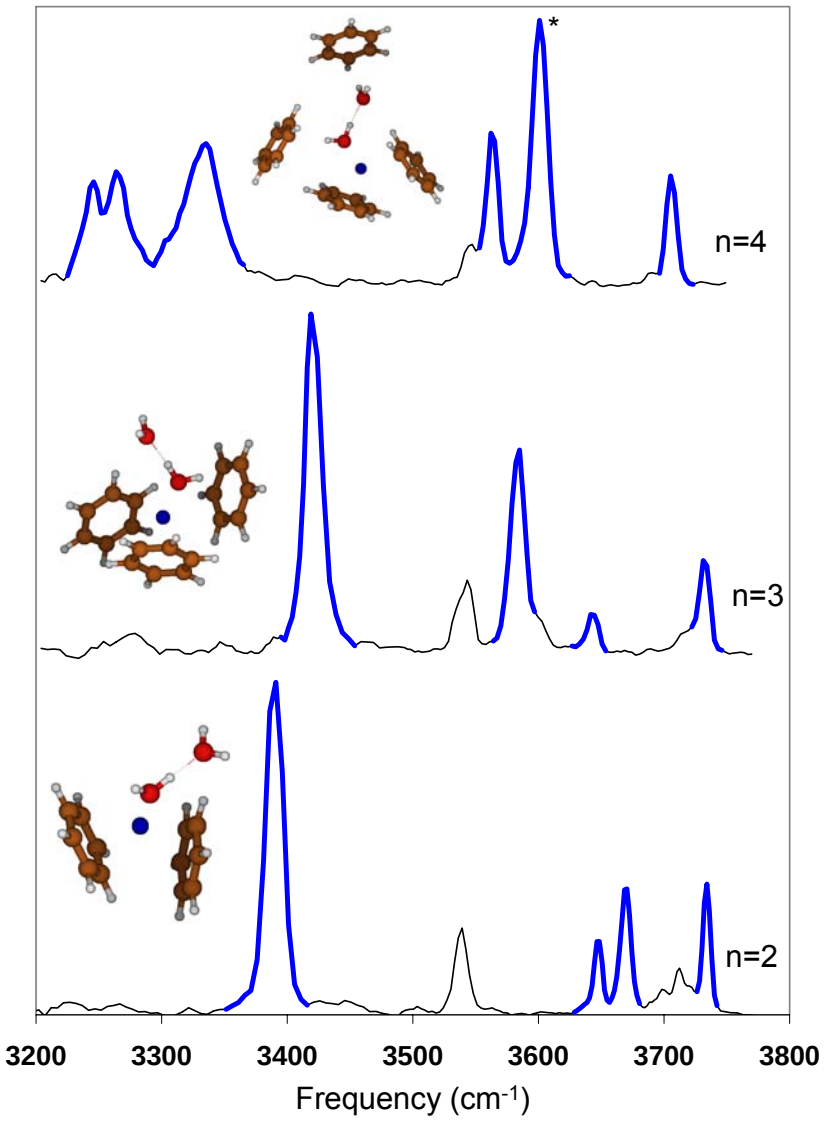

Figure 5.7. IRPD spectra of $Li^+(C_6H_6)_n(H_2O)_2Ar$ each recorded in the ($Ar + C_6H_6$) loss channel. The spectral features assigned to the high energy isomers displayed in the figure are highlighted in blue. The features not highlighted are due to the global minimum energy isomers. In the n=4 spectrum, the feature marked with an asterisk comes from a combination of the high energy isomer and the global minimum energy structure.

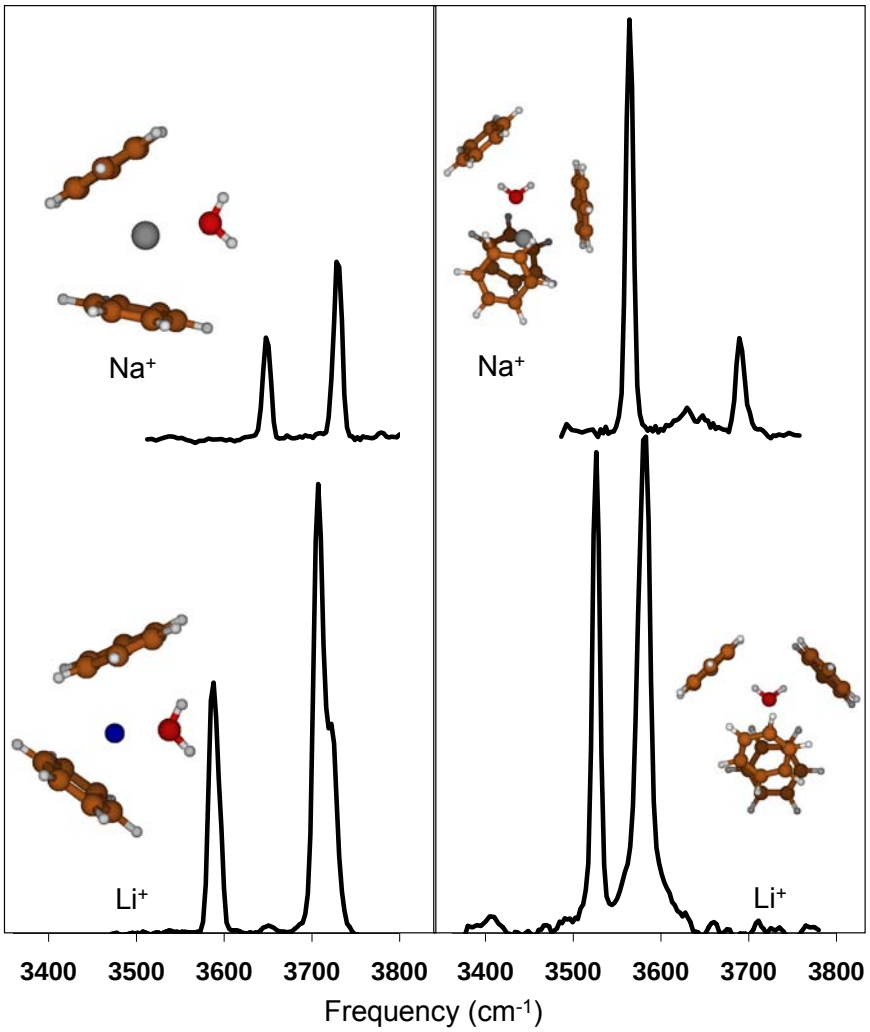

Figure 5.8. IRPD spectra of $M^+(C_6H_6)_2(H_2O)_1Ar$, left, and $M^+(C_6H_6)_4(H_2O)_1Ar$, right, where M = Li, Na. Each of the spectra was recorded in the Ar loss channel. The calculated global energy minimum structure for each cluster is also shown.

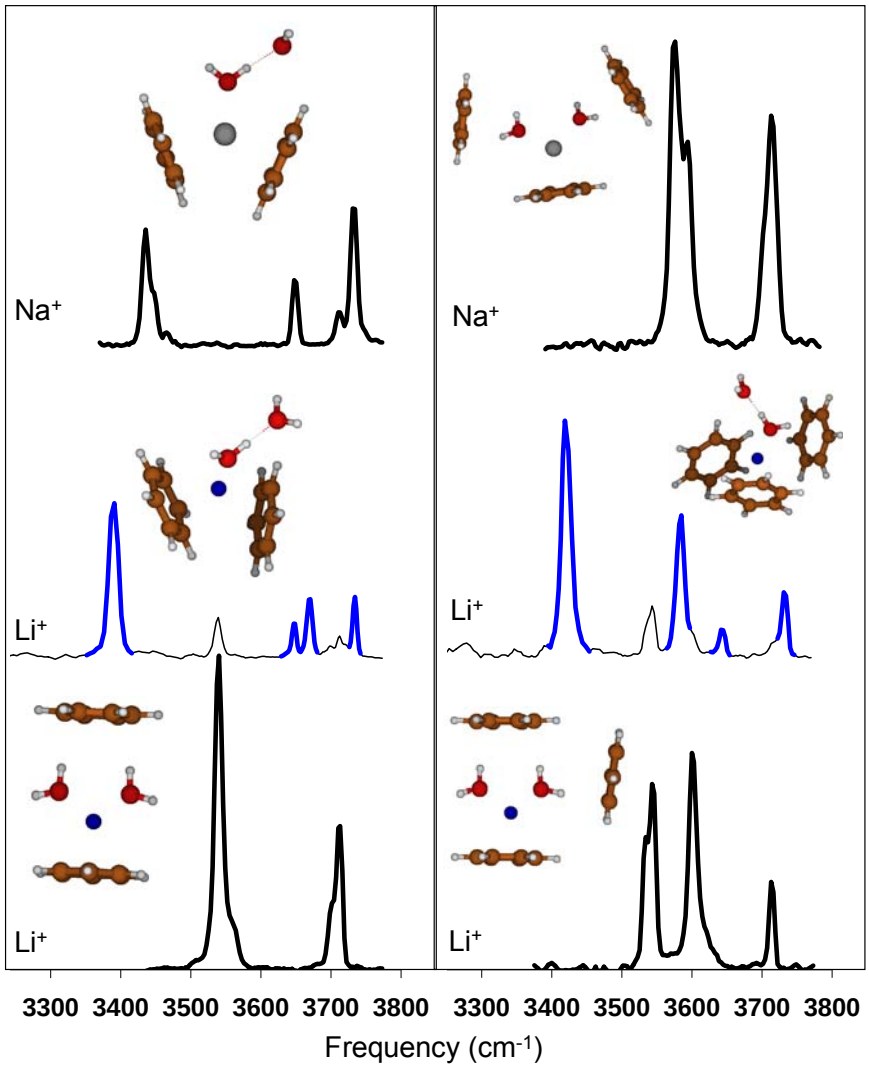

Figure 5.9. IRPD spectra of $M^+(C_6H_6)_2(H_2O)_2Ar$, left, and $M^+(C_6H_6)_3(H_2O)_2Ar$, right, where M = Li, Na. The spectra on the bottom and top were acquired in the loss of Ar channel. The middle spectra were acquired in the loss of (Ar + C_6H_6) channel with spectral features assigned to the high energy isomers highlighted in blue. A calculated structure for each cluster is also shown.

5.6 Tables

Table 5.1. The average and full width at half of the maximum (FWHM) of the internal energy and effective temperature distributions of several clusters at the middle of the second quadrupole. These values are based on RRKM-EE calculations.

	Internal Energy (kJ/mol)		Temperature (K)	
	Average[a]	FWHM	Average[a]	FWHM
$Li^+(C_6H_6)_1(H_2O)_1$	79 (12)	136	600 (60)	720
$Li^+(C_6H_6)_2(H_2O)_1$	48 (8)	58	330 (30)	250
$Li^+(C_6H_6)_3(H_2O)_1$	41 (6)	59	240 (20)	240
$Li^+(C_6H_6)_1(H_2O)_2$	53 (8)	83	410 (40)	420
$Li^+(C_6H_6)_2(H_2O)_2$	40 (6)	46	270 (30)	200
$Li^+(C_6H_6)_1(H_2O)_1Ar$	4 (1)	7	70 (10)	120
$Li^+(C_6H_6)_2(H_2O)_2Ar$	4 (1)	6	50 (10)	60

[a]Uncertainty estimates given in parentheses are due to uncertainties in the ligand binding energies (±10%) used in the RRKM-EE calculations.

Table 5.2. Experimentally observed and calculated OH stretching frequencies (cm^{-1}) for $Li^+(C_6H_6)_{1\text{-}4}(H_2O)_1Ar$ along with their assignments.

Cluster	Exp Freq	Calc Freq	OH Stretching Assignment	Isomer
$Li^+(C_6H_6)_1(H_2O)_1Ar$	3720	3721	Asymmetric	1-1A
	3646	3636	Symmetric	1-1A
$Li^+(C_6H_6)_2(H_2O)_1Ar$	3707	3727	Free	2-1A
	3586	3583	Weak OH-π interaction	2-1A
$Li^+(C_6H_6)_3(H_2O)_1Ar$	3655	3658	Weak OH-π interaction	3-1A
	3540	3547	π-H-bond	3-1A
$Li^+(C_6H_6)_4(H_2O)_1Ar$	3581	3584	Asymmetric π-H-bond	4-1A
	3526	3520	Symmetric π-H-bond	4-1A

Table 5.3. Relative energies (kJ/mol) and binding energies (kJ/mol) for the $Li^+(C_6H_6)_{1-4}(H_2O)_{1-2}$ structures presented in Figures 5.1-5.6 using both B3LYP/6-31+G* and MP2/6-31+G* calculations. Vibrational zero point energy corrections are included in these calculations.

	Relative Energy		Benzene Binding Energy[a]		Water Binding Energy[a]		Ar Binding Energy[b]	
Cluster	**B3LYP**	**MP2**	**B3LYP**	**MP2**	**B3LYP**	**MP2**	**B3LYP**	**MP2**
1-1A	0	0	121	132	116	126	2	8
2-1A	0	0	35	64	-	-	-	-
2-1B	1	18	34	46	-	-	-	-
3-1A	0	0	26	49	-	-	-	-
4-1A	0	0	14	32[c]	-	-	-	-
1-2A	0	0	64	85	71	83	-	-
2-2A	0	0	36	50	73	87	1	7
2-2B	22	13	26	57	50	56	-	-
3-2A	0	-	22	43[c]	68	-	-	-
3-2B	29	-	15	-	39	-	-	-
4-2A	0	-	20	-	74	-	-	-
4-2B	28	-	21	-	46	-	-	-

[a]Benzene and water binding energies based on calculations of structures not including argon.
[b]Ar binding energies based on calculations of structures including argon.
[c]Single point energy calculation of B3LYP optimized geometry, vibrational zero point energy corrections not included.

Table 5.4. Experimentally observed and calculated OH stretching frequencies (cm^{-1}) for $Li^+(C_6H_6)_{1-4}(H_2O)_2Ar$ along with their assignments.

Cluster	Exp Freq	Calc Freq	OH Stretching Assignment	Isomer
$Li^+(C_6H_6)_1(H_2O)_2Ar$	3725	3738	Asymmetric	1-2A
	3648	3645	Symmetric	1-2A
$Li^+(C_6H_6)_2(H_2O)_2Ar$	3734	3747	Asymmetric	2-2B
	3713	3720	Free	2-2A
	3670	3674	Weak OH-π interaction	2-2B
	3648	3641	Symmetric	2-2B
	3540	3549	π-H-bond	2-2A
	3390	3375	Water-water H-bond	2-2B
$Li^+(C_6H_6)_3(H_2O)_2Ar$	3733	3742	Asymmetric	3-2B
	3714	3721	Free	3-2A
	3644	3638	Symmetric	3-2B
	3601	3619	Asymmetric π-H-bond	3-2A
	3584	3594	π-H-bond	3-2B
	3545	3549	π-H-bond	3-2A
	3534	3533	Symmetric π-H-bond	3-2A
	3420	3384	Water-water H-bond	3-2B
$Li^+(C_6H_6)_4(H_2O)_2Ar$	3706	3710	Free	4-2B
	3603	3623	Asymmetric π-H-bond	4-2A
	3601	3608	π-H-bond of 1st shell water	4-2B
	3564	3567	π-H-bond of 2nd shell water	4-2B
	3547	3551	Symmetric π-H-bond	4-2A
	3322	3311	Water-water H-bond	4-2B

5.7 References

(1) Marechal, Y. *The Hydrogen Bond and the Water Molecule*, 1 ed.; Elsevier: Amsterdam, 2007.
(2) Nelson, D. L.; Cox, N. M. *Lehninger Principles of Biochemistry*, 3rd ed.; Worth Publishers: New York, NY, 2000.
(3) McQuarrie, D. A.; Simon, J. D. *Physical Chemistry A Molecular Approach*; University Science Books: Sausalito, 1997.
(4) Davis, J. T. *Nature Chemistry* **2010**, *2*, 516.
(5) Dougherty, D. A. *Science* **1996**, *271*, 163.
(6) Kumpf, R. A.; Dougherty, D. A. *Science* **1993**, *261*, 1708.
(7) Ma, J. C.; Dougherty, D. A. *Chemical Reviews* **1997**, *97*, 1303.
(8) Mecozzi, S.; West, A. P.; Dougherty, D. A. *Journal of the American Chemical Society* **1996**, *118*, 2307.
(9) Gruenloh, C. J.; Carney, J. R.; Arrington, C. A.; Zwier, T. S.; Fredericks, S. Y.; Jordan, K. D. *Science* **1997**, *276*, 1678.
(10) Pribble, R. N.; Aaron, W. G.; Kenneth, H.; Timothy, S. Z. *The Journal of Chemical Physics* **1995**, *103*, 531.
(11) Pribble, R. N.; Zwier, T. S. *Science* **1994**, *265*, 75.
(12) Zwier, T. S. *Annual Review of Physical Chemistry* **1996**, *47*, 205.
(13) Cabarcos, O. M.; Weinheimer, C. J.; Lisy, J. M. *Journal of Chemical Physics* **1998**, *108*, 5151.
(14) Cabarcos, O. M.; Weinheimer, C. J.; Lisy, J. M. *The Journal of Chemical Physics* **1999**, *110*, 8429.
(15) Miller, D. J.; Lisy, J. M. *Journal of the American Chemical Society* **2008**, *130*, 15381.
(16) Rodriguez, J. D.; Lisy, J. M. *International Journal of Mass Spectrometry* **2009**, *283*, 135.
(17) Beck, J. P.; Lisy, J. M. *The Journal of Physical Chemistry A* **2010**, *114*, 10011.
(18) Miller, D. J.; Lisy, J. M. *The Journal of Chemical Physics* **2006**, *124*, 184301.
(19) Nicely, A. L.; Miller, D. J.; Lisy, J. M. *Journal of the American Chemical Society* **2009**, *131*, 6314.
(20) Frisch, M. J. T., G. W.; Schlegel, H. B.; Scuseria, G. E.; Robb, M. A.; Cheeseman, J. R.; Montgomery, Jr., J. A.; Vreven, T.; Kudin, K. N.; Burant, J. C.; Millam, J. M.; Iyengar, S. S.; Tomasi, J.; Barone, V.; Mennucci, B.; Cossi, M.; Scalmani, G.; Rega, N.; Petersson, G. A.; Nakatsuji, H.; Hada, M.; Ehara, M.; Toyota, K.; Fukuda, R.; Hasegawa, J.; Ishida, M.; Nakajima, T.; Honda, Y.; Kitao, O.; Nakai, H.; Klene, M.; Li, X.; Knox, J. E.; Hratchian, H. P.; Cross, J. B.; Bakken, V.; Adamo, C.; Jaramillo, J.; Gomperts, R.; Stratmann, R. E.; Yazyev, O.; Austin, A. J.; Cammi, R.; Pomelli, C.; Ochterski, J. W.; Ayala, P. Y.; Morokuma, K.; Voth, G. A.; Salvador, P.; Dannenberg, J. J.; Zakrzewski, V. G.; Dapprich, S.; Daniels, A. D.; Strain, M. C.; Farkas, O.; Malick, D. K.; Rabuck, A. D.; Raghavachari, K.; Foresman, J. B.; Ortiz, J. V.; Cui, Q.; Baboul, A. G.; Clifford, S.; Cioslowski, J.; Stefanov, B. B.; Liu, G.; Liashenko, A.; Piskorz, P.; Komaromi, I.; Martin, R. L.; Fox, D. J.; Keith, T.; Al-Laham, M. A.; Peng, C. Y.; Nanayakkara, A.; Challacombe, M.; Gill, P. M. W.; Johnson, B.; Chen, W.;

Wong, M. W.; Gonzalez, C.; and Pople, J. A. Gaussian 03, Revision D.01; Gaussian, Inc.: Wallingford CT, 2004.
(21) Fraley, P. E.; Narahari Rao, K. *Journal of Molecular Spectroscopy* **1969**, *29*, 348.
(22) Gorelsky, S. I. *SWizard program*; 4.1 ed., 2005.
(23) Marcus, R. A. *The Journal of Chemical Physics* **1952**, *20*, 359.
(24) Klots, C. E. *The Journal of Chemical Physics* **1985**, *83*, 5854.
(25) Klots, C. E. *Zeitschrift fÃ¼r Physik D Atoms, Molecules and Clusters* **1987**, *5*, 83.
(26) Klots, C. E. *Journal of Physical Chemistry* **1988**, *92*, 5864.
(27) Vaden, T. D.; Weinheimer, C. J.; Lisy, J. M. *Journal of Chemical Physics* **2004**, *121*, 3102.
(28) Cabarcos, O. M.; Weinheimer, C. J.; Lisy, J. M. *J. Phys. Chem. A* **1999**, *103*, 8777.
(29) Miller, D. J.; Lisy, J. M. *Journal of the American Chemical Society* **2008**, *130*, 15393.
(30) Ayotte, P.; Weddle, G. H.; Johnson, M. A. *Journal of Chemical Physics* **1999**, *110*, 7129.
(31) Ayotte, P.; Weddle, G. H.; Kim, J.; Johnson, M. A. *Journal of the American Chemical Society* **1998**, *120*, 12361.
(32) Carney, J. R.; Zwier, T. S. *Journal of Physical Chemistry A* **2000**, *104*, 8677.
(33) Dian, B. C.; Clarkson, J. R.; Zwier, T. S. *Science* **2004**, *303*, 1169.

Chapter 6: IRPD of Benzyl Alcohol Containing Clusters: Trending Toward Biologically Relevant Ligands

6.1 Introduction

In chapter 5 of this dissertation, competition between cation•••π, cation•••dipole, O-H•••π, and O-H•••O interactions was investigated using ion-benzene-water clusters. In more biologically relevant aromatic systems, polar regions exist that can form inter- or intra-molecular bonds and therefore alter the relative stability of the various non-covalent interactions[1,2]. For example, the amino acids tryptophan and tyrosine contain aromatic, polar side chains[3]. Additionally, neurotransmitters such as epinephrine[4], and sympathomimetic amines such as ephedrine[5] have both aromatic and polar regions. Thus, it is highly desirable to build on the knowledge gained from the results of the previous chapter by studying a system containing a polar, aromatic ligand.

A significant amount of research along these lines has already been reported by the Lisy group[6-11]. Some of the aromatic molecules studied previously are displayed in Figure 6.1. Phenol contains an aromatic ring with a substituted OH group. Thus, when a cation binds to phenol, it will interact either with oxygen lone pairs (σ-type interaction) or the π electrons[9]. Due to the phenol geometry, the cation cannot form both bonds simultaneously. It was shown that π interactions dominated the non-hydrated $M^+(Phenol)_1$ clusters, while σ-type interactions dominated hydrated $M^+(Phenol)_1(H_2O)_n$ clusters, M = Na, K[9].

Following the work on phenol, investigations were performed on a variety of other biologically relevant molecules including indole[6], tryptamine[7,8], and 2-amino-1-phenyl ethanol (APE) [7]. These studies demonstrated how an alkali metal cation altered

the geometry of the biomolecule. For tryptamine and APE, this lead to the detection of conformers previously unobserved in neutral cluster studies.

In this chapter, the results of a study on M^+(benzyl alcohol)$_1$(H_2O)$_{0-2}$Ar cluster ions are reported. Benzyl alcohol (BA) was chosen as a way to bridge the gap between the small phenol molecule where no intramolecular hydrogen bonding occurs, and the larger APE molecule, which has two polar sites. Benzyl alcohol is interesting because it is one of the simplest molecules capable of forming an intramolecular O-H•••π hydrogen bond and has therefore generated a great deal of attention from experimentalists and computationalists[12-34]. It is now generally agreed that neutral, gas-phase BA has the gauche/cis orientation (gauche refers to the C_{ortho}-C_{ipso}-C_{α}-O orientation, cis refers to the orientation of the O-H relative to the ring) shown in Figure 6.1 with a very weak (~ 1 kJ/mol) O-H•••π hydrogen bond, while cationic BA has a planar/trans structure with no hydrogen bond. Furthermore, according to IR-UV double resonance experiments and calculations, benzyl alcohol in neutral BA(H_2O)$_n$ clusters acts as the proton donor in O-H•••O hydrogen bonds[19,22,23].

Given these previous studies, investigating the impact of alkali metal ions on the structure and bonding of (BA)$_1$(H_2O)$_{0-2}$ is worthwhile. This is accomplished through a combination of *ab initio* electronic structure calculations and infrared spectroscopy of M^+(BA)$_1$(H_2O)$_{0-2}$Ar cluster ions, M = Li, Na. Based on the results of chapter 5, the lithium ion was chosen in anticipation of trapping out and probing high energy conformers. Sodium is used to compare with lithium and gauge the impact of ion size.

6.2 Experimental and Computational Details

Infrared predissociation (IRPD) spectra were acquired using the experimental apparatus described in chapter 2. The benzyl alcohol was purchased from Sigma Aldrich and introduced into the system using either the bubbler or the heated sample holder with gentle heating (< 40°C). Without exception, the spectra reported below were acquired in the Ar loss channel as no fragmentation into other loss channels was observed.

MP2/6-31+G* *ab initio* calculations were performed to generate optimized $M^+(BA)_1(H_2O)_{0-2}$ structures and corresponding simulated spectra. Spartan 08[35] was used to generate initial neutral $(BA)_1(H_2O)_{0-2}$ structures which were optimized using GAUSSIAN 03[36]. An alkali ion was introduced at several locations of the optimized neutral clusters and the resulting cluster ions were optimized using GAUSSIAN 03. Frequency calculations were performed for the unique optimized cluster ion structures. Reported energies include zero point energy corrections. Simulated spectra were generated with the SWizard[37] program applying a Gaussian line shape with 10 cm^{-1} width to each feature. The BA OH stretches were scaled by 0.977 and the water OH stretches were scaled by 0.970 to match gas phase neutral values.

6.3 Results and Discussion

$Li^+(BA)_1(H_2O)_nAr$

The spectra of $Li^+(BA)_1(H_2O)_nAr$, n=0-2, are displayed in Figure 6.2. One sharp feature at 3666 cm^{-1} is observed in the n=0 spectrum indicating the presence of only one conformer of $Li^+(BA)_1Ar$, in line with the potential energy search which resulted in one optimized structure. According to the calculations, this conformer has the C-O bond perpendicular to the plane of the benzyl ring with the O-H bond pointing away from the

ring (a perpendicular/trans BA configuration). The ion is positioned asymmetrically above the ring so that it can interact with the oxygen lone pairs and the benzyl π electrons. This structure is much different than the either the neutral or cationic BA configuration[20,24,25,29], underscoring the importance of the ion in dictating structure. In this case, the ability of the ion to interact with the oxygen and the π electrons takes prescedence over the weak intramolecular O-H•••π bond in the neutral BA structure.

Upon addition of a single water, the n=1 spectrum has four new features, indicating the presence of multiple $Li^+(BA)_1(H_2O)_1Ar$ conformers. To aid in the assignment, calculated structures and simulated spectra are presented in Figure 6.3. The experimental spectrum has a distinct feature at 3583 cm^{-1}. This is in the region of a weak O-H•••π interaction as observed in the $Li^+(C_6H_6)_2(H_2O)_1Ar$ spectrum presented in the previous chapter. The global minimum energy conformer Li1A is the only calculated conformer with a water O-H•••π interaction. In this structure, Li^+ interacts with both oxygen atoms and the benzyl π electrons. Due to the small ion size, the water is also able to interact with the π electrons. Conformer Li1A accounts for the three experimental features at 3583 cm^{-1} (O-H•••π), 3662 cm^{-1} (BA OH stretch), and 3714 cm^{-1} (free OH stretch). The prominent features at 3288 cm^{-1} and 3735 cm^{-1} are yet to be assigned. Based on the calculations there are two possibilities for these features: conformer Li1D, or a combination of conformers Li1B and Li1C. Conformers Li1B and Li1D each contain a strong hydrogen bonded OH stretching feature below 3450 cm^{-1}, with conformer Li1D giving better overall agreement with experiment. Despite being considerably higher in energy, conformer Li1D would be more likely to be trapped out in the cluster ion generation process because neutral $(BA)_1(H_2O)_1$ clusters contain a

hydrogen bond directed from the benzyl alcohol towards the water[19,22,23]. Thus, trapping conformer Li1D could be accomplished without breaking and reforming the hydrogen bond. We therefore tentatively assign the experimental peaks at 3288 cm^{-1} and 3735 cm^{-1} to the BA•••OH_2 hydrogen bond and water asymmetric stretches, respectively.

Adding a second water to the system only minimally alters the experimental spectrum. The four lowest energy calculated conformers for $Li^+(BA)_1(H_2O)_2$ along with their simulated spectra are displayed in Figure 6.4. As was the case for n=1, the $Li^+(BA)_1(H_2O)_2Ar$ spectrum *could* be assigned as coming from conformers Li2A and Li2D. Compared to the n=1 spectrum, the feature in the n=2 spectrum corresponding to the O-H•••π interaction is shifted to lower frequency, consistent with the global minimum energy structure Li2A. In order to maximize the Li^+•••O interactions in this conformer, the ion is drawn away from the benzyl ring compared to structure Li1A. Therefore, one water in conformer Li2A is able to move closer to the ring, resulting in a stronger, more direct O-H•••π interaction (see Table 6.1 for structural parameters). The prominent experimental spectral feature at 3330 cm^{-1} is due to a hydrogen bonded benzyl alcohol OH stretch. This feature is not as red-shifted compared to the analogous feature in the n=1 spectrum. This is due to the presence of the water bound to the ion which reduces the Li^+•••BA interaction, resulting in a smaller red-shift.

The assignments given in the previous paragraph are reasonable and agree with the experimental evidence. However, based on the calculations, the presence of other conformers cannot be ruled out. In fact, there is a slight asymmetry in the experimental feature at 3330 cm^{-1} which may indicate the presence of two different O-H•••O-H

hydrogen bonds. This could be due to a combination of conformers Li2B and Li2D, which have nearly identical calculated hydrogen bonded OH stretching frequencies.

$Na^+(BA)_1(H_2O)_nAr$

The spectra of $Na^+(BA)_1(H_2O)_{n=0-2}Ar$ are shown in Figure 6.5. Most notably in the n=1 spectrum is the absence of the feature between 3500 – 3600 cm^{-1} which was seen for $Li^+(BA)_1(H_2O)_1Ar$. This demonstrates that, unlike its Li^+ counterpart, $Na^+(BA)_1(H_2O)_1Ar$ contains no weak O-H•••π interactions. As can be seen by the global minimum energy structure reported in Figure 6.6 and the parameters given in Table 6.1, the sodium ion is located more centrally above the benzyl ring, not allowing the water to interact with the π electrons. A very similar ion size effect was reported for $M^+(C_6H_6)_2(H_2O)_1Ar$ in the previous chapter. The small peak at 3617 cm^{-1} comes from the water symmetric stretch. Analogous to $Li^+(BA)_1(H_2O)_1Ar$, the remainder of the features in the $Na^+(BA)_1(H_2O)_1Ar$ spectrum are assigned to conformers Na1A and Na1D with possible additional contributions from Na1B and Na1C (Figure 6.6).

The assignments of the $Na^+(BA)_1(H_2O)_2Ar$ experimental spectrum are made by comparison with conformers Na2A - Na2D displayed in Figure 6.7. None of these conformers can be definitively excluded from consideration. The most notable aspect of this spectrum is the drastically reduced intensity of the hydrogen bonded OH stretching peak at 3392 cm^{-1}. This represents another major difference between the Na^+ and Li^+ containing clusters. For $Na^+(BA)_1(H_2O)_2Ar$, isomer Na2C is only a minor isomer in the cluster ensemble despite being only 19 kJ/mol higher in energy than conformer Na2A. Apparently, due to its larger size and smaller charge density compared to Li^+, Na^+

produces minima on the potential energy surface with smaller barriers to rearrangement resulting in fewer trapped high energy clusters.

6.4 Conclusions

Benzyl alcohol has a special place in the progression from small purely model systems to larger, more biologically relevant molecules as it bridges the gap between phenol and APE. IRPD spectra of $M^+(BA)_1(H_2O)_{0-2}Ar$, M = Li, Na, along with *ab initio* calculations were reported and interpreted. The presence of an alkali cation dramatically alters the conformation of benzyl alcohol. Both $Li^+(BA)$ and $Na^+(BA)$ have a perpendicular/trans structure which maximizes the ion•••electron interactions at the expense of the intramolecular O-H•••π hydrogen bond.

Upon hydration, the global minimum energy structures are once again those that maximize the solvation of the ion and there is no evidence of dominant structures with an intramolecular BA O-H•••π hydrogen bond. However, a weak water O-H•••π bond is observed for $Li^+(BA)_1(H_2O)_1Ar$, but not for $Na^+(BA)_1(H_2O)_1Ar$, a result of the difference in ion size. As evident from a red shift, the O-H•••π bond is slightly stronger in $Li^+(BA)_1(H_2O)_2Ar$ than in $Li^+(BA)_1(H_2O)_1Ar$, consistent with the calculated spectra and structures. Finally, whereas the $Li^+(BA)_1(H_2O)_2Ar$ spectrum has an intense feature at 3330 cm^{-1}, the corresponding O-H•••O hydrogen bonded OH stretching feature in the $Na^+(BA)_1(H_2O)_2Ar$ is significantly suppressed. This is more evidence of the superior high energy isomer trapping ability of Li^+ compared to Na^+.

6.5 Figures

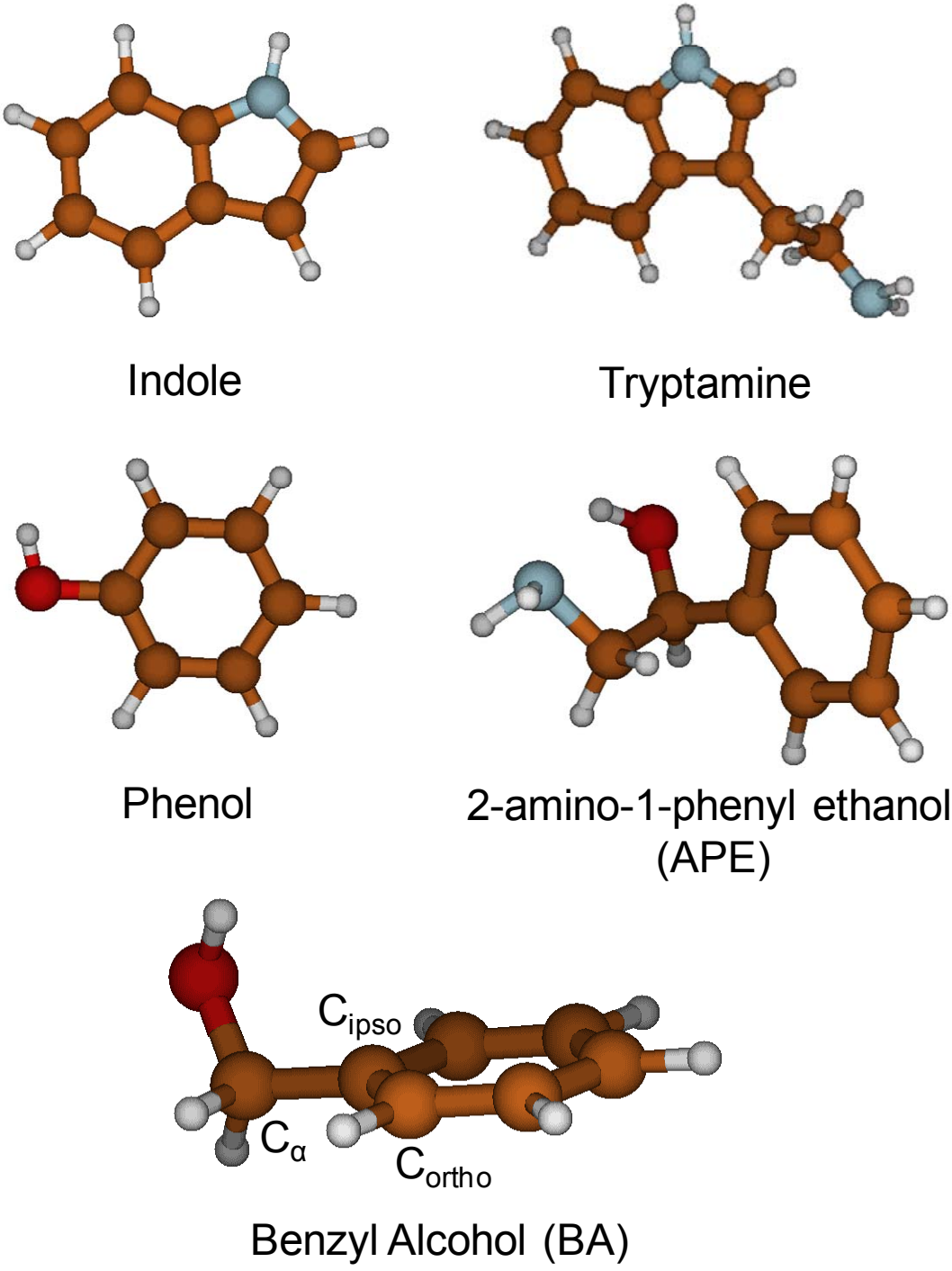

Figure 6.1. Ball-and-stick representations of molecules that have been studied previously by the Lisy group (top) and a representation of benzyl alcohol (bottom), the subject of this chapter.

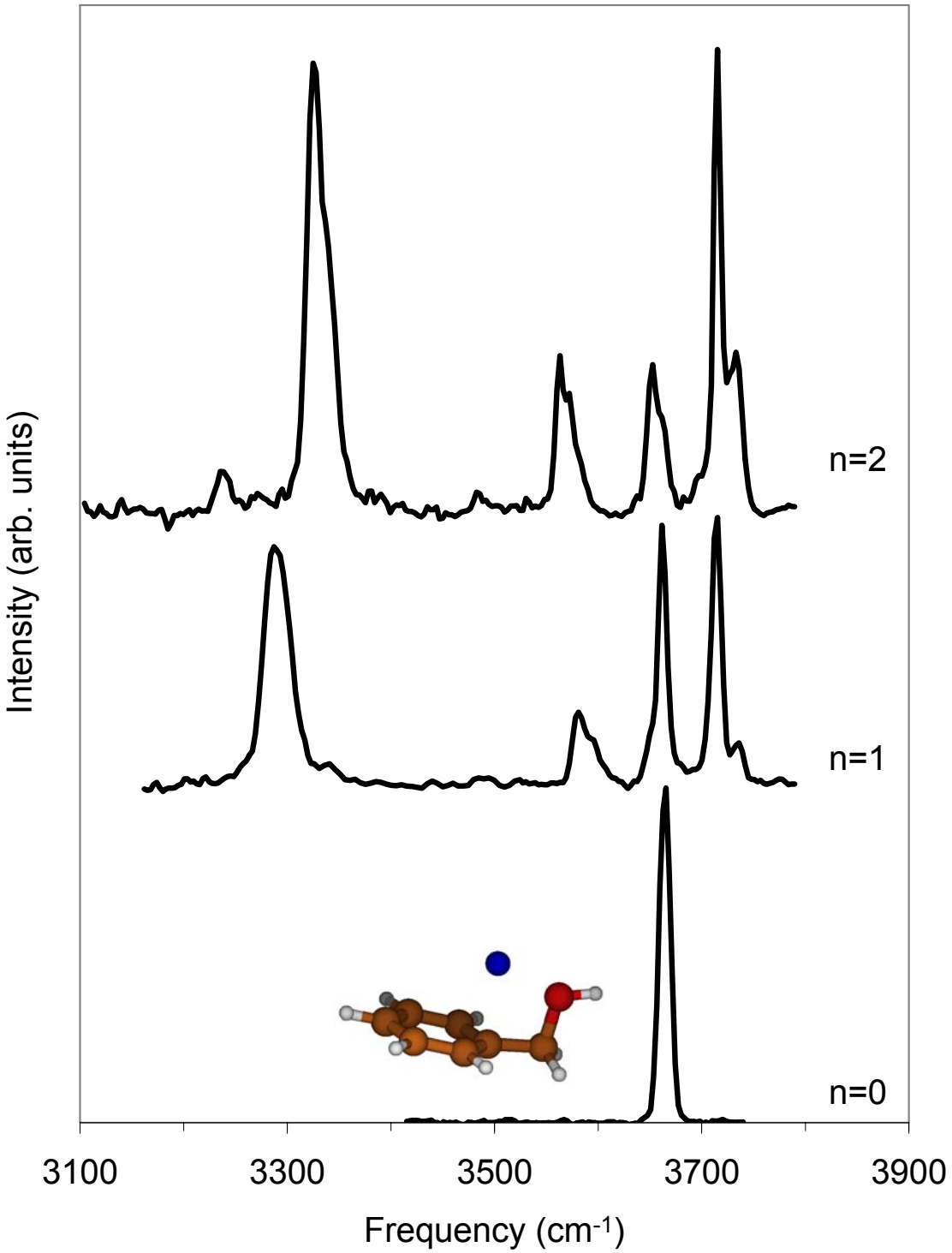

Figure 6.2. IRPD spectra of $Li^+(BA)_1(H_2O)_nAr$. The calculated minimum energy conformer of $Li^+(BA)_1Ar$ is also shown.

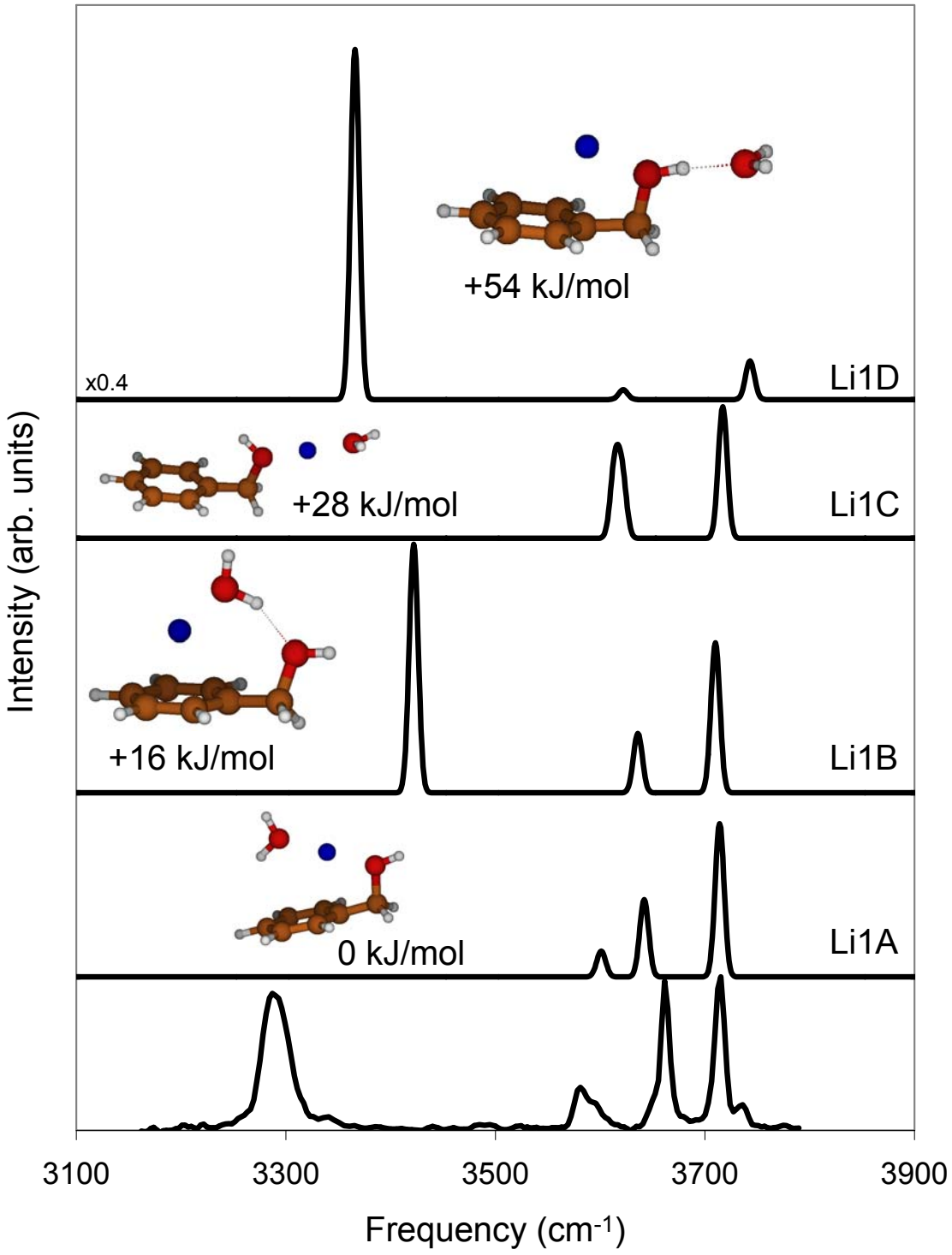

Figure 6.3. Experimental IRPD spectrum of $Li^+(BA)_1(H_2O)_1Ar$ (bottom) along with four optimized MP2/6-31+G* calculated structures and simulated spectra.

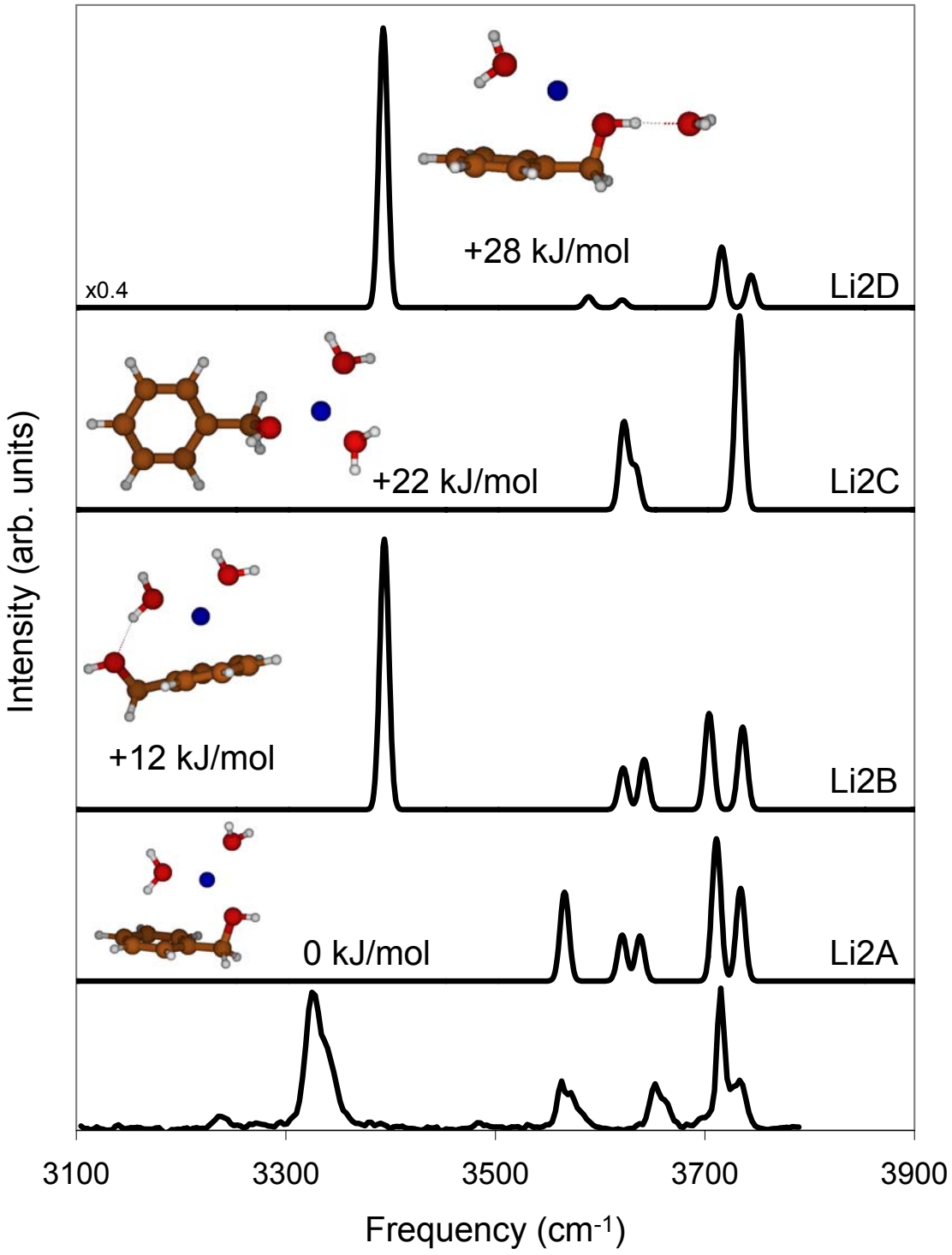

Figure 6.4. Experimental IRPD spectrum of $Li^+(BA)_1(H_2O)_2Ar$ (bottom) along with four optimized MP2/6-31+G* calculated structures and simulated spectra.

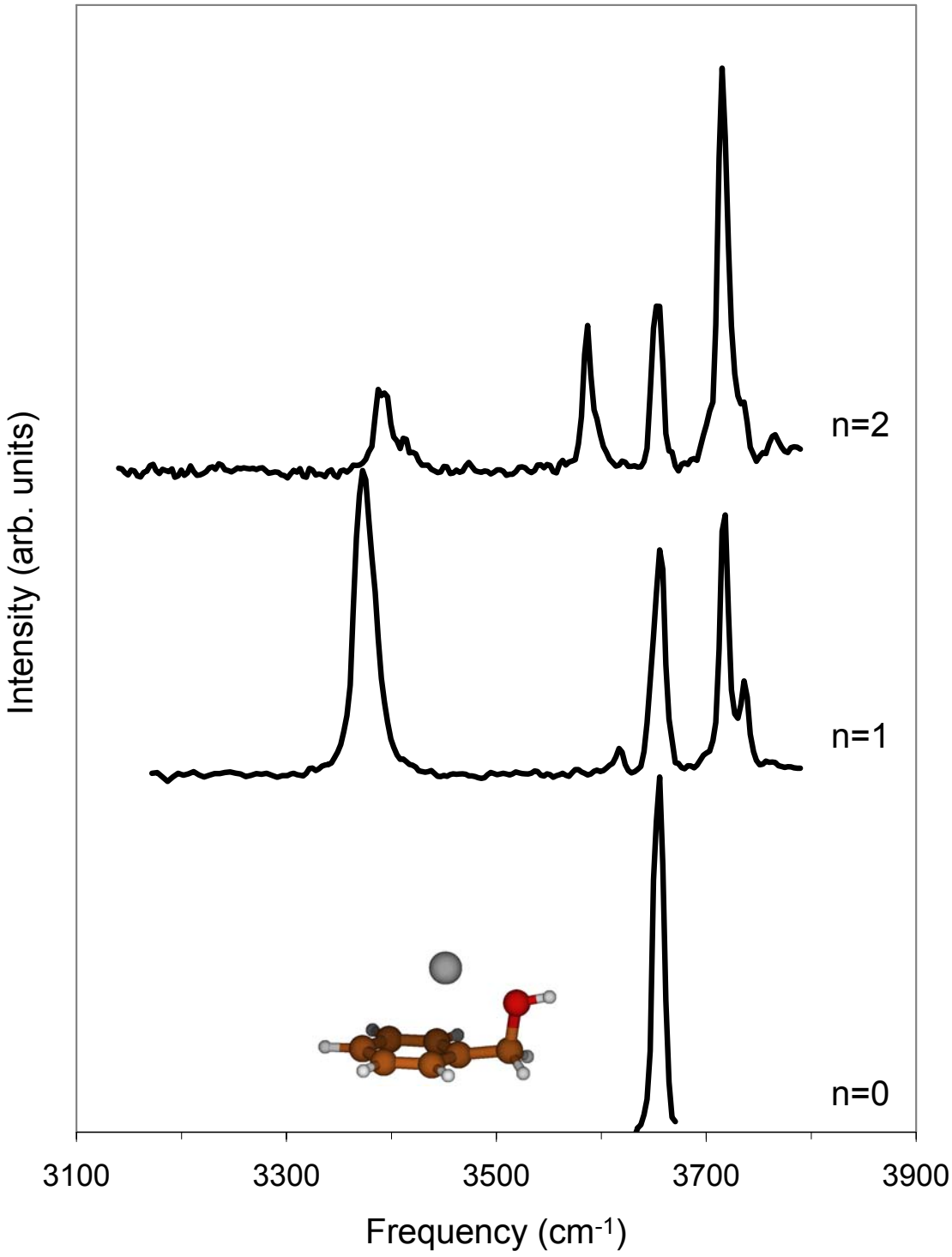

Figure 6.5. IRPD spectra of $Na^+(BA)_1(H_2O)_nAr$. The calculated global minimum energy conformer of $Na^+(BA)_1Ar$ is also shown.

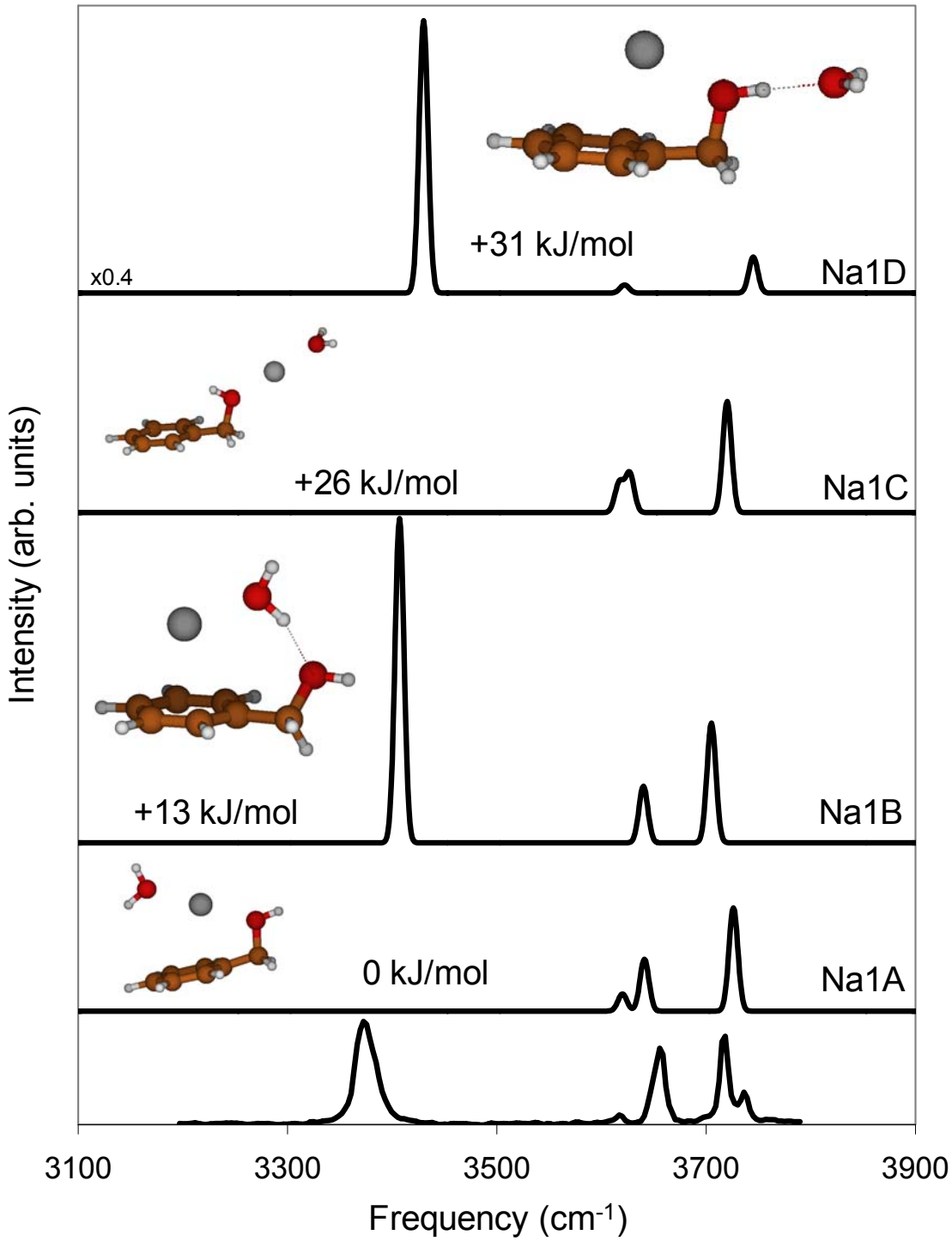

Figure 6.6. Experimental IRPD spectrum of $Na^+(BA)_1(H_2O)_1Ar$ (bottom) along with four optimized MP2/6-31+G* calculated structures and simulated spectra.

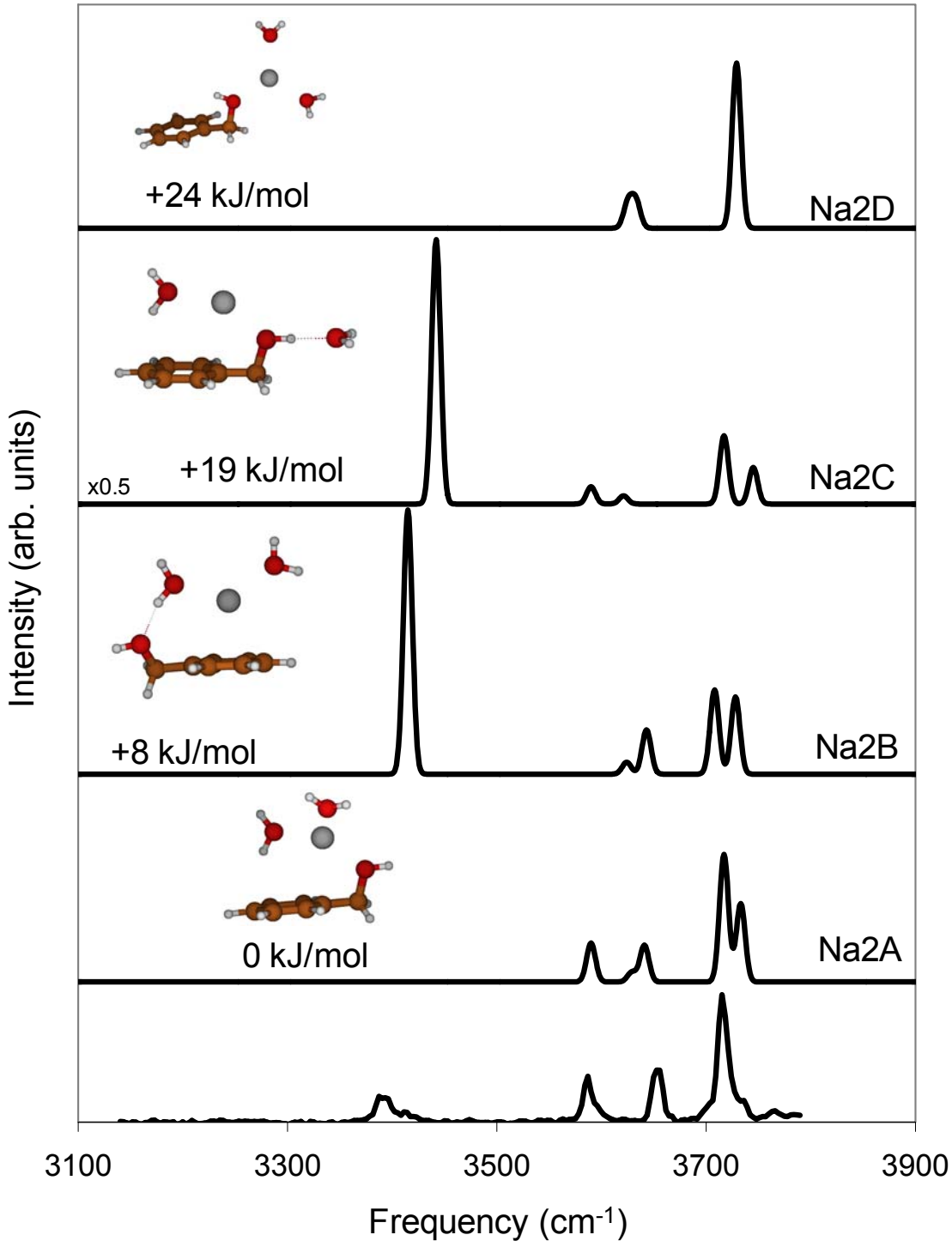

Figure 6.7. Experimental IRPD spectrum of $Na^+(BA)_1(H_2O)_2Ar$ (bottom) along with four optimized MP2/6-31+G* calculated structures and simulated spectra.

6.6 Tables

Table 6.1. Calculated geometric parameters of selected $M^+(BA)_1(H_2O)_{0-2}$ clusters.

Distance(Å)	LiBA	NaBA	Li1A	Na1A	Li2A	Na2A
Ion-O (BA)	1.91	2.32	1.90	2.32	1.91	2.32
Ion-C_{ipso} [a]	2.29	2.66	2.44	2.73	3.01	3.06
Ion-X [b]	2.53	2.76	2.85	2.93	3.58	3.46
H-C_n [c]			2.80	3.38	2.44	2.53
Angle (degree)	**LiBA**	**NaBA**	**Li1A**	**Na1A**	**Li2A**	**Na2A**
Ion-C_{ipso}-X [b]	83	79	92	84	102	95
O-H-C_n [c]			131	113	154	148

[a] C_{ipso} represents the benzyl alcohol ring carbon onto which the CH_2OH substituent is attached. See Figure 6.1.

[b] X represents the center of mass of the six carbon atoms that constitute the ring in benzyl alcohol.

[c] H-C_n represents the distance between a water hydrogen and the nearest carbon atom. O-H-C_n is the angle formed from the water oxygen through the hydrogen to that nearest carbon.

6.7 References

(1) *Hydrogen Bonding - New Insights*; Grabowski, S. J., Ed.; Springer: Dordrecht, The Netherlands, 2006; Vol. 3.

(2) Marechal, Y. *The Hydrogen Bond and the Water Molecule*, 1 ed.; Elsevier: Amsterdam, 2007.

(3) Nelson, D. L.; Cox, N. M. *Lehninger Principles of Biochemistry*, 3rd ed.; Worth Publishers: New York, NY, 2000.

(4) Hartung, W. H. *Chemical Reviews* 1931, *9*, 389.

(5) Lands, A. M.; Arnold, A.; McAuliff, J. P.; Luduena, F. P.; Brown Jr, T. G. *Nature* 1967, *214*, 597.

(6) Miller, D. J.; Lisy, J. M. *The Journal of Chemical Physics* 2006, *124*, 184301.

(7) Nicely, A. L. Charge and temperature effects on biomolecule hydration: An experimental and computational investigation, University of Illinois at Urbana-Champaign, 2010.

(8) Nicely, A. L.; Miller, D. J.; Lisy, J. M. *Journal of the American Chemical Society* 2009, *131*, 6314.

(9) Vaden, T. D.; Lisy, J. M. *Journal of Chemical Physics* 2004, *120*, 721.

(10) Vaden, T. D.; Lisy, J. M. *Journal of Chemical Physics* 2005, *123*.

(11) Vaden, T. D.; Lisy, J. M. *Journal of Chemical Physics* 2006, *124*.

(12) Faubel, M.; Steiner, B.; Toennies, J. P. *Journal of Chemical Physics* 1997, *106*, 9013.

(13) Guchhait, N.; Ebata, T.; Mikami, N. *Journal of the American Chemical Society* 1999, *121*, 5705.

(14) Im, H. S.; Bernstein, E. R.; Secor, H. V.; Seeman, J. I. *Journal of the American Chemical Society* 1991, *113*, 4422.
(15) Ito, M.; Hirota, M. *Bulletin of the Chemical Society of Japan* 1981, *54*, 2093.
(16) Schaefer, T.; Sebastian, R.; Peeling, J.; Penner, G. H.; Koh, K. *Canadian Journal of Chemistry* 1989, *67*, 1015.
(17) Varfolomeeva, V. V.; Terent'ev, V. A. *Russian Journal of General Chemistry* 1998, *68*, 1914.
(18) Visser, T.; Van Der Maas, J. H. *Spectrochimica Acta Part A: Molecular Spectroscopy* 1986, *42*, 599.
(19) Ahn, D. S.; Jeon, I. S.; Jang, S. H.; Park, S. W.; Lee, S.; Cheong, W. *Bulletin of the Korean Chemical Society* 2003, *24*, 695.
(20) Dessent, C. E. H.; Geppert, W. D.; Ullrich, S.; Moller-Dethlefs, K. *Chemical Physics Letters* 2000, *319*, 375.
(21) Glaser, R.; Nichols, G. R. *Journal of Organic Chemistry* 2000, *65*, 755.
(22) Guchhait, N. *Proceedings of the Indian Academy of Sciences: Chemical Sciences* 2001, *113*, 235.
(23) Guchhait, N.; Ebata, T.; Mikami, N. *Journal of Chemical Physics* 1999, *111*, 8438.
(24) Li, S.; Bernstein, E. R. *The Journal of Chemical Physics* 1992, *97*, 7383.
(25) Miller, B. J.; Kjaergaard, H. G.; Hattori, K.; Ishiuchi, S. i.; Fujii, M. *Chemical Physics Letters* 2008, *466*, 21.
(26) Mons, M.; Robertson, E. G.; Simons, J. P. *Journal of Physical Chemistry A* 2000, *104*, 1430.
(27) Sebbar, N.; Bockhorn, H.; Bozzelli, J. W. *Journal of Physical Chemistry A* 2005, *109*, 2233.
(28) Utzat, K.; Restrepo, A. A.; Bohn, R. K.; Michels, H. H. *International Journal of Quantum Chemistry* 2004, *100*, 964.
(29) Utzat, K. A.; Bohn, R. K.; Montgomery, J. A.; Michels, H. H.; Caminati, W. *Journal of Physical Chemistry A* 2010, *114*, 6913.
(30) Abraham, R. J.; Bakke, J. M. *Tetrahedron* 1978, *34*, 2947.
(31) Baker, A. W.; Bublitz, D. E. *Spectrochimica Acta* 1966, *22*, 1787.
(32) Hehre, W. J.; Radom, L.; Pople, J. A. *Journal of the American Chemical Society* 1972, *94*, 1496.
(33) Oki, M.; Iwamura, H. *Bulletin of the Chemical Society of Japan* 1959, *32*, 955.
(34) Oki, M.; Iwamura, H. *Bulletin of the Chemical Society of Japan* 1959, *32*, 1135.
(35) Wavefunction, I. Spartan '08 Irvine, CA.
(36) Frisch, M. J. T., G. W.; Schlegel, H. B.; Scuseria, G. E. et. al., Gaussian 03, Revision D.01; Gaussian, Inc.: Wallingford CT, 2004.
(37) Gorelsky, S. I. *SWizard program*; 4.1 ed., 2005.

Chapter 7: Infrared Spectroscopy of Hydrated Alkali Metal Cations: Evidence of Multiple Photon Absorption

7.1 Introduction

Cluster ions are stabilized by non-covalent interactions and can be induced to fragment with vibrational excitation. It has long been known that when the binding energy of the most labile ligand of a cluster ion is less than the energy of a resonant infrared (IR) photon, then single photon absorption is sufficient to cause fragmentation. However, cluster fragmentation has been reported in cases where the binding energy of the dissociating ligand exceeds the energy of a single IR photon. This seemingly counterintuitive situation has led to some confusion and debate in the literature.

Yuan T. Lee and his group were the first to try to explain this phenomena in a manner that was a natural progression from work in infrared multiple photon dissociation (IRMPD)[1]. One of the major results from the IRMPD field was to prove that once a molecule or ion is in a quasi-continuum (i.e. in a region of very high density of states) the energy fluence, not the laser power, dictates the extent of fragmentation[2,3]. Lee and co-workers exploited this knowledge to develop a two-color laser scheme to dissociate strongly bound cluster ions. Either a tunable difference frequency generation (DFG) laser with ~10 ns/pulse and ~1 mJ/pulse[4,5] or a tunable cw color center laser[6] was used to resonantly excite a vibrational stretching mode of the cluster. Irradiation with a fixed frequency, 2-10 W cw-CO_2 laser for tens of milliseconds was used to selectively dissociate the vibrationally excited clusters, which had a much higher density of states than the ground state clusters. This technique was successfully applied to several

systems, including $H_3O^+(H_2O)^6$, which has a binding energy of over 132 kJ/mol (11,000 cm^{-1}).

Other experiments, using only a single, tunable DFG laser pulse, suggested that MPD was still the primary route to dissociation[4-7] as in the cases of $H_3O^+(H_2O)_{2-3}$[6] and $NH_4^+(NH_3)_{3-10}$[4,7]. This was a very logical assumption for the smallest clusters, where the binding energies reached 82 kJ/mol (6900 cm^{-1}), which is equivalent to approximately two mid IR photons. The exception to this generalization was $C_2H_7^+$, with a binding energy of 54 kJ/mol (4500 cm^{-1})[5]. Since the binding energy was only slightly larger than the photon energy (3650-3950 cm^{-1}), the authors noted that the cluster ions with an internal energy of 8-10 kJ/mol (700-800 cm^{-1}), corresponding to a temperature of 400-500 K, could fragment following the absorption of a single photon. Thus, the internal energy of the absorbing cluster ions was also seen to be an important factor.

Subsequently, two papers, one by the group of Okumura[8] and one by Lee's group (led primarily by Chang by that time)[9], showed that $NO^+(H_2O)_2$ and $NH_4^+(H_2O)_3$ with hydration enthalpies of 67 kJ/mol (5600 cm^{-1}) and 56 kJ/mol (4700 cm^{-1}), respectively, could each dissociate after absorption of a single photon in the range 3300-3800 cm^{-1} at the expense of some internal energy. These papers led to somewhat of a paradigm shift in the discussion of how the dissociation of tightly bound cluster ions took place, with many more recent papers stating that dissociation results from the combined contributions of internal energy and single photon absorption[10-25].

However, this does not rule out the possibility of multiple photon absorption from a single laser pulse. Depending on the size, ligand binding energies, and internal energy of the clusters studied, two photon absorption can occur[8,26,27]. The mechanism used to

explain the absorption of several photons in these studies is once again borrowed from the extensive literature on IRMPD[28]. After a single photon absorption and subsequent rapid intramolecular vibrational redistribution (IVR), the cluster is able to absorb a second photon with the same vibrational mode responsible for both absorption events. This is the same incoherent photon absorption mechanism responsible for IRMPD of strongly bound molecules where tens to hundreds of photons are required for dissociation, often accomplished with CO_2[29]or free-electron[30-36] lasers. In single DFG laser pulse experiments, this mechanism has been used to explain the absence of the asymmetric (υ_3) H_2O stretch in the spectrum of $NO^+(H_2O)$ even though the symmetric (υ_1) is observed[8] as well as the absence of the free OH stretch in $Cl^-(H_2O)$[26]. These studies emphasize the importance of efficient IVR when this multiple photon absorption mechanism is operative.

Evidence will be presented in this paper for the absorption of multiple photons by hydrated alkali metal ion clusters based on changes in spectral features in various cluster fragmentation channels. Several groups have reported the detection of various fragment cluster ions from similar systems by irradiating them with a single pulse[8,37,38] or multiple pulses[39,40] of a mid IR DFG laser. However, a systematic investigation of the implications of multiple IR photon absorption and subsequent dissociation of weakly bound cluster ions of this type into different fragmentation channels has yet to be published.

7.2 Experimental Details

The spectra presented in this chpater were acquired using the triple-quadrupole mass spectrometer and IR laser which was described in chapter 2. A brief description is

given here. A mixture of argon and water (~ 100:1) is supersonically expanded through a 180 μm diameter conical nozzle with typical backing pressures of 300-500 Torr to generate neutral water clusters. The fully expanded neutral beam is subsequently impacted perpendicularly by ions produced by thermionic emission. The nascent cluster ions have a large amount of internal energy from the collisional impact of the ion and its subsequent solvation, which is dissipated via evaporative cooling until the clusters reach a quasi-stable state. The ions are guided into the detection chamber which consists of three quadrupoles and the detector. The first quadrupole mass-selects the parent ion of interest. The second quadrupole serves as an ion guide with no ion trapping implemented. While traversing this quadrupole, the ions interact with a single, ~ 10 ns pulse from a mildly-focused, tunable IR laser (LaserVision OPO/A pumped by a 10 Hz Surelite II Nd:YAG laser). Typical IR energies in the quadrupole range from 1-8 mJ/pulse with a spot size ~ 2.1 mm. Photon absorption induces dissociation and the third quadruple mass-selects the resulting fragment ions. Fluence-corrected dissociation cross-sections are reported as a function of IR frequency while monitoring various fragment ions.

7.3 Results

A compilation of the IRPD spectra in the OH stretching region for the one- and two-water-loss channels of $M^+(H_2O)_{5-7}$, where M is an alkali metal, is shown in Figure 7.1. The spectra are organized into columns where all the clusters share similar spectral features. To facilitate comparison between the one- and two-water-loss spectra, the spectra have been scaled so that the high frequency feature (~ 3710-3720 cm^{-1}) in each panel has the same maximum value. We first consider $Cs^+(H_2O)_5$, where the one-water-

loss spectrum with five absorption features has been assigned in a previous study[22]. The peak at 3710 cm^{-1} has two contributions: the asymmetric and free-OH stretching modes. The symmetric stretch of water gives rise to the weak peak at 3645 cm^{-1}. The features below 3600 cm^{-1} correspond to hydrogen-bonded OH stretches from isomers with various water•••water interactions. These are bent (~ 3570 cm^{-1}), linear (~ 3490 cm^{-1}), and cyclic (~ 3415 cm^{-1}) hydrogen bonds, as shown in Figure 7.2.

The two-water-loss spectrum of $Cs^+(H_2O)_5$ is dramatically different compared to the one-water-loss counterpart. Features from the bent and cyclic hydrogen bond OH stretches are appreciably suppressed in the two-water-loss case. Essentially the same results are observed for $Li^+(H_2O)_6$, $Na^+(H_2O)_6$, $K^+(H_2O)_6$, and $Rb^+(H_2O)_5$ (left column of Figure 7.1). Furthermore, the features from the free OH and linear H-bond OH stretches are relatively unaffected by the loss channel monitored in all cases. It is clear that the process responsible for the loss of multiple ligands in our experiments is strongly mode-dependent.

As more solvating waters are added to the clusters, the strength of ion•••ligand interactions decrease and water•••water interactions begin to dominate. This shift can be seen in the one-water-loss spectra of $Li^+(H_2O)_7$, $Na^+(H_2O)_7$, $K^+(H_2O)_7$, and $Rb^+(H_2O)_6$ (right column of Figure 7.1) by an increase in the cyclic feature at 3400-3415 cm^{-1} relative to the linear and bent hydrogen-bonded features. This suggests that cluster ions with more extensive hydrogen-bonded networks are prevalent in these larger systems. Despite the prominence of the cyclic-type feature in the one-water-loss spectra, the two-water-loss spectra still reflect a strong preference for the linear hydrogen bond in the

3450-3500 cm^{-1} region, while the bent hydrogen bond and cyclic hydrogen bond OH stretching features are significantly suppressed.

The spectra of $Na^+(H_2O)_5$, $K^+(H_2O)_5$, and $Cs^+(H_2O)_4$, not shown, further emphasize the mode-specific nature of the multiple ligand loss process. For these clusters, the one-water-loss spectra contain only two prominent hydrogen-bonded OH stretching features, corresponding to bent and linear type hydrogen bonds. In the two-water-loss spectra, the peak from the linear hydrogen bond OH stretch retains its intensity while the peak corresponding to a bent hydrogen bond OH stretch is not observed.

7.4 Discussion

A significant issue to address is whether the two-water spectra are the result of multiple photon absorption or whether they are from one photon absorption of clusters with sufficient internal energy to dissociate two water molecules. We took several approaches to answer this question. The first was to investigate the fluence dependence of both the one- and two-water-loss spectra. The slope of a ln-ln plot of fragmentation vs. laser pulse energy gives an indication of the number of photons absorbed[2,8,13]. An example of the fluence analysis for the linear hydrogen bond OH stretching feature of $Li^+(H_2O)_7$ is shown in panel A of Figure 7.3, where a ln-ln plot of fragmentation vs. laser pulse energy shows a linear relationship with a slope of 0.83±0.03 for the loss of one water and 1.80±0.07 for the loss of two waters. Similar plots were generated for many of the clusters in the linear hydrogen bond OH stretching region and are summarized in panel B of Figure 7.3. The one water loss data are centered around 0.8, indicating a linear, one photon process. However, the two water loss data show a slope that is

uniformly larger than one and centered around 1.75, indicating significant quadratic, two-photon contributions.

Next, as emphasized in the introduction, when distinguishing between single and multiple photon dissociation, it is important to consider the internal energy of the clusters. Thus, our second approach to determine the number of photons required to dissociate two ligands was to compare the experimental extent of fragmentation with the amount predicted by modeling our experiments using the Rice-Ramsperger-Kassel-Marcus evaporative ensemble (RRKM-EE) formalism, which allows the energy distribution of evaporating clusters to be calculated and tracked as a function of flight time through the apparatus. This approach has been described in detail previously[41] and is also described in chapter 8. A full set of calculations was performed for $Li^+(H_2O)_7$. Experimentally, 15% of the parent clusters lost two waters at 3460 cm^{-1}. The results of the simulations for two photon absorption are shown in Figure 7.4 and the overall results are summarized in Table 7.1. The results indicate that the energy provided by one mid-IR photon is not sufficient to lead to dissociation of two water ligands even from the hottest $Li^+(H_2O)_7$ cluster ions. Based on the calculations, if two 3460 cm^{-1} photons are absorbed by a $Li^+(H_2O)_7$ cluster ion, there is a 40% probability that the cluster ion would dissociate with the loss of two waters. Therefore, the experimental fragmentation of 15% could be explained if roughly 40% of the $Li^+(H_2O)_7$ clusters absorbed two photons, resulting in an overall two water fragmentation of 16%. This is a general result that the amount of fragmentation observed in the multiple-water loss spectra exceeds that expected from single photon absorption based on RRKM-EE calculations, but can be explained by invoking multiple photon absorption.

A final piece of evidence of multiple photon absorption is provided by the $Na^+(H_2O)_7$ spectra shown in Figure 7.5. For this cluster, in addition to the one- and two-water loss spectra shown in Figure 7.1, a spectrum was obtained by monitoring the three-water-loss channel. At 3720 cm^{-1}, approximately 2% of the parent clusters lost three water ligands. Since the binding energy of each water is at least 40 kJ/mol[42], the energy required to dissociate three waters from $Na^+(H_2O)_7$ cannot be provided by a single photon.

The next issue that must be addressed is the preponderance of the free-OH and linear hydrogen bond peaks in the multiple-water-loss spectra. Since we just have shown that the two-water-loss spectra come primarily from two-photon absorption, it is reasonable to assume that the differences between the one- and two-water-loss spectra come from differences in the one- and two-photon absorption processes. One common multiple photon absorption mechanism which is known to occur in molecular and cluster ions is the 'slow-heating', incoherent absorption of multiple photons, mentioned in the introduction. This is a multiple step mechanism consisting of photon absorption followed by rapid IVR and subsequent absorption of another photon by the same 'bright' mode. For single laser pulse (~10 ns) experiments, this mechanism relies on efficient redistribution of energy to prepare the absorbing chromophore for another absorption event and therefore favors vibrational modes with the most rapid IVR. Thus, as seen in $Cl^-(H_2O)$[26], for single laser pulse experiments, hydrogen bonded OH stretches, which have stronger anharmonic couplings to the low frequency cluster modes, are more susceptible to this mechanism than are the relatively decoupled free-OH stretches. This multiple photon absorption mechanism seems inconsistent with the experimental spectra

shown in Figure 7.1. In each of the two-water-loss spectra, the free-OH stretching feature retains significant intensity, an unexpected result based on IVR propensities. Furthermore, the incoherent two-photon mechanism cannot be used to explain the drastic differences in the relative intensities of the cyclic, linear, and bent type hydrogen bonded OH stretching features. The cyclic hydrogen bond OH stretch is part of an extensive H-bond network, so it would be expected to have the most rapid IVR and be most susceptible to this MPA process. However, this is not the case in our experiments. Only the linear hydrogen bonded OH stretch retains significant intensity in the hydrogen bond region in the two water loss spectra.

Another possible MPA/D mechanism that has been suggested is as follows:

$$M^+(H_2O)_n \xrightarrow{h\nu} M^+(H_2O)_{n-1} + H_2O$$
$$M^+(H_2O)_{n-1} \xrightarrow{h\nu} M^+(H_2O)_{n-2} + H_2O$$

In this scenario, the parent cluster absorbs a photon and dissociates. Then, the fragment ion absorbs a photon and subsequently dissociates. The main argument against this mechanism for our experiments is that it would require that the parent ion dissociate within 10 ns in order for the first fragment ion to have a chance to interact with the laser pulse. According to our RRKM-EE calculations, the $Li^+(H_2O)_7$ ensemble after one photon absorption has a median dissociation lifetime of 650 ns. Furthermore, if one considers only the top 5% of clusters with internal energy, the average lifetime is 30 ns, still above the 10 ns threshold. The results from $Li^+(H_2O)_7$ RRKM-EE calculations are readily generalized to the other clusters and indicate that the parent clusters do not contain sufficient internal energy to dissociate within the 10 ns time frame required for this particular mechanism.

Another suggested mechanism is coherent two photon absorption or a ladder climbing mechanism[1,43]. Given that all vibrational modes are anharmonic to some extent, for direct two-photon absorption to occur, some form of anharmonic compensation must take place. A common method is to use very intense lasers (10^7-10^9 W/cm^2) so that the laser field broadening can compensate for the anharmonicity[1,43]. Using much more moderate intensities of ~ 10^5 W/cm^2, molecules such as SF_6 were shown to undergo two-photon absorptions by rotational anharmonicity compensation (PQR-transitions)[44]. However, the anharmonicities of the water molecule are significantly larger than the anharmonicities of SF_6[45]. With anharmonicity constants of x_{11} = -44 cm^{-1} and x_{33} = -46 cm^{-1}, the v = 1 to v = 2 transitions of the symmetric and asymmetric water stretches are off resonance from the fundamentals by around 90 cm^{-1}. Although the exact frequencies of the cluster water modes will be slightly different, similarly large anharmonicites are still present with the hydrogen bonded OH stretching modes and the free OH stretching modes. Thus, with such large anharmonicities and with the very modest ~ 3MW/cm^2 laser intensity used in our experiments, direct two-photon absorption through laser power broadening or rotational compensation seems very unlikely. It is still possible that anharmonic compensation occurs through other means, for example through a combination band. Choi et. al. have suggested that two photon absorption in $NO^+(H_2O)$ could occur through the $0 \rightarrow \upsilon_1 \rightarrow \upsilon_1 + \upsilon_3$ combination band[8]. However, the $\upsilon_1 \rightarrow \upsilon_1 + \upsilon_3$ transition for water is still off resonance from the υ_1 fundamental by 57 cm^{-1}. Even allowing for the potential influence of factors like combination bands, another practical argument against this mechanism of MPA is that it cannot be used to explain the observed experimental spectra. There appears to be no mechanism that would provide an

efficient route to direct two-photon absorption using the ladder climbing mechanism selectively for the linear hydrogen-bonded OH and free OH stretches, but not for the bent and cyclic bonded OH stretches.

Given the apparent failure of the suggested MPA mechanisms given above, we propose another possible MPA mechanism which is consistent with our experimental data. It is possible that degenerate oscillators in the cluster can individually absorb a photon during the laser pulse. In order for this to occur, the multiple absorbing oscillators must be decoupled from one another. Thus for multiple photon absorption to occur, an oscillator must be able to absorb a photon without significantly changing the absorption cross section or frequency of the other degenerate oscillators over the timescale of the experiment; in this case the ~10 ns laser pulse. Thus, clusters with decoupled oscillators would be the most likely candidates for MPA. Clearly, the free-OH stretching mode is less coupled than an OH involved in a proton-donating hydrogen bond[46]. So, clusters with multiple free-OH oscillators should be susceptible to this MPA mechanism at ~3710 cm^{-1} as observed in Figure 7.1. The situation is somewhat more complicated in the hydrogen bonding region because the oscillators are not necessarily independent of one another. Consider three isomers (shown in Figure 7.2) of $Cs^+(H_2O)_5$ that have been shown to be present under our experimental molecular beam conditions[22]. The isomer in Figure 7.2A contains a ring of four hydrogen bonds. The dynamics of ring opening following IR excitation in hydrogen bonded systems has been studied previously. For example, two reports on the hydrogen fluoride trimer agreed that ring opening occurred on the picosecond time scale[47,48]. In a similar way, a single photon absorption by the cluster represented in Figure 7.2A could cause rapid hydrogen bond

cleavage and subsequent ring opening. This ring opening, on a timescale much shorter than the laser pulse width, would preclude subsequent absorption of photons in the cyclic hydrogen bond spectral region and thus lead to diminished MPA in the multiple water loss channel. The isomer represented in Figure 7.2B contains two bent hydrogen bonds in a cyclic-like structure with the ion. The bent hydrogen bonds are not independent of each other. A single photon absorption in the bent region could lead to the rapid cleavage of one of these hydrogen bonds, disrupting the bent system on a timescale much shorter that the laser pulse width. This leaves the remaining isomer in Figure 7.2C to consider as a candidate for MPA in the H-bond region. In contrast to the other two isomers, this isomer has two identical linear hydrogen bonds which are independent of each other. Either could conceivably absorb a photon during the 10 ns laser pulse without leading to the dissociation or perturbation of the other. Thus, of the three isomers presented, the one with the linear hydrogen bonds would be predicted to be most susceptible to MPA. This is a rational explanation for the one feature in the hydrogen bond region that retains significant intensity in the multiple ligand loss channels. Due to its consistency with our experiments and explanatory power, we therefore propose that the MPA process in our experiments involves the parallel excitation of multiple, identical, and independent oscillators, where each oscillator is able to absorb a photon independent of the others.

7.5 Conclusions

Mode-specific behavior was observed by monitoring multiple loss channels of $M^+(H_2O)_n$ clusters after irradiation with a single, ~10 ns pulse from a YAG pumped, OPO/OPA laser system. The two-water-loss spectra of $M^+(H_2O)_{5\text{-}7}$ show a preference for free-OH and linear hydrogen bond OH stretching features, whereas the cyclic- and bent-

type hydrogen bonded OH stretching features are significantly suppressed or unobserved. Based on simulations of the internal energy distributions of these clusters, evidence was given that the two-water-loss spectra are primarily the result of two-photon absorption. The MPA mechanism used to explain the experimental results is the parallel excitation of multiple, identical oscillators. Free OH and linear hydrogen bond oscillators are relatively decoupled from each other and multiple oscillators can independently absorb a photon. Bent- and cyclic-type hydrogen bonds are not susceptible to parallel multiple photon absorption, due to rapid hydrogen bond cleavage and ring opening processes, which are fast compared to the timescale of the experiment.

7.6 Figures

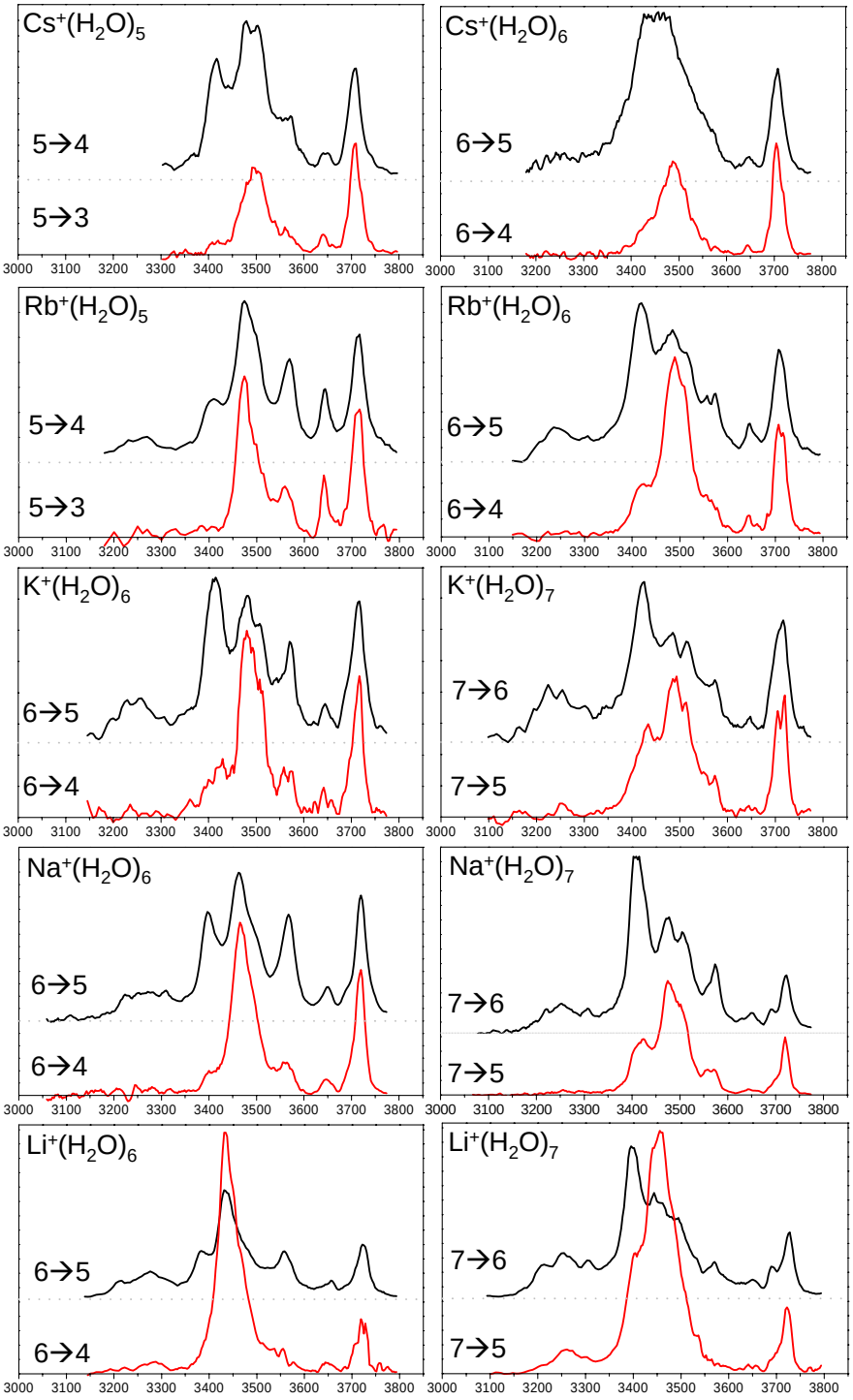

Figure 7.1. Summary of IRPD spectra of $M^+(H_2O)_{5\text{-}7}$ monitoring the loss of one water (black) and two waters (red). Graph axes are frequency in cm^{-1} (x-axis) and dissociation cross section in arbitrary units (y-axis). Cross sections for each cluster are scaled so that each loss channel has the same maximum of the free-OH peak at ~3710-3720 cm^{-1}.

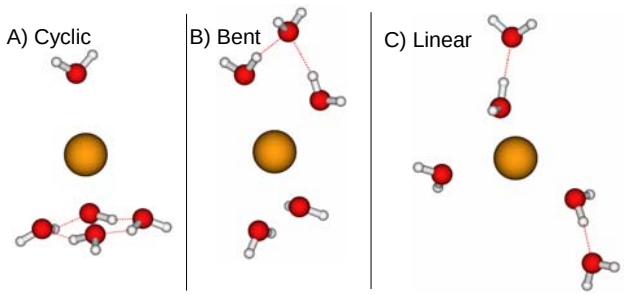

Figure 7.2. Three isomers of $Cs^+(H_2O)_5$ that are likely present in our molecular beam containing A) cyclic, B) bent, and C) linear type hydrogen bonds. Figures taken from Miller, et. al[22].

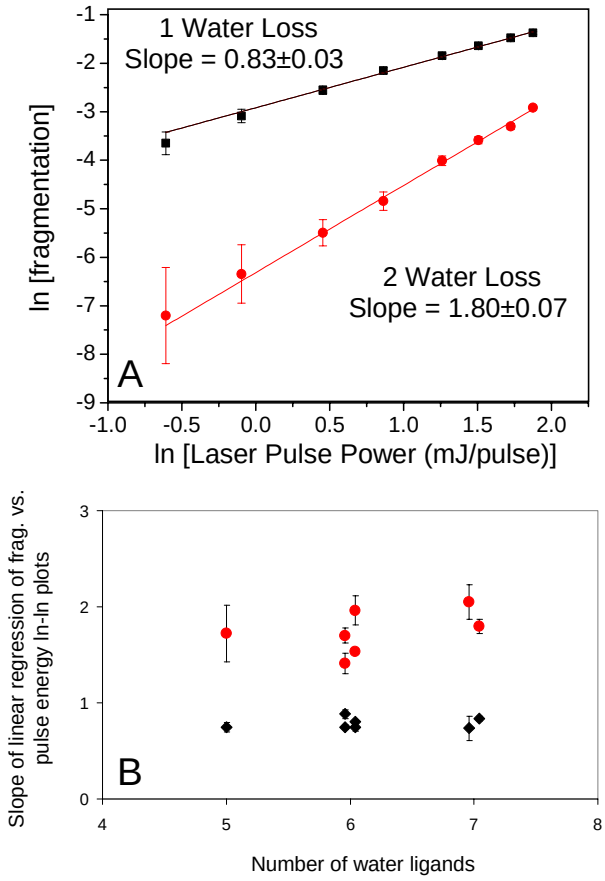

Figure 7.3. Panel A: Laser power dependence of the fragmentation channels of $Li^+(H_2O)_7$ observed at 3460 cm^{-1}. Experimental data for 1 water loss (black squares) and 2 water loss (red circles) are plotted in a ln-ln plot along with the linear regression line for each set of data. Panel B: Experimental laser power dependence data for the loss of one water (black diamonds) and the loss of two waters (red circles). The x-axis is the number of water ligands in $M^+(H_2O)_n$ (for n=6,7, slight offsets are used for better visualization) and the y-axis is the linear least-squares regression slope from a ln-ln plot of fragmentation vs. laser pulse power.

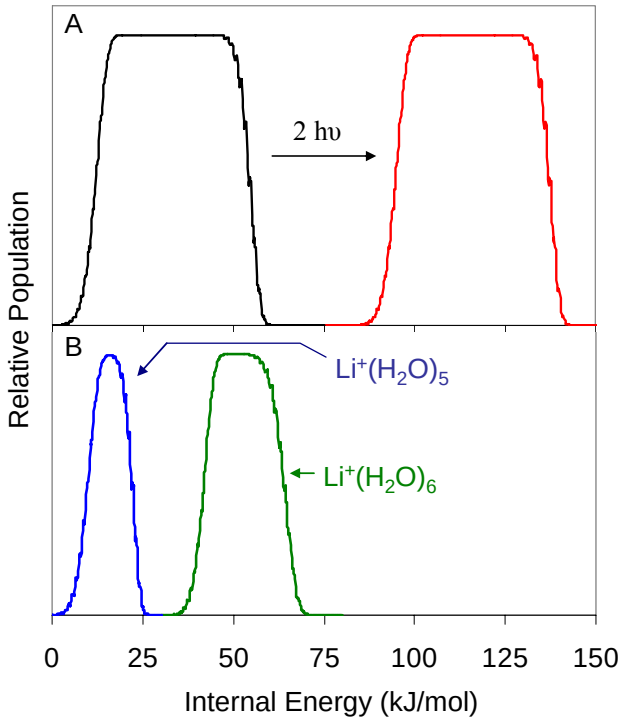

Figure 7.4. Energy distributions calculated using the RRKM-EE approach. Panel A Energy distribution calculated for the parent ion $Li^+(H_2O)_7$ in the middle of the second quadrupole before (black) and after (red) the absorption of 2 photons at 3460 cm^{-1}. Panel B: Energy distributions calculated for the fragment ions at the detector produced by fragmentation from 2-photon-excited $Li^+(H_2O)_7$ parent ions. According to these calculations, ~ 40% of the 2-photon-excited $Li^+(H_2O)_7$ parent ions end up in the two-water-loss fragmentation channel.

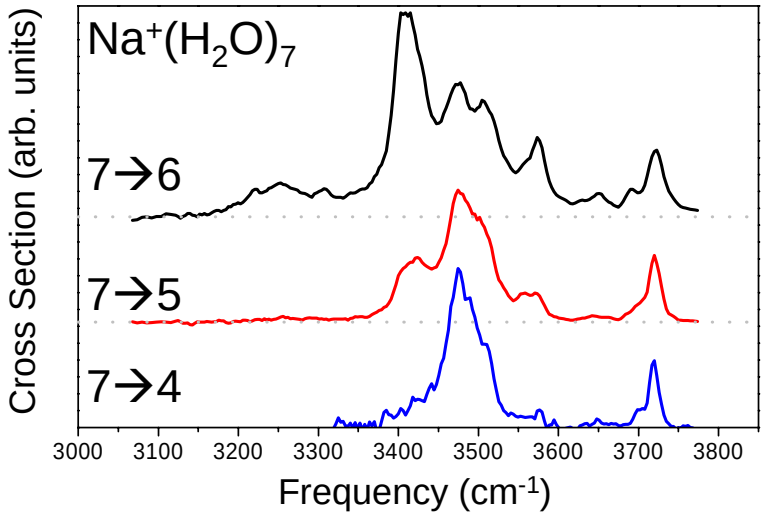

Figure 7.5. IRPD spectra of $Na^+(H_2O)_7$ monitoring the loss of one water (black), two waters (red), and three waters (blue). Cross sections are scaled so that each loss channel has the same maximum of the free-OH peak.

7.7 Tables

Table 7.1. Probability that a $Li^+(H_2O)_7$ cluster will lose 0,1, or 2 water ligands as the result of one or two photon (3460 cm^{-1}) absorption based on RRKM-EE calculations. Uncertainties (given in parentheses) estimated by varying the water binding energies used in the RRKM calculations by ± 10%.

	1 photon	2 photons
No frag.	0.1 (0.1)	0.0 (0.0)
-1 Water	0.9 (0.1)	0.6 (0.2)
-2 Waters	0.0 (0.0)	0.4 (0.2)

7.8 References

(1) Schulz, P. A.; Sudbø, A. S.; Krajnovich, D. J.; Kwok, H. S.; Shen, Y. R.; Lee, Y. T. *Annual Review of Physical Chemistry* 1979, *30*, 379.

(2) Bomse, D. S.; Woodin, R. L.; Beauchamp, J. L. Multiphoton Dissociation of Molecules with Low Power CW Infrared Lasers. In *Advances in Laser Chemistry*; Zewail, A. H., Ed.; Springer: New York, 1978; Vol. 3; pp 362.

(3) Woodin, R. L.; Bomse, D. S.; Beauchamp, J. L. *Journal of the American Chemical Society* 1978, *100*, 3248.

(4) Price, J. M.; Crofton, M. W.; Lee, Y. T. *Journal of Physical Chemistry* 1991, *95*, 2182.

(5) Yeh, L. I.; Price, J. M.; Lee, Y. T. *J. Am. Chem. Soc.* 1989, *111*, 5597.

(6) Yeh, L. I.; Okumura, M.; Myers, J. D.; Price, J. M.; Lee, Y. T. *Journal of Chemical Physics* 1989, *91*, 7319.
(7) Price, J. M.; Crofton, M. W.; Lee, Y. T. *The Journal of Chemical Physics* 1989, *91*, 2749.
(8) Choi, J.-H.; Kuwata, K. T.; Haas, B.-M.; Cao, Y.; Johnson, M. S.; Okumura, M. *The Journal of Chemical Physics* 1994, *100*, 7153.
(9) Wang, Y.-S.; Chang, H.-C.; Jiang, J.-C.; Lin, S. H.; Lee, Y. T.; Chang, H.-C. *Journal of the American Chemical Society* 1998, *120*, 8777.
(10) Chang, H.-C.; Jiang, J.-C.; Hahndorf, I.; Lin, S. H.; Lee, Y. T.; Chang, H.-C. *Journal of the American Chemical Society* 1999, *121*, 4443.
(11) Chang, H.-C.; Wang, Y.-S.; Lee, Y. T.; Chang, H.-C. *International Journal of Mass Spectrometry* 1998, *179-180*, 91.
(12) Hahndorf, I.; Jiang, J.-C.; Chang, H.-C.; Wu, C.-C.; Chang, H.-C. *The Journal of Physical Chemistry A* 1999, *103*, 8753.
(13) Inokuchi, Y.; Nishi, N. *The Journal of Chemical Physics* 2001, *114*, 7059.
(14) Inokuchi, Y.; Ohashi, K.; Honkawa, Y.; Yamamoto, N.; Sekiya, H.; Nishi, N. *The Journal of Physical Chemistry A* 2003, *107*, 4230.
(15) Inokuchi, Y.; Ohshim, K.; Misaizu, F.; Nishi, N. *Journal of Physical Chemistry A* 2004, *108*, 5034.
(16) Jiang, J. C.; Wang, Y. S.; Chang, H. C.; Lin, S. H.; Lee, Y. T.; Niedner-Schatteburg, G.; Chang, H. C. *Journal of the American Chemical Society* 2000, *122*, 1398.
(17) Johnson, M. S.; Kuwata, K. T.; Wong, C. K.; Okumura, M. *Chemical Physics Letters* 1996, *260*, 551.
(18) Wang, Y. S.; Tsai, C. H.; Lee, Y. T.; Chang, H. C.; Jiang, J. C.; Asvany, O.; Schlemmer, S.; Gerlich, D. *The Journal of Physical Chemistry A* 2003, *107*, 4217.
(19) Weiser, P. S.; Wild, D. A.; Bieske, E. J. *Chemical Physics Letters* 1999, *299*, 303.
(20) Wu, C. C.; Jiang, J. C.; Boo, D. W.; Lin, S. H.; Lee, Y. T.; Chang, H. C. *The Journal of Chemical Physics* 2000, *112*, 176.
(21) Miller, D. J.; Lisy, J. M. *Journal of Chemical Physics* 2006, *124*, 1.
(22) Miller, D. J.; Lisy, J. M. *Journal of the American Chemical Society* 2008, *130*, 15393.
(23) Vaden, T. D.; Lisy, J. M. *Journal of Chemical Physics* 2005, *123*.
(24) Vaden, T. D.; Lisy, J. M. *Journal of Physical Chemistry A* 2005, *109*, 3880.
(25) Weinheimer, C. J.; Lisy, J. M. *Journal of Chemical Physics* 1996, *105*, 2938.
(26) Choi, J.-H.; Kuwata, K. T.; Cao, Y.-B.; Okumura, M. *Journal of Physical Chemistry A* 1998, *102*, 503.
(27) Pankewitz, T.; Lagutschenkov, A.; Niedner-Schatteburg, G.; Xantheas, S. S.; Lee, Y. T. *Journal of Chemical Physics* 2007, *126*.
(28) Letokhov, V. S. *Nonlinear Laser Chemistry. Multiple-Photon Excitation*Berlin, 1983; Vol. 22.
(29) Brodbelt, J. S.; Wilson, J. J. *Mass Spectrometry Reviews* 2009, *28*, 390.
(30) Eyler, J. R. *Mass Spectrometry Reviews* 2009, *28*, 448.
(31) MacAleese, L.; Maître, P. *Mass Spectrometry Reviews* 2007, *26*, 583.
(32) Oomens, J.; Sartakov, B. G.; Meijer, G.; von Helden, G. *International Journal of Mass Spectrometry* 2006, *254*, 1.

(33) Polfer, N. C.; Oomens, J. *Physical Chemistry Chemical Physics* 2007, *9*, 3804.
(34) Polfer, N. C.; Oomens, J. *Mass Spectrometry Reviews* 2009, *28*, 468.
(35) Valle, J. J.; Eyler, J. R.; Oomens, J.; Moore, D. T.; Meer, A. F. G. v. d.; Helden, G. v.; Meijer, G.; Hendrickson, C. L.; Marshall, A. G.; Blakney, G. T. *Review of Scientific Instruments* 2005, *76*, 023103.
(36) von Helden, G.; van Heijnsbergen, D.; Meijer, G. *The Journal of Physical Chemistry A* 2003, *107*, 1671.
(37) Miyazaki, M.; Fujii, A.; Ebata, T.; Mikami, N. *Science* 2004, *304*, 1134.
(38) Shin, J. W.; Hammer, N. I.; Diken, E. G.; Johnson, M. A.; Walters, R. S.; Jaeger, T. D.; Duncan, M. A.; Christie, R. A.; Jordan, K. D. *Science* 2004, *304*, 1137.
(39) Bush, M. F.; Saykally, R. J.; Williams, E. R. *ChemPhysChem* 2007, *8*, 2245.
(40) Bush, M. F.; Saykally, R. J.; Williams, E. R. *Journal of the American Chemical Society* 2008, *130*, 15482.
(41) Cabarcos, O. M.; Weinheimer, C. J.; Lisy, J. M. *J. Phys. Chem. A* 1999, *103*, 8777.
(42) Dzidic, I.; Kebarle, P. *The Journal of Physical Chemistry* 1970, *74*, 1466.
(43) Bagratashvili, V. N.; Letokhov, V. S.; Makarov, A. A.; Ryabov, E. A. *Multiple-photon Infrared laser Photophysics and Photochemistry*; Harwood Academic Publishers: Chur, Switzerland, 1985.
(44) Alimpiev, S. S.; Karlov, N. V.; Sartakov, B. G.; Khokhlov, E. M. *Optics Communications* 1978, *26*.
(45) Herzberg, G. *Molecular Spectra and Molecular Structure II. Infrared and Raman Spectra of Polyatomic Molecules*; Van Norstrand Reinhold Company: New York, New York, 1945.
(46) Pine, A. S.; Fraser, G. T. *The Journal of Chemical Physics* 1988, *89*, 6636.
(47) Michael, D. W.; Lisy, J. M. *The Journal of Chemical Physics* 1986, *85*, 2528.
(48) Suhm, M. A.; Farrell, J. T. J.; Ashworth, S. H.; Nesbitt, D. J. *The Journal of Chemical Physics* 1993, *98*, 5985.

Chapter 8: Evaporative Ensemble Calculations

8.1 Introduction

The internal energy content of cluster ions studied by IRPD spectroscopy is an important factor in determining cluster geometries and thus spectral features. Therefore, the Lisy group has a history of performing calculations to model the internal energy distributions of clusters studied in the triple quadruple apparatus described in chapter 2. The first generation of these energy modeling calculations utilized Rice-Ramsperger-Kassel[1,2] evaporative ensemble[3] (RRK-EE) formalism to calculate cluster energy distributions as a function of flight time through the apparatus in a two step process. The first step was to calculate unimolecular dissociation rates as a function of cluster internal energy. In the second step, the internal energy distributions were calculated using the assumptions of the evaporative ensemble and the dissociation rates as input parameters. These calculations were used to estimate average energies and temperatures for $M^+(CH_3OH)_n$ cluster ions[4,5].

The next generation of these calculations involved using the more rigorous Rice-Ramsperger-Kassel-Marcus[6] (RRKM) formalism for the estimation of unimolecular dissociation rates. The difference between the two approaches is that RRKM calculations explicitly consider intramolecular ligand vibrational modes, while RRK calculations only consider intermolecular modes. The discrepancy between the two approaches can become significant when the ligands have intramolecular vibrational modes similar in frequency to the intermolecular vibrational frequencies. The RRKM-EE approach was first used in the Lisy group to re-calculate energies and temperatures of $Na^+(CH_3OH)_{1-8}$[7], and has subsequently been used for water containing systems[8,9].

As a practical matter, the RRKM-EE calculations performed in the Lisy lab have been carried out using two computer programs, rrkmcalc and tqevapen, coded in C by previous graduate students[10]. RRKM calculations are performed using the rrkmcalc program. The details of these calculations have been given previously[7-11]. The important point for this discussion is that the program takes cluster binding energies and vibrational frequencies as inputs and calculates unimolecular dissociation rates, temperatures, and fragment cluster energies as a function of parent cluster internal energy as outputs. These rrkmcalc outputs along with experimental time of flight data are used as input values for the tqevapen program which calculates cluster ion energy and temperature distributions as a function of flight time through the apparatus. These calculations are based on two major assumptions of the evaporative ensemble formalism developed by Klots[3]. The first assumption is that all of the clusters that make it to the quadrupoles are the result of at least one evaporative event. This is reasonable for our experimental setup where neutral clusters are impacted with energetic ions. In fact, molecular dynamics simulations of the collision process have predicted that several evaporative events take place within 100 ps of collision[12]. The second assumption is that the evaporation events occur one ligand at a time. That is, $M^+(L)_n$ can be formed only from the evaporation of one ligand, L, from $M^+(L)_{n+1}$, and can only evaporate one ligand to form $M^+(L)_{n-1}$. This assumption is also supported by molecular dynamics calculations which show only monomer evaporative events[12].

In this chapter, two expansions to the evaporative ensemble part of these calculations will be presented. Instead of altering or enhancing the current tqevapen program, new codes were written for use with MATLAB[13] software which offers more

flexibility and is more user friendly. One of the major limitations to the original tqevapen program was that it would only calculate energy distributions one cluster size at a time, making the comparison of several clusters a tedious process. Therefore, a new code was written to allow for efficient calculation of simulated mass spectra. A second major deficiency of the tqevapen program was that it only calculated fragmentation into a single loss channel. Thus, a separate MATLAB program was written to simulate the fragmentation of a parent cluster into multiple loss channels following photon absorption. These new programs only replace the tqevapen program, but still rely on the use of the rrkmcalc program, which has not been changed.

8.2 Modeling Mass Spectra

Mass spectra are obtained in the Lisy lab by scanning the resolving mass of the first quadrupole while the second and third quadrupoles act as ion guides (r.f. only mode). Thus, prior to arriving at the first quadrupole, a parent cluster, $M^+(L)_n$, can be generated by evaporation of one ligand, L, from $M^+(L)_{n+1}$ and can itself lose one ligand to form $M^+(L)_{n-1}$. The energy distribution of $M^+(L)_n$ prior to the first quadruple can be modeled as a function of time using the following linear, first order differential equations:

$$\frac{dP_{n+1}(E_{n+1})}{dt} = -k_{n+1}(E_{n+1})P_{n+1}(E_{n+1})$$

$$\frac{dP_n(E_n)}{dt} = k_{n+1}(E_{n+1})P_{n+1}(E_{n+1}) - k_n(E_n)P_n(E_n)$$

where P_n, E_n, and k_n are the population, energy and unimolecular dissociation rate of cluster $M^+(L)_n$, respectively. E_{n+1} is the energy of cluster $M^+(L)_{n+1}$ that would result in $M^+(L)_n$ with energy E_n following evaporation of one ligand. From the assumptions of the evaporative ensemble, the boundary conditions for these equations are:

$$P_{n+1}\left(E_{n+1}, t=0\right)=1$$
$$P_n\left(E_n, t=0\right)=0$$

Once the clusters reach the first quadrupole, determined by experimental time of flight data, the feeding mechanism is cut off and only unimolecular dissociation can occur until the detector is reached:

$$\frac{dP_n\left(E_n\right)}{dt}=-k_n\left(E_n\right)P_n\left(E_n\right)$$

With the exception of the time of flight data, all of the parameters needed to solve these equations in order to calculate the population distribution of $M^+(L)_n$ at the detector are obtained from the rrkmcalc program. The MATLAB program Model_MS was created in order to efficiently calculate the energy distributions at the detector for many clusters. The MATLAB code is presented in Appendix A.1. By integrating the energy distributions at the detector for the various clusters, simulated mass spectra are obtained. As a final step, a Gaussian line shape is applied to the simulated mass spectra to approximate the shape of experimental spectra. An example of these types of calculations for $Li^+(H_2O)_n$ clusters is displayed in Figure 8.1 where the parameters for the applied Gaussian line shape were determined by fitting an experimental $Li^+(H_2O)_n$ mass spectrum.

Relative populations of cluster ions observed in mass spectra are a function of the cluster generation process and source conditions. For example, conditions favoring small clusters over large clusters (or vice versa) can be obtained by adjusting variables such as the backing pressure[14]. Therefore, attempting to exactly model any given mass spectrum may not be especially informative. However, investigating how various input parameters

for the calculations impact the relative population of a cluster and its nearest neighbors is informative. The Model_MS program is well suited for such sensitivity calculations.

As an example, the influence of binding energies on the appearance of the simulated mass spectrum was determined for $Li^+(H_2O)_n$. In the simulated spectrum shown in Figure 8.1, the binding energy of each $Li^+(H_2O)_n$ with n>6 was set at 44 kJ/mol (enthalpy of vaporization of water at 298K). To investigate the influence of this value we performed the simple test of changing the binding energy of one cluster (n=20) by ± 10%, keeping all other inputs unchanged. The results of these calculations are summarized in Figure 8.2 and emphasize two important consequences of the assumptions of the evaporative ensemble. First, modest ± 10% changes in binding energies lead to drastic (± 50%) variations in relative intensities in the simulated mass spectra. Second, since all clusters are formed from a larger cluster via evaporation, changing the binding energy of cluster *n* alters the relative population of cluster *n* and the relative population of cluster *n-1*. Raising the binding energy of cluster *n* results in a population increase for cluster *n* and a population decrease for cluster *n-1*. This result has implications in the study mass spectra containing magic numbers. Briefly, magic number clusters are ones which appear with anonymously large intensity in otherwise smoothly varying mass spectra and are often assumed to be the result of especially stable cluster geometries[15-17]. As seen in Figure 8.1, $Li^+(H_2O)_{20}$ has a larger intensity in the experimental mass spectrum than $Li^+(H_2O)_{21}$ and has been identified as a magic number[17]. Based on Figure 8.2, a magic number at n=20 could actually be formed in two ways. It could be the result of anomalously stable n=20 cluster in which case the peak due to n=19 in the mass spectrum would be expected to be suppressed. Alternatively, it could be the result of an

anomalously unstable n=21 cluster in which case the peak due to n=21 would be suppressed. Based on the experimental spectrum in which the peak from n=19 is not suppressed, the latter explanation appears more likely.

8.3 Cluster Energy Distributions Following Photon Absorption

As reported in chapters 5 and 7 of this dissertation, multiple ligand loss can follow photon absorption in some cases. Therefore, it is important to be able to simultaneously model the energy distributions of a parent and several fragment cluster ions as they proceed from the experimental region, the second quadrupole, to the detector. The MATLAB program Laser_Frag5 (code reported in Appendix A.2) was created for this purpose. This program requires as an input the energy distribution of the parent cluster $M^+(L)_n$ in the second quadrupole. The easiest way to generate this input is to use the Model_MS MATLAB program. The other input required for Laser_Frag5 is the total energy imparted to the parent from photon absorption. Given these inputs, Laser_Frag5 calculates the energy distributions following photon absorption of the parent cluster and four fragment clusters at the detector in the following two step process. Before entering the third quadrupole, the energy distributions evolve in the following way:

$$\frac{dP_n(E_n)}{dt} = -k_n(E_n)P_n(E_n)$$

$$\frac{dP_{n-1}(E_{n-1})}{dt} = k_n(E_n)P_n(E_n) - k_{n-1}(E_{n-1})P_{n-1}(E_{n-1})$$

...

$$\frac{dP_{n-4}(E_{n-4})}{dt} = k_{n-3}(E_{n-3})P_{n-3}(E_{n-3}) - k_{n-4}(E_{n-4})P_{n-4}(E_{n-4})$$

where $P_n(E_n)$ is the population of the parent cluster with energy E_n, $P_{n-1}(E_{n-1})$ is the population of the first fragment, E_{n-1} is the energy remaining in the fragment ion

produced from the parent with energy E_n. Once the clusters enter the third quadruple, the feeding mechanism for the fragment ions ceases and only unimolecular dissociation occurs. This is modeled as a simple exponential decay:

$$\frac{dP_n(E_n)}{dt} = -k_n(E_n)P_n(E_n)$$
$$\frac{dP_{n-1}(E_{n-1})}{dt} = -k_{n-1}(E_{n-1})P_{n-1}(E_{n-1})$$
...
$$\frac{dP_{n-4}(E_{n-4})}{dt} = -k_{n-4}(E_{n-4})P_{n-4}(E_{n-4})$$

where t=0 represents the entrance to the third quadrupole and the final time represents the flight time through Q3.

The use of the Laser_Frag5 program has been very helpful in estimating branching ratios into various fragmentation channels as was shown in chapter 7 (see Figure 7.4 and Table 7.1). This program has also provided a more rigorous explanation of the observed loss channels in $Li^+(CH_4)_1Ar_n$ clusters[18]. Experimentally, the observed fragmentation channel for $Li^+(CH_4)_1Ar_n$ following photon absorption is a function of *n* as demonstrated in the third column of Table 8.1. The Laser_Frag5 program was used to calculate the expected fragmentation channel, i.e. the fragment cluster with significant population at the detector, for these clusters. The results are given in the final column of Table 8.1 and match exactly with the experimental observations.

8.4 Conclusions

The cluster generation mechanism described in chapter 2 is ideally suited for description using the assumptions of the evaporative ensemble. Computer programs previously developed and used by the Lisy group suffered from two significant shortcomings. First, energy distributions could only be calculated one at a time, making

calculation of a simulated mass spectrum tedious and time consuming. Second, energy distributions of fragment ions following laser absorption were not calculated. These shortcomings were resolved by the development of two new MATLAB programs, Model_MS and Laser_Frag5.

Model_MS can be used to quickly generate simulated mass spectra and is ideal for sensitivity studies of input parameters such as ligand binding energies. Laser_Frag5 allows the energy distribution following photon absorption of a parent and several fragment ions to be calculated. This analysis is helpful in describing the photon energies required to observe various fragmentation channels. As an added benefit, these new programs are written in MATLAB code and are very user friendly and highly customizable.

8.5 Figures

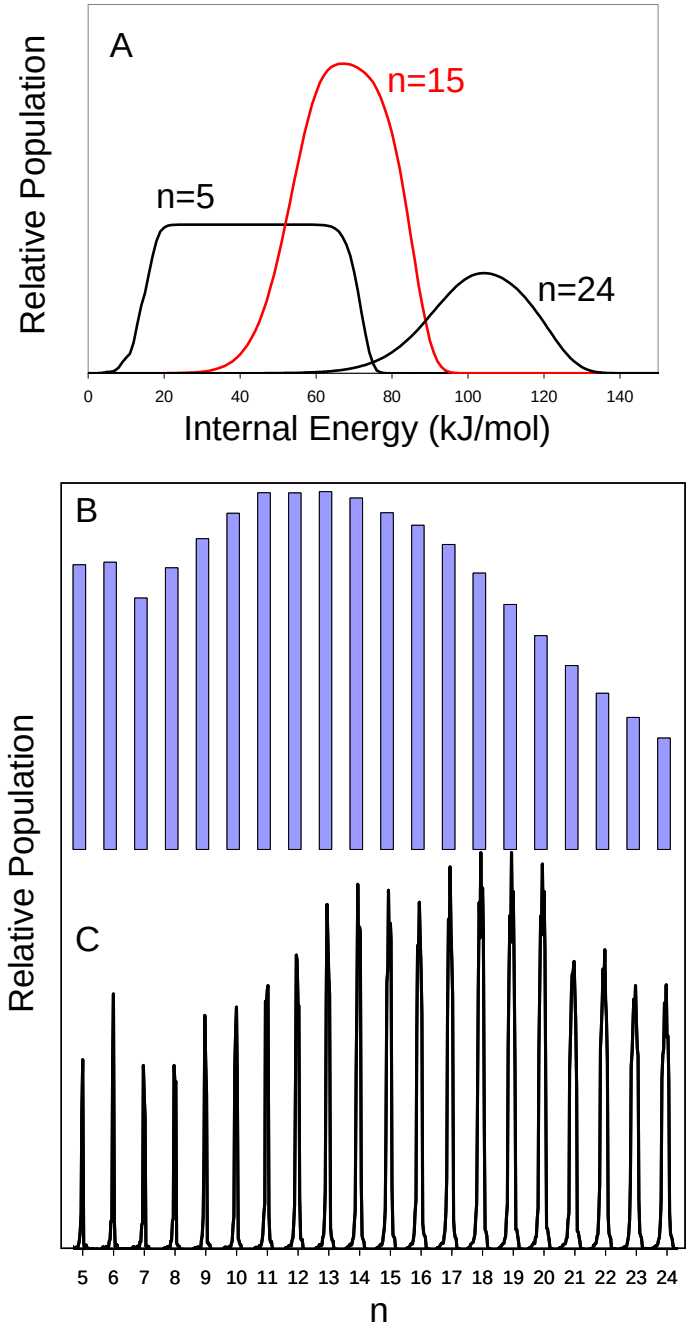

Figure 8.1. A) Representative energy distributions for three $Li^+(H_2O)_n$ clusters calculated using the Model_MS program. B) Simulated mass spectrum of $Li^+(H_2O)_n$ generated with the Model_MS program. C) Experimental mass spectrum of $Li^+(H_2O)_n$.

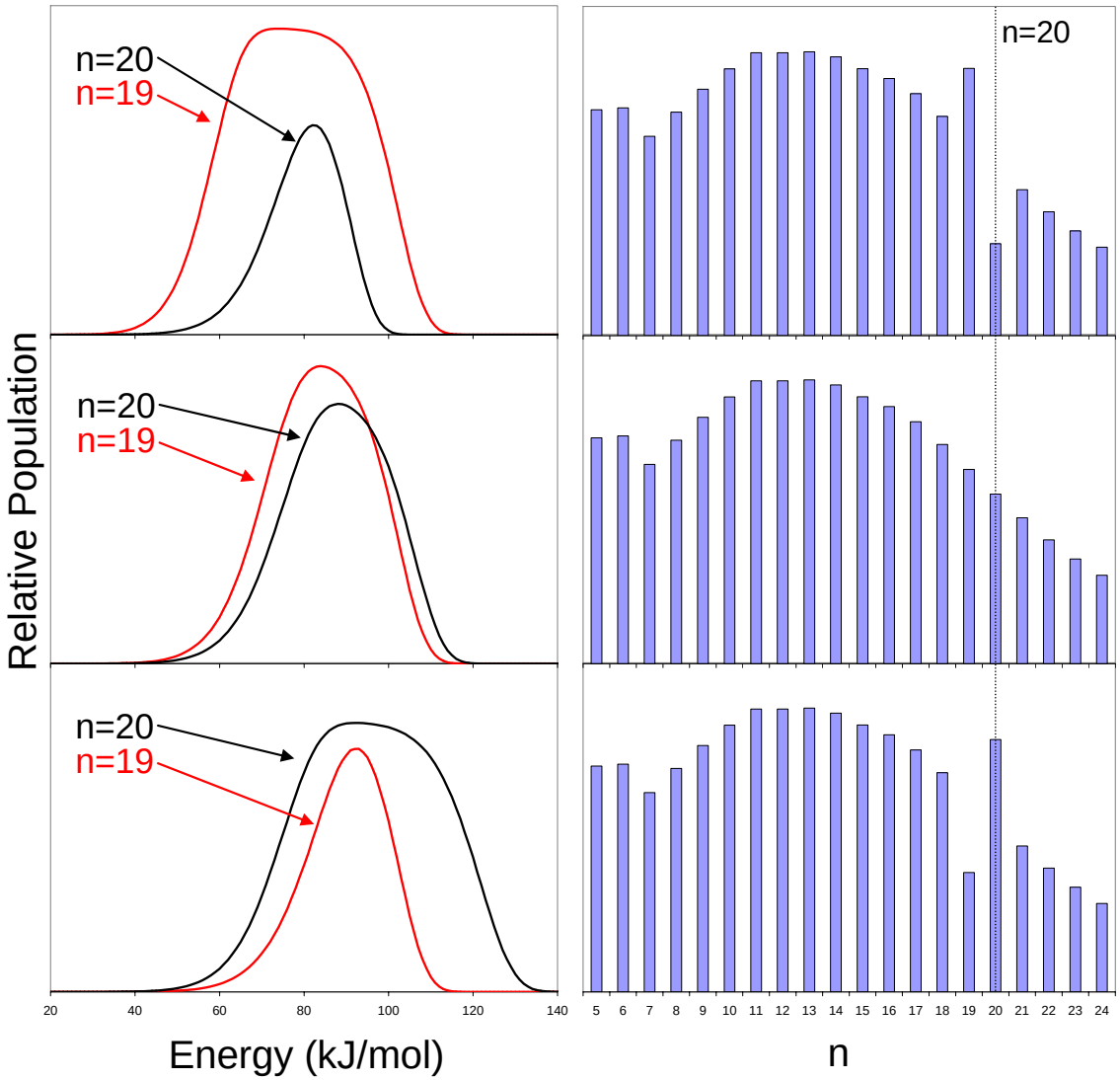

Figure 8.2. Energy distributions for $Li^+(H_2O)_{19\text{-}20}$ (left) and simulated mass spectra for $Li^+(H_2O)_n$ (right). The three panels represent variations in the binding energy of $Li^+(H_2O)_{20}$ used for the calculations. The binding energies are: $BE_{n=20}$ = 48 kJ/mol (bottom), $BE_{n=20}$ = 44 kJ/mol (center), $BE_{n=20}$ = 40 kJ/mol (top). The binding energies for all other clusters with n>6 were 44 kJ/mol.

8.6 Tables

Table 8.1. Experimental and calculated loss channels for $Li^+(CH_4)_1Ar_n$ following the absorption of one photon at 2900 cm^{-1}.

		Loss channel	
n	BE[a] (kJ/mol)	Experimental[b]	Calculated[c]
1	21.58	1 Ar	1 Ar
2	19.28	1 Ar	1 Ar
3	18.48	1 Ar	1 Ar
4	11.68	2 Ar	2 Ar
5	13.7	2 Ar	2 Ar
6	2.6	3 Ar	3 Ar

[a]Binding energy estimated from *ab inito* calculations
[b]Observed loss channel[18]
[c]Calculated loss channel obtained using the Laser_Frag5 program

8.7 References

(1) Kassel, L. S. *The Journal of Physical Chemistry* **1928**, *32*, 225.
(2) Rice, O. K.; Ramsperger, H. C. *Journal of the American Chemical Society* **1927**, *49*, 1617.
(3) Klots, C. E. *Zeitschrift fur Physik D Atoms, Molecules and Clusters* **1987**, *5*, 83.
(4) Draves, J. A.; Luthey-Schulted, Z.; Liu, W.-L.; Lisy, J. M. *The Journal of Chemical Physics* **1990**, *93*, 4589.
(5) Selegue, T. J.; Moe, N.; Draves, J. A.; Lisy, J. M. *The Journal of Chemical Physics* **1992**, *96*, 7268.
(6) Marcus, R. A. *The Journal of Chemical Physics* **1952**, *20*, 359.
(7) Cabarcos, O. M.; Weinheimer, C. J.; Lisy, J. M. *J. Phys. Chem. A* **1999**, *103*, 8777.
(8) Miller, D. J.; Lisy, J. M. *Journal of the American Chemical Society* **2008**, *130*, 15393.
(9) Vaden, T. D.; Weinheimer, C. J.; Lisy, J. M. *Journal of Chemical Physics* **2004**, *121*, 3102.
(10) Weinheimer, C. J. The Role of Hydrogen Bonding in Alkali Metal Ion Solvation, University of Illinois at Urbana-Champaign, 1998.
(11) Weinheimer, C. J. The Role of Hydrogen Bonding in Alkali Metal Ion Solvation, University of Illinois at Urbana-Champaign, 1996.
(12) Cabarcos, O. M. An Experimental and Computational Study of Noncovalent Interactions in Gas Phase Ion Solvation, University of Illinois at Urbana-Champaign, 1998.
(13) MATLAB; R2010a ed.; The MathWorks, 2010.
(14) Wu, C.-C.; Lin, C.-K.; Chang, H.-C.; Jiang, J.-C.; Kuo, J.-L.; Klein, M. L. *Journal of Chemical Physics* **2005**, *122*.
(15) Shin, J. W.; Hammer, N. I.; Diken, E. G.; Johnson, M. A.; Walters, R. S.; Jaeger, T. D.; Duncan, M. A.; Christie, R. A.; Jordan, K. D. *Science* **2004**, *304*, 1137.
(16) Sobott, F.; Wattenberg, A.; Barth, H.; Brutschy, B. *International Journal of Mass Spectrometry* **1999**, *185*, 271.

(17) Steel, E. A.; Merz, K. M.; Selinger, A.; Castleman, A. W. *The Journal of Physical Chemistry* **1995**, *99*, 7829.
(18) Rodriguez Jr, O.; Lisy, J. M. *Journal of Physical Chemistry A*, *115*, 1228.

Chapter 9: Conclusions

In this dissertation, results of infrared presissociation (IRPD) spectroscopy and accompanying calculations were reported for various cluster ion systems. Throughout this work, two major themes arose. High energy conformer trapping was observed in the clusters tagged with argon (chapters 3-6) and multiple photon absorption was observed in non-argonated, hydrated alkali metal ion systems (chapter 7).

High energy conformers were observed for $Cl^-(CH_3OH)_{2\text{-}3}Ar$ as evidenced by a significant red shift of the ionic hydrogen bonded O-H stretching feature. These high energy conformers consist of methanol chains, terminated by an ionic hydrogen bond to the chloride ion and are significant for several reasons. The presence of second and third shell methanols led to a cooperative enhancement of the ionic hydrogen bond. In the case of $Cl^-(CH_3OH)_3Ar$, a methanol O-H stretch was observed at 2733 cm^{-1}, shifted nearly 950 cm^{-1} from its neutral value. A shift of this magnitude indicates a significant weakening of the methanol O-H bond. The presence of the high energy isomers was significant also in that they provided information on the cluster generation process. High energy isomers are more likely to be trapped if their structures resemble the structures of their neutral precursors in some way. Since neutral methanol trimer is a cyclic hydrogen bonded structure, the high energy isomer with two hydrogen bonds could be trapped because of a barrier in going from the neutral structure, with three hydrogen bonds, to the global minimum energy structure with no hydrogen bonds. Finally, the presence of high energy conformers was also significant in that harmonic frequency calculations were inadequate in describing their vibrational frequencies. This led to an alternate and computationally

inexpensive procedure to approximate the enhanced ionic hydrogen bond of a high energy $Cl^-(CH_3OH)_2$ conformer.

The study of chloride containing clusters was extended to Cl^-(*N*-methylacetamide)$_1(H_2O)_{0-2}Ar_2$, where the two major results were based on the ionic hydrogen bonded N-H stretching features in IRPD spectra. The presence of an ionic hydrogen bonded N-H stretching feature in the spectrum of $Cl^-(NMA)_1Ar_2$ confirmed a N-H•••Cl^- interaction. This result conflicted with a previously published computational study which indicated that the chloride should bind to a methyl group. Upon addition of water molecules, the ionic hydrogen bond N-H stretching frequency shifts to lower frequency. This result indicates that the waters strengthen the N-H•••Cl^- interaction by forming hydrogen bonds with the NMA oxygen. MP2 calculations of $Cl^-(NMA)_1(H_2O)_1$ support this interpretation.

The theme of high energy conformer trapping was picked up again in the investigations of $Li^+(C_6H_6)_{2-4}(H_2O)_2Ar_1$. High energy conformers of these cluster ions were identified based on the presence of an experimental feature consistent with an O-H•••O hydrogen bond. This feature, consistent with MP2 calculations, only appeared in spectra obtained by monitoring the (Ar + C_6H_6) fragmentation channel, whereas only features from the global minimum energy structure appeared when monitoring the Ar fragmentation channel. This fortunate result, based on binding energies and relative conformer energies, allowed for specific conformers to be probed based on the fragmentation channel monitored.

The final example of high energy conformer trapping was observed in the M^+(benzyl alcohol)$_1(H_2O)_{0-2}$Ar clusters. However, in these clusters, the high energy

isomers were observed in the same fragmentation channel as the global minimum energy isomers. Despite this, the experimental spectra, when coupled with MP2 calculations, provided much information on the dominant types of non-covalent interactions present in the system. Specifically, O-H•••O hydrogen bonds were present in the high energy isomers while O-H•••π interactions were observed in the global minimum energy structures of all of the hydrated clusters except Na^+(benzyl alcohol)$_1$(H_2O)$_1$Ar. A final observation from chapters 5 – 6 is that Li^+ was proven to be superior to Na^+ at inducing high energy conformer trapping. Presumably this is due to the larger charge density of Li^+ producing deeper wells on the potential energy surface.

The second major theme of this dissertation was multiple photon absorption in hydrated alkali metal ion clusters. Fragmentation into multiple water loss channels was observed for $M^+(H_2O)_{5-7}$ upon irradiation with a single pulse from an IR laser. Support for the presence of multiple photon absorption by these clusters was given by laser fluence dependence studies and by evaporative ensemble calculations (which were described in chapter 8). The two-water loss spectra of each cluster showed only one prominent feature in the hydrogen bonded OH stretching region, corresponding to a linear hydrogen bond, whereas one-water loss spectra showed features corresponding to linear, cyclic, and bent hydrogen bonding motifs. This was rationalized by invoking a multiple photon absorption mechanism wherein multiple identical oscillators in the same cluster each absorb a photon.

Appendix A: MATLAB Code

A.1 Model_MS

```
function
[kmatparent,prodEmat,Pop_Q1Ent,Pop_MidQ2,Pop_Det]=Model_MS(smallest_par
      ent,largest_parent,startE,interval,endE,TOFfile,ratefile,producte
      nergyfile,y0,xc,w,A)
% This program calculates model Mass Spectra based on fragmentation
% rates and time-of-flights.  A Gaussian shape is applied to the
% spectra. To get Gaussian values, plot integrated area of experimental
% mass peak vs. n, the number of ligands, and fit to a Gaussian.
% y0=offset of Gaussian, xc=center of Gaussian, w=width of Gaussian,
% A=area of Gaussian.

%  Outputs generated by this program:
%  prodEmat is a matrix which contains energies of the parent clusters
%     kmatparent is a matrix which contains rate constants (1/microsec)
%     for the parent clusters at energies given by prodEmat
%  Pop_Q1Ent, Pop_MidQ2, and Pop_Det are matricies which contain the
%     population of the parent clusters at the energies given by
%     prodEmat at the entrance to Q1 and the detector, respectively.
%Population and energy matricies have population/energy of
%smallest_parent in leftmost column continuing to larger clusters in
%the columns to the right.

global k1 k2 %These must be global so they can be passed to the
integrator.

% Reading the input files and initializing certain values.
[ratedata,header]=xlsread(ratefile);
    %Ratefile is an Excel file with rate constants in units of 1/s.
    %Column 1 of Ratefile is energy, column 2 contains rate constants
     % of the cluster with 1 ligand, column 3 contains rate constants of
     % the cluster with 2 ligands, ... column n contains rate constants
     % of the cluster with n-1 ligands.  Empty columns must be kept as
     % placeholders for any cluster sizes that are not considered.
[prodenergy,header3]=xlsread(productenergyfile);
    %productenergyfile is an Excel file with the energy of the parent
    %cluster produced from the feeder with energy E given in column 1.
    %Column n (n>1) has the resulting energy of parent n-2 from feeder
    %n-1.
[TOFdata,header3]=xlsread(TOFfile);
    %TOFfile is an Excel file with the time-of-flights for the clusters
    %separated into four regions.  Columns 2-5 contain TOFs for the
    %regions source to Q1 entrance, Q1 entrance to Q2 entrance, Q2
    %entrance to Q3 entrance, and Q3 entrance to detector,
    %respectively.  Column 1 contains integers representing the cluster
    %size starting with n=1.
EnergyVec=zeros((endE-startE)/interval+1,1);
kmatparent=zeros((endE-startE)/interval+1,(largest_parent-
      smallest_parent)+1);
kmatfeeder=zeros((endE-startE)/interval+1,(largest_parent-
      smallest_parent)+1);
prodEmat=zeros((endE-startE)/interval+1,(largest_parent-
```

```
      smallest_parent)+1);
Pop_Q1Ent=zeros((endE-startE)/interval+1,(largest_parent-
      smallest_parent)+1);
Pop_MidQ2=zeros((endE-startE)/interval+1,(largest_parent-
      smallest_parent)+1);
Pop_Det=zeros((endE-startE)/interval+1,(largest_parent-
      smallest_parent)+1);
inputEinterval=prodenergy(2,1)-prodenergy(1,1);
Estep=1/inputEinterval;

% This loop generates the energy vector.
for j=0:(endE-startE)/interval
    EnergyVec(j+1)=startE+j*interval;
end

% Generate prodEmat
for p =1:largest_parent-smallest_parent+1
 prodEmat(:,p)=prodenergy(EnergyVec(:,1)*Estep+1,smallest_parent+1+p);
end

% Generate kmats
for p =1:largest_parent-smallest_parent+1
 kmatfeeder(:,p)=ratedata(EnergyVec(:,1)*Estep+1,smallest_parent+1+p);
 kmatparent(:,p)=ratedata(round(prodEmat(:,p)*Estep+1),smallest_parent+
      p);
end
kmatfeeder=kmatfeeder/1000000;
kmatparent=kmatparent/1000000;
parentsize=smallest_parent;
time=round(TOFdata(largest_parent,2))+2;
Outputs=zeros(time+1,3,(endE-startE)/interval+1);

% This loops through energies (i) and parent sizes (z) sending the
% appropriate values to the integrator.
for z=1:(largest_parent-smallest_parent)+1
    for i =0:(endE-startE)/interval
        k1=kmatfeeder(i+1,z);
        k2=kmatparent(i+1,z);
            %Here, we let the distribution develop for a time equal a
            %little greater than the TOF required to get from source to
Q1
            %entrance The +2 is added as a buffer.  The actual
            %distributions are calcuated below using the correct, exact
            %TOF.
        [T,Y]=ode15s(@lossofone,[0:1:time],[1,0]);
            %values are sent to the ODE solver.
            %Feeders are given uniform distribution.
        Outputs(:,:,i+1)=[T Y];
    end
Pop_Q1Ent(:,z)=squeeze(Outputs(round(TOFdata(parentsize,2))+1,3,:));
Pop_MidQ2(:,z)=Pop_Q1Ent(:,z).*exp(-kmatparent(:,z)*(sum(TOFdata
      (parentsize,3:5))/2));
Pop_Det(:,z)=Pop_Q1Ent(:,z).*exp(-kmatparent(:,z)*sum(TOFdata
      (parentsize,3:5)))*(y0+(A/(w*sqrt(pi/2)))*exp(-2*((parentsize-
      xc)/w)^2));
parentsize=parentsize+1;
```

```
end

function dy = lossofone(t,y)
% Defines the differential equations for loss of 1 ligand.
% Takes time and initial values of the population as inputs.  Gives
% Gives populations at times t as outputs.

global k1 k2 ;
dy = zeros(2,1);
dy(1)=-k1*y(1);
dy(2)=k1*y(1)-k2*y(2);
```

A.2 Laser_Frag5

```
function
[prodEmat,MidQ2,Q3Entrance,Detector,MidQ2Laser,Q3EntranceLaser,Detector
      Laser]=Laser_Frag5(ratefile,productenergyfile,midQ2file,TOFfile,
      startE,interval,endE,parentsize,laserEwavenumber)
% This program calculates the energy distributions of one parent
% cluster and four fragments at the detector  given the energy
% distribution of the parent in the second quadrupole.

%  Outputs generated by this program:
%  prodEmat is a matrix which contains energies of the clusters
%  MidQ2, Q3Entrance, Detector, MidQ2Laser, Q3EntranceLaser,
%  and Detector Laser are populations for the parent and four
%  fragments at the indicated location with and without the influence
%  of the laser at the energies given by prodEmat.
%Population and energy matricies have population/energy of the parent
%in leftmost column continuing to smaller clusters in the columns to
%the right (i.e. parent -1 ligand is in column 2, etc).


global k1 k2 k3 k4 k5
%% Reading the input files and initializing the energy vector and k
   matrix.
[ratedata,header]=xlsread(ratefile);
    %Ratefile is an Excel file with rate constants in units of 1/s.
    %Column 1 of Ratefile is energy, column 2 contains rate constants
    %of the cluster with 1 ligand, column 3 contains rate constants of
    %the cluster with 2 ligands, ... column n contains rate constants
    %of the cluster with n-1 ligands.  Empty columns must be kept as
    %placeholders for any cluster sizes that are not considered.
EnergyVec=zeros((endE-startE)/interval+1,1);
    %pre-allocating the energy vector
kmat=zeros((endE-startE)/interval+1,5);
    %pre-allocating the rate constant matrix
[TOFdata,header4]=xlsread(TOFfile);
    %TOFfile is an Excel file with the time-of-flights for the
    %clusters separated into four regions.  Columns 2-5 contain TOFs
    %for the regions source to Q1 entrance, Q1 entrance to Q2
    %entrance, Q2 entrance to Q3 entrance, and Q3 entrance to
    %detector, respectively.  Column 1 contains integers representing
    %the cluster size starting with n=1.
[prodenergy,header5]=xlsread(productenergyfile);
```

```
    %productenergyfile is an Excel file with the energy of the
    %fragment cluster produced from the parent
[midQ2,header6]=xlsread(midQ2file);
    %the midQ2 file has the midQ2 populations vs. internal energy
prodEmat=zeros((endE-startE)/interval+1,6);
laserE=laserEwavenumber*1.196266e-2;
inputEinterval=prodenergy(2,1)-prodenergy(1,1);
Estep=1/inputEinterval;

%% This loop generates the energy vector.
for j=0:(endE-startE)/interval
    EnergyVec(j+1)=startE+j*interval;
end

%% Generate kmat and prodEmat
prodEmat(:,1)=EnergyVec;
for p =1:5
 kmat(:,p)=ratedata(round(prodEmat(:,p)*Estep+1),parentsize+2-p);
 prodEmat(:,p+1)=prodenergy(round(prodEmat(:,p)*Estep+1),parentsize+2-
      p);
end
prodEmat=prodEmat(:,1:5); % The for loop above gives an extra, useless
      columnt to prodEmat, so it is removed here.
kmat=kmat/1000000;  % Converting kmat to have units of 1/microseconds
time=round(TOFdata(parentsize,4)/2)+2; % the plus two is added on as a
      buffer
Outputs=zeros(time+1,6,(endE-startE)/interval+1);
OutputsLaser=zeros(time+1,6,(endE-startE)/interval+1);

%% Loop for differential equations for non-laser excited
for i =0:(endE-startE)/interval
    tic;
    k1=kmat(i+1,1);
    k2=kmat(i+1,2);
    k3=kmat(i+1,3);
    k4=kmat(i+1,4);
    k5=kmat(i+1,5);

    parentmidQ2=midQ2(round(Estep*(EnergyVec(i+1))+1),parentsize+1);

    [T,Y]=ode15s(@DE_5,[0:1:time],[parentmidQ2,0,0,0,0]);
    Outputs(:,:,i+1)=[T Y];
    time_for_iteration=toc

end
%This is the end of the main loop of differential equation solving.

%% LASER - Loop for differential equations for LASER excited
midQ2excited = zeros((endE-startE)/interval+1,1);
for j=0:(endE-startE)/interval
    if j+1-round(laserE*Estep)<1
        midQ2excited(j+1)=0;
    else
        midQ2excited(j+1)=midQ2(j+1-round(laserE*Estep),parentsize+1);
    end
```

```
end

for i =0:(endE-startE)/interval
    tic;
    k1=kmat(i+1,1);
    k2=kmat(i+1,2);
    k3=kmat(i+1,3);
    k4=kmat(i+1,4);
    k5=kmat(i+1,5);

    parentmidQ2=midQ2excited(i+1);

    [T,Y]=ode15s(@DE_5,[0:1:time],[parentmidQ2,0,0,0,0]);
    OutputsLaser(:,:,i+1)=[T Y];
    time_for_iteration=toc

end
%This is the end of the main loop of differential equation solving.

%% This loop generates output matrices.

Q3time=round(TOFdata(parentsize,4)/2)+1; % index of time for parent to
get from mid Q2 to Q3 entrance

MidQ2=[squeeze(Outputs(1,2,:)) squeeze(Outputs(1,3,:))
squeeze(Outputs(1,4,:)) squeeze(Outputs(1,5,:))
squeeze(Outputs(1,6,:))];
MidQ2Laser=[squeeze(OutputsLaser(1,2,:)) squeeze(OutputsLaser(1,3,:))
squeeze(OutputsLaser(1,4,:)) squeeze(OutputsLaser(1,5,:))
squeeze(OutputsLaser(1,6,:))];

Q3Entrance=[squeeze(Outputs(Q3time,2,:)) squeeze(Outputs(Q3time,3,:))
      squeeze(Outputs(Q3time,4,:)) squeeze(Outputs(Q3time,5,:))
      squeeze(Outputs(Q3time,6,:))];
Q3EntranceLaser=[squeeze(OutputsLaser(Q3time,2,:))
      squeeze(OutputsLaser(Q3time,3,:))
      squeeze(OutputsLaser(Q3time,4,:))
      squeeze(OutputsLaser(Q3time,5,:))
      squeeze(OutputsLaser(Q3time,6,:))];

Detector=[squeeze(Outputs(Q3time,2,:)).*exp(-kmat(:,1)*(TOFdata
      (parentsize,5))) squeeze(Outputs(Q3time,3,:)).*exp(-kmat(:,2)
      *(TOFdata(parentsize-1,5))) squeeze(Outputs(Q3time,4,:)).*exp(-
      kmat(:,3)*(TOFdata(parentsize-2,5)))
      squeeze(Outputs(Q3time,5,:)).*exp(-kmat(:,4)*(TOFdata(parentsize-
      3,5))) squeeze(Outputs(Q3time,6,:)).*exp(-
      kmat(:,5)*(TOFdata(parentsize-4,5)))];
DetectorLaser=[squeeze(OutputsLaser(Q3time,2,:)).*exp(-kmat(:,1)*
      (TOFdata(parentsize,5))) squeeze(OutputsLaser(Q3time,3,:)).*exp(-
      kmat(:,2)*(TOFdata(parentsize-1,5)))
      squeeze(OutputsLaser(Q3time,4,:)).*exp(-
      kmat(:,3)*(TOFdata(parentsize-2,5)))
      squeeze(OutputsLaser(Q3time,5,:)).*exp(-
      kmat(:,4)*(TOFdata(parentsize-3,5)))
```

```
      squeeze(OutputsLaser(Q3time,6,:)).*exp(-
      kmat(:,5)*(TOFdata(parentsize-4,5)))];

function dy = DE_5(t,y)
% Defines the differential equations for loss of 5 ligands.
% Takes time and initial values of the population as inputs.  Gives
% populations at times t as outputs.

global k1 k2 k3 k4 k5;
dy = zeros(5,1);
dy(1)=-k1*y(1);
dy(2)=k1*y(1)-k2*y(2);
dy(3)=k2*y(2)-k3*y(3);
dy(4)=k3*y(3)-k4*y(4);
dy(5)=k4*y(4)-k5*y(5);
```